SPECTROSCOPIC STUDY OF DEFECTS IN CADMIUM SELENIDE QUANTUM DOTS (QDS) AND CADMIUM SELENIDE NANORODS (NRS)

by

SANTANU ROY

M.Sc., Indian Institute of Technology Madras, 2006

AN ABSTRACT OF A DISSERTATION

Submitted in partial fulfillment of the requirements for the degree

DOCTOR OF PHILOSOPHY

Department of Chemistry
College of Arts and Sciences

KANSAS STATE UNIVERSITY
Manhattan, Kansas

2013

Abstract

Ever depleting sources of fossil fuel has triggered more research in the field of alternate sources of energy. Over the past few years, CdSe nanoparticles have emerged as a material with a great potential for optoelectronic applications because of its easy exciton generation and charge separation. Electronic properties of CdSe nanoparticles are highly dependent on their size, shape and electronic environment.

The main focus of this research is to explore the effect of different electronic environments on various spectroscopic properties of CdSe nanoparticles and link this to solar cell performance. To attain that goal, CdSe quantum dots (QDs) and nanorods (NRs) have been synthesized and either doped with metal dopants or embedded in polymer matrices. Electronic properties of these nanocomposites have been studied using several spectroscopic techniques such as absorption, photoluminescence, time-resolved photoluminescence, confocal microscopy and wide field microscopy. Indium and tin are the two metal dopants that have been used in the past to study the effect of doping on conductivity of CdSe QDs. Based on the photoluminescence quenching experiments, photoluminescence of both indium and tin doped samples suggest that they behave as n-type semiconductors. A comparison between theoretical and experimental data suggests that energy levels of indium doped and tin doped QDs are 280 meV and 100 meV lower than that of the lowest level of conduction band respectively.

CdSe nanorods embedded in two different polymer matrices have been investigated using wide field fluorescence microscopy and confocal microscopy. The data reveals significant enhancement in bandedge luminescence of NRs in the vicinity of a conjugated polymer such as P3HT. Photoactive charge transfer from polymers to the surface traps of NRs may account for the observed behavior. Further study shows anti-correlation between bandedge and trap state emission of CdSe NRs. A recombination model has been proposed to explain the results. The origin of traps is also investigated and plausible explanations are drawn from the acquired data.

SPECTROSCOPIC STUDY OF DEFECTS IN CADMIUM SELENIDE QUANTUM DOTS (QDS) AND CADMIUM SELENIDE NANORODS (NRS)

by

SANTANU ROY

M.Sc., Indian Institute of Technology Madras, 2006

A DISSERTATION

submitted in partial fulfillment of the requirements for the degree

DOCTOR OF PHILOSOPHY

Department of Chemistry
College of Arts and Sciences

KANSAS STATE UNIVERSITY
Manhattan, Kansas

2013

Approved by:

Major Professor
Dr. Viktor Chikan

Abstract

Ever depleting sources of fossil fuel has triggered more research in the field of alternate sources of energy. Over the past few years, CdSe nanoparticles have emerged as a material with a great potential for optoelectronic applications because of its easy exciton generation and charge separation. Electronic properties of CdSe nanoparticles are highly dependent on their size, shape and electronic environment.

The main focus of this research is to explore the effect of different electronic environments on various spectroscopic properties of CdSe nanoparticles and link this to solar cell performance. To attain that goal, CdSe quantum dots (QDs) and nanorods (NRs) have been synthesized and either doped with metal dopants or embedded in polymer matrices. Electronic properties of these nanocomposites have been studied using several spectroscopic techniques such as absorption, photoluminescence, time-resolved photoluminescence, confocal microscopy and wide field microscopy. Indium and tin are the two metal dopants that have been used in the past to study the effect of doping on conductivity of CdSe QDs. Based on the photoluminescence quenching experiments, photoluminescence of both indium and tin doped samples suggest that they behave as n-type semiconductors. A comparison between theoretical and experimental data suggests that energy levels of indium doped and tin doped QDs are 280 meV and 100 meV lower than that of the lowest level of conduction band respectively.

CdSe nanorods embedded in two different polymer matrices have been investigated using wide field fluorescence microscopy and confocal microscopy. The data reveals significant enhancement in bandedge luminescence of NRs in the vicinity of a conjugated polymer such as P3HT. Photoactive charge transfer from polymers to the surface traps of NRs may account for the observed behavior. Further study shows anti-correlation between bandedge and trap state emission of CdSe NRs. A recombination model has been proposed to explain the results. The origin of traps is also investigated and plausible explanations are drawn from the acquired data.

Table of Contents

List of Figures

List of Tables

Acronyms

NPs = Nanoparticles

QDs = Quantum dots

NRs = Nanorods

PV = Photovoltaics

CV = Cyclic voltammetry

CCD = Charged coupled device

APD = Avalanche photodiode

PMMA = poly methyl methacrylate

P3HT = poly (3-hexylthiophene)

Acknowledgements

It is my great pleasure to acknowledge the following individuals whose contributions went beyond the mere scientific aspects of this work.

I would like to express my gratitude to my major advisor Prof. Viktor Chikan for his guidance, immense support and continuous encouragement. He trained me to develop new ideas and carry out independent research. In short, he is a great mentor and helped me in every aspect of my PhD life.

My sincere thanks to my collaborators Prof. Daniel A. Higgins of Kansas State University and Prof. Christopher Elles of University of Kansas. Prof. Higgins allowed me to access the spectroscopic instruments in his lab and whenever I needed, he was there to help me with scientific advices and knowledge. I acknowledge the active participation by Prof. Elles during THz set-up and all insightful discussions about research.

I take this opportunity to thank the administrative and technical staff in the Department of Chemistry for their spontaneous support and co-operation. The list includes, but not limited to, Mr. Jim Hodgson, Mr. Ron Jackson, Mr. Tobe Eggers, Ms. Mary Dooley, Mr. Ralph Hudson, Ms. Lisa Percival and Ms. Kimberly Ross.

I thank all past and present postdocs and graduate students of our lab who made this journey enjoyable. I thank Dr. Pankaj Mandal, Dr. Christopher Tuinenga, Dr. Pinar Dagtepe, Dr. Naween Dahal, Dr. Raj Kumar Dani, Mr. George Podaru and Mr. Hongfu Luo and Ms. Jenna Wasylenko. I extend my thanks to Ms. Fadzai, Ms. Alicia, Mr. Joshua and Mr. Lorinc who came to our lab as summer research interns. I really enjoyed working with them and appreciate their contribution in my research.

My sincere gratitude to the Department of Chemistry, Kansas State University and NSF-EPSCOR for providing enough funding and scholarship to carry out this research.

All my friends deserve special thanks to make Manhattan the sweet home away from home. I thank Dr. Abhinav Alakshendra, Ms. Uma Sarmistha, Ms. Kaayana Sharma, Dr. Shyamal Krishna Talukdar, Dr. Lateefuddin Syed, Dr. Prashant Chopade, Mr. Rohit Gali, Ms. Smita Patil, Dr. Aditya Gundugola, Dr. Mausam Kalita and Dr. Rajarshi Dey who helped me in every possible way.

Next, I would like to thank my wife Dr. Jhinuk Gupta for being a great support throughout these years, especially during those crucial and not-so-easy moments. Finally, I thank my mother Mrs. Sumita Roy. This thesis would not come to the reality without her sacrifice, support and blessings.

Dedication

I dedicate this thesis to my mother.

Chapter 1 - Introduction

1.1 Motivation

Cadmium selenide (CdSe) nanoparticles (NPs) have drawn significant attention in last few decades due to their wide range of applicability in fields like solar cells research, light emitting diodes (LEDs),[1,2] lasers[3] and medicine.[4] CdSe is a semiconducting material and semiconductor industries have shown significant growth in last few decades. Total worldwide revenue of semiconductor industries have increased from 161 (source: Gartner Dataquest Analysis Report) billion US dollars to 311 (source: iSuppli Analysis Report) billion US dollars within a period of 12 years (1999 to 2011). Microchips, diode lasers, LEDs transistors are few examples of semiconducting device and semiconductor materials that are important component for data storage, data transportation and data management. Apart from significant amounts of commercially viable products, semiconductor research has drawn significant attention in scientific community due to its wide range of applicability. Online data base (Web of Knowledge [v.5.9]) shows more than 250,000 research articles on semiconductors alone. It is important to understand the reasons that make semiconductors unique for electronics applications.

Semiconductors are unique in terms of electronic conductance because they behave as both an insulator and a metal depending on applied temperature. The primary reason for the temperature dependence is that the band gap of semiconductor falls in between that of metals and insulators (Figure 1.1).

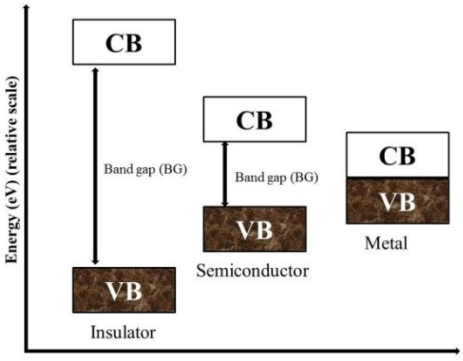

Figure 1.1 Schematic representation of band gap of metal, semiconductor and insulator. The energy is represented in relative scale.[5]

A schematic representation of band gaps of insulator, semiconductor and metal are shown (Figure 1.1). Energy in electron volts (eV) is represented in Y axis of the figure and it is not in absolute scale. The lower and upper level of band gap is known to be valence and conduction band respectively. It is observed that insulator and metal have maximum and minimum band gap respectively. Insulators are known not to be good conductor of electricity as electrons stay in the valence bands and cannot reach to conduction band owing to wide band gap. In contrast, metals have narrow band gap and electrons are not only confined to valence bands. Significant numbers of electrons, known as free electrons, are in the conduction bands and they help metals to carry electricity. Semiconductors have band gaps that fall in between insulator and metal and depending on applied temperature they can either behave as metals or insulators. At low temperature, electrons in semiconductors stay in the valence band leaving conduction band empty and as a result they behave as insulators. Whereas, at elevated temperature electrons can be promoted to the conduction band of semiconductor and all of a sudden they will conduct electricity which is metallic behavior. Electrical conductivity (σ) of semiconductors increases with increase in temperature (T) and this dependence is expressed in eq (1).[6]

$$\sigma = \alpha e^{-E/2kT} \qquad (1)$$

Where, α, E and k are proportionality constant, band gap of semiconductor and Boltzmann constant (in eV). A plot of "ln(σ)" *vs.* temperature shows linear increase in conductivity with increase in temperature with a negative slope (E/2k).

Temperature does not alter the intrinsic electrical conductivity of semiconductors. The intrinsic property of semiconductor can be changed by introducing trace amount of foreign atom to the semiconductor and it is called doping. A correct choice of dopants makes semiconductor either electron rich (n-type semiconductor) or electron deficient (p-type semiconductors). Semiconductors are doped to improve intrinsic conductivity which suits them better for electronic applications.

Any electronic device is built upon diodes, transistors and logic gates which cannot be prepared without doped semiconductors. N- and p- type semiconductors for example are first combined to make diodes which can either help or restrict electron flow depending on the connection. A simple schematic diagram of forward and reverse bias of diode is shown in Figure 1.2. A diode is a p-n junction and depending upon how it is connected to the electrical wire the bias is called forward or reverse. When p- and n- type end are connected to the positive and

negative end of the cell, it is called forward bias. Electron moves freely in the circuit for forward bias as negative end is connected to the electron rich part of diode.

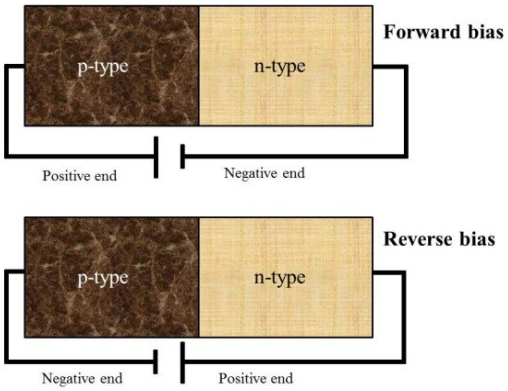

Figure 1.2 Forward (top) and reverse (down) bias of diodes.[5]

As a result electrons move freely from one end to the other and current moves in the opposite direction establishing a good electrical connection. Similarly when p- and n- type end are connected to the negative and positive end of the cell, it is called reverse. Electron movement is restricted in this geometry due to the different attachment of electrical wires and reverse bias does not allow electricity to pass. This unique behavior of diode contributes greatly in electronic industries to build logic gates.

Semiconductor industries mostly use ultra-pure silicon for fabricating electronic devices as silicon is available in high abundance. The only drawback of using silicon is that it is very expensive to manufacture ultra-pure silicon. Significant effort has been made to replace silicon with other semiconducting materials but no appropriate alternative could be found till now. CdSe nanoparticles are semiconductor materials like its bulk counterpart and are good model system and they can be synthesized easily by colloidal synthesis. Band gap of CdSe falls in the visible range of the electromagnetic spectrum which makes it excellent candidate for solar cell applications. Band gap of CdSe can be tuned by tuning size of CdSe nanoparticles as band gap increases with decreasing particle size. These qualities make CdSe NPs potential material for electro optic devices in spite of its low abundance and cost. Significant work has been done on CdSe nanoparticles and online database show more than 15,000 research papers (Web of Knowledge [v.5.9]) on CdSe. CdSe nanoparticle research is still producing significant number of scientific papers which signifies it is still an important material in scientific community. One of

major limitations of any CdSe based device is that they lack in efficiency. This lack in efficiency can be attributed to many facts but in this thesis one of the common drawbacks of CdSe NPs named trap states will be discussed and they are defects in the crystal structure. These trap states decrease electro optic efficiency of CdSe based devices. Hence, there is a scope to investigate more about trap states of CdSe NPs and make it a commercially viable material for more efficient electro optic devices such as solar cells. Two different shape NPs are discussed here and they are quantum dots (QDs) and nanorods (NRs).

1.2 CdSe Quantum Dots

CdSe QDs are spherical semiconductor nanoparticles made of inorganic core of few hundreds of atoms and surrounded by organic surfactant known as ligand from the colloidal synthesis. Radii of QDs are smaller than bulk exciton Bohr radius (≈ 5.6 nm) therefore, they represent a class of material intermediate between molecule and bulk CdSe.[7] Many properties of QDs are different than that of their bulk counterpart, such as, energy levels of bulk and QDs are completely different which will be discussed in next sections. Surface area of QDs increases rapidly with the decrease in QDs size and surface play an important role in their electrical and optical properties. Bulk CdSe is not susceptible for trap states but QDs are due to their small particle size. Let us go through all these differences between CdSe QDs with their bulk counterpart.

Charges generated by absorption of photon by CdSe are not localized in bulk material as they are not confined. Valence and conduction bands structures of bulk CdSe are shown in Figure 1.3.

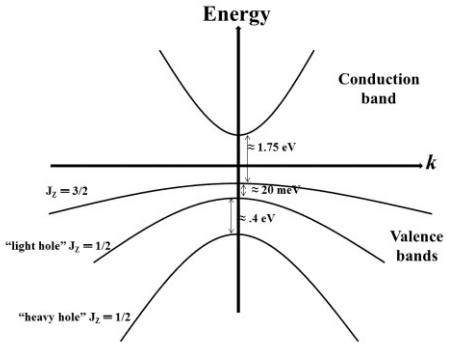

Figure 1.3 Schematic of bulk CdSe (energy gaps are not perfectly scaled).[8]

The band gap of bulk CdSe is close to 1.75 eV as shown in Figure 1.3. It is very difficult to distinguish between heavy hole and light hole as their energy levels are close to each other. It can be seen that the conduction band has sharper in nature than the valence bands. As a result electrons are more localized in semiconductor than that of holes. Electrons and holes are not confined in bulk CdSe but this scenario changes when particle size become small.

1.2.1 Quantum Confinement in CdSe QDs

QDs are small particles and as a result electrons and holes generated upon absorption of photon are confined in small space and many behaviors of QDs can be explained by quantum mechanics. That is why QDs are referred to as quantum confined particles. According to the Heisenberg uncertainty principle of quantum mechanics, position of any quantum confined particle cannot be predicted absolutely at any point of time. As a result charges generated can move within QDs and at the same time they can fell the effect of each other as they are confined in very small space. That is the reason they sometime termed as excitons. Quantum confinement of both electron and hole in all three dimensions leads to discrete energy levels which are represented in Figure 1.4.

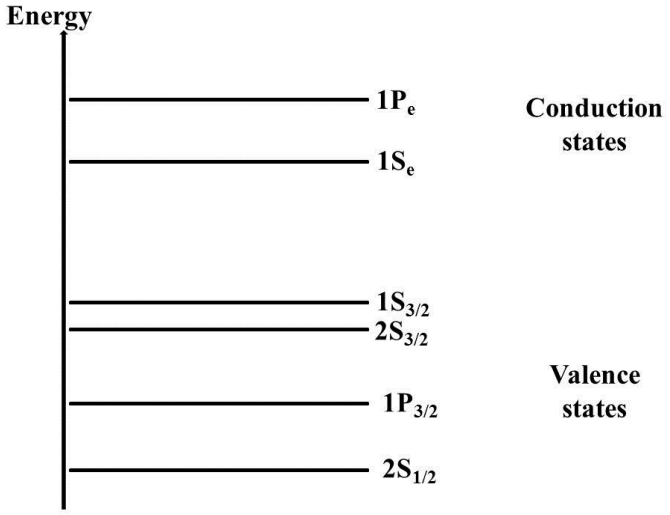

Figure 1.4 Schematic of discrete energy levels of CdSe quantum dots (energy gaps are not perfectly scaled).[9]

The difference between highest level of valence band and lowest level of conduction band is known as band gap. It can be seen in Figure 1.4 that both valence and conduction bands show discrete energy levels and they are not looking like band structures. The gaps between every

discrete energy levels increases with decrease in QDs size. As a result, both optical absorption and emission from QDs show blue shift as its size decreases.[10] Although CdSe QDs show very different and interesting behavior than its bulk counterpart, it shows similar crystallographic structure of its bulk form. There is a challenge associated with QDs and that is surface to volume ratio increases as size of particles decreases. Larger surface may give rise to greater chance of surface defects.[11]

CdSe QDs have large surface to volume ratio due to their very small particle size and it can be visualized as shown in Figure 1.5. Surface to volume ratio is plotted against radius of a perfect sphere and the same figure can be understood for QDs as well. The radius of the QDs is varied from 0.1 nm to 4 nm and surface to volume ratio changes from 6 nm^{-1} to 0.8 nm^{-1}. It can be observed that surface area increases as the size of QDs decreases. A window of size distribution (1 nm to 2.8 nm) is shown in in Figure 1.5 as this thesis does not deal with very small QDs and CdSe does not behave as QDs above exciton Bohr radius. Although this large surface area is covered with ligands, there are few trap states on surface that causes significant decrease in photoluminescence.

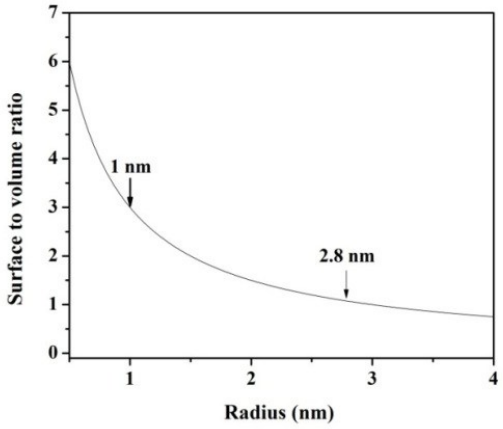

Figure 1.5 Surface to volume ratio *versus* radius plot of a perfect sphere. Radius is represented in nanometers to correlate QDs.

1.2.2 Defects

Surface traps are still very important issue as they decrease performance of electro optic materials and reduce photoluminescence efficiency. The challenge of lowering of photo luminescence can be overcome by adopting core-shell composite structure which is very

important both in the perspective of experimental and practical applications.[12] It is important to discuss about the origin of surface traps. Surface traps are defects on QDs surface that arise at the time of synthesis. CdSe QDs crystalize in wurtzite structure and it is made of perfect tetrahedron (Figure 1.6).

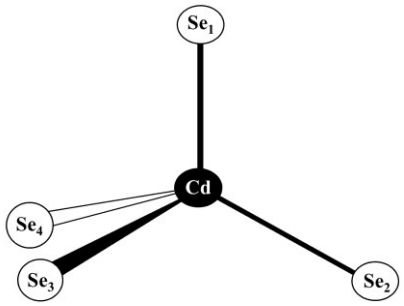

Figure 1.6 A perfect tetrahedral (unit of wurtzite structure).

All selenium atoms in wurtzite structure are surrounded by cadmium in tetrahedral structure and vice versa. Let us consider the filled circle and empty circles are cadmium (Cd) and selenium (Se) atoms respectively. Selenium atoms are surrounded in tetrahedral geometry where all bond lengths are same and all bond angles (selenium-cadmium-selenium bond angle) are 109.4^{o}. The tetrahedral geometry can be visualized as two selenium atoms (Se_1 and Se_2) are in the same plane of the paper. The third (Se_3) and fourth (Se_4) selenium are located above and below the plane respectively. It is important to surround every atom by four counter atoms. There are many atoms in surface which are not surrounded by counter atoms and as a result all valences are not satisfied. Those positions are called traps states. This is a very common form of defect as the synthesis is very rapid and causes imperfections in crystal structure.

An important strategy to suppress the trap states is to use a higher band gap inorganic semiconductor material on core of the QDs. It is observed that particles overcoated with inorganic materials are more stable and robust than that of organic ligands and has greater tolerance to processing and experimental conditions. Some examples of core-shell QDs are CdS on CdSe and CdSe on CdS,[13] ZnS on CdSe,[14] CdTe on CdSe[12]. It is known that CdSe QDs and ZnS crystalize in wurtzite and zinc blend structures respectively. Both wurtzite and zinc blend structure are consist of same crystallographic motif and they are compatible to each other. Core-shell structure made of CdSe and ZnS form Type-I semiconductor.[15] ZnS is a semiconducting

material like CdSe and it does not interfere in optical properties of CdSe as ZnS has very high band gap in the UV range of electromagnetic spectrum.

1.2.3 Synthesis and Characterization of CdSe QDs

Significant amount of work has been done with core-shell QDs and it is drawing attention in scientific community as a model system. Synthesis and structural analysis of CdSe QDs have drawn significant attention at the initial stage of CdSe QDs evolution.[16-18] Solution phase QDs synthesis can be understood as solid phase formation from a solution phase.[19] It starts with a rapid nucleation followed by relatively slow growth of nanoparticle on the existing nuclei. Nearly monodisperse QDs are synthesized by the approach developed by Bawendi *et al.* 1993.[16] This synthesis is carried out by injecting metal-organic precursors into a vigorously stirred container containing a hot coordinating solvent. Medium to long chain of alkylphosphine R_3P, alkylphosphine oxide R_3PO (R = butyl or octyl), alkylamines, alkylacids etc. are used as solvents and coordinating ligands for nanoparticle growth. Organometallic compound like dimethyl cadmium ($Cd(CH_3)_2$) is used for the synthesis of CdSe QDs. A major drawback of using organometallic compound is that it is very volatile and toxic which has adverse effect on human health. Scientist have made significant effort to find an alternative of organometallic compound as precursors.

The challenge of using organometallic compound is overcome by Peng *et al.* where they have employed an alternative route to prepare CdSe QDs by choosing less toxic and more stable cadmium precursors such as cadmium oxide (CdO) and cadmium acetate ($Cd(OAc)_2$).[20,21]

An alternate approach which employs single precursor is also described in the literature to prepare nearly monodisperse QDs. The single source precursor used is $Li_4[Cd_{10}Se_4(SPh)_{16}]$ and it is synthesized in lab according to the literature method.[22] In this single precursor method core-shell CdSe/ZnS particles are synthesized using two steps. In the first step, a single precursor $Li_4[Cd_{10}Se_4(SPh)_{16}]$ is used to grow CdSe quantum dots in the presence of hexadecyl amine (HDA) which act as ligand. Few other long length hydrocarbons are also know for QDs synthesis and they are dodecylamine (DDA), octadecylamine (ODA) etc. The long length of hydrocarbon in HDA makes it a very good surfactant that stabilizes the QDs. The solution containing HDA and single precursor is stirred for 18 hours at 120 °C and then temperature is raised to 250 °C

and kept at this temperature for 2 hours. A solution made of distilled TOP, diethyl zinc and hexamethyldisilithiane is added drop-wise to grow a ZnS shell around the nanoparticles.

Synthesized QDs need a thorough purification to remove excess ligands which act as a stabilizer at the time of synthesis. An organic polar solvent like methanol or ethanol is used to dissolve the excess ligands and QDs precipitate out from the solution in presence of this organic polar solvent. Centrifugation followed by discarding supernatant removes excess ligands. The sample is vacuum dried and dissolved in non-polar organic solvent like toluene. These purified QDs are then subjected to several spectroscopic experiments and characterization. Transmission electron microscopy (TEM) is used to determine formation of nanoparticles by recording TEM image. High resolution TEM of a single QD is shown in Figure 1.7.[23] It is seen in the TEM image that size of QD is about 3 nm and it form a uniform crystal structure. This TEM image (Viktor Chikan's group) shows that synthesis produces high quality QDs.

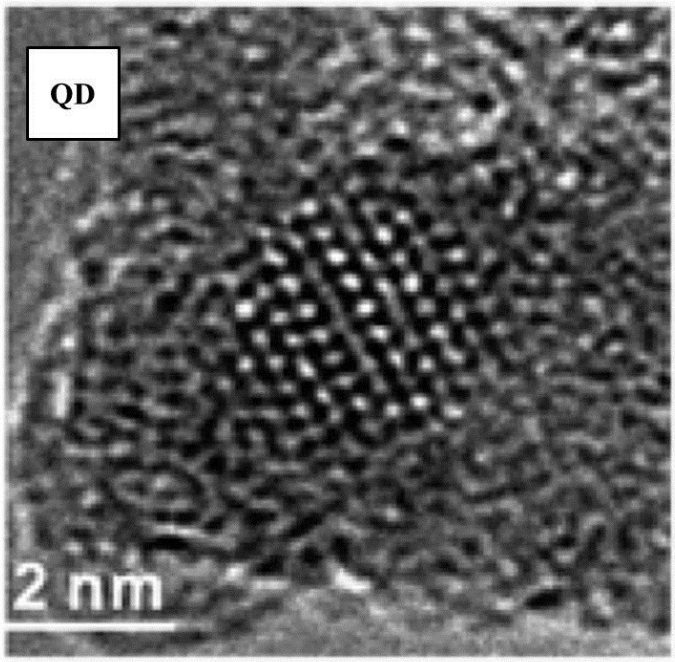

Figure 1.7 High resolution TEM of a single CdSe QD showing wurtzite crystal structure.

1.2.4 Optical Properties of CdSe QDs

The absorption spectra of CdSe QDs resemble the absorption spectra of both bulk CdSe and molecular spectra. Bulk semiconductors show an excitonic peak which is weak in nature and

an increasing absorption profile along the direction of low wavelengths. The smooth increase in absorption feature at low wavelength is due to higher energy exciton formation in the band structure. Molecular transitions on the other hand show sharper features in the absorption profile as the energy levels are discrete. It is important to record absorption spectra of purified CdSe QDs as it provides information about quality of the synthesized QDs. CdSe QDs show absorption profile close to the bulk absorption with a very sharp excitonic peak and an absorption spectrum of CdSe is shown in Figure 1.8. The sharp excitonic peak of QDs arises due to the formation of excitons located in the discrete energy levels close to band edge and it can be seen at wavelength 535 nm in Figure 1.8. It is very distinct absorption feature that can be identified from its bulk counterpart and it can also give information about the size of the QDs. As size of QDs decreases, the sharp absorption features show hypsochromic shift.

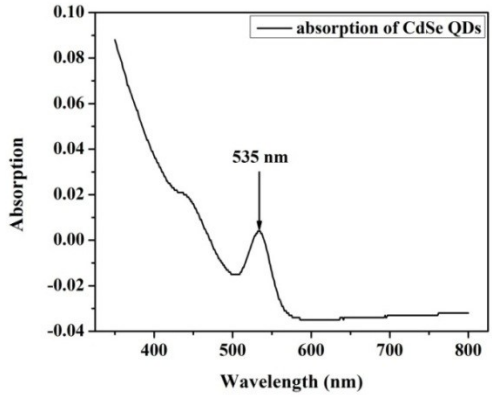

Figure 1.8 Absorption spectra of Cdse QDs in toluene showing sharp excitonic peak.

Absorption of photon creates excitons in QDs as briefly discussed in the previous paragraph. The possible photo physical processes typically involve a variety of pathways as shown in the Jablonski diagram in Figure 1.9A. A schematic of molecular photophysical recombination is shown (Figure 1.9A) and this diagram is known as Jablonski diagram. Ground state and excited state are shown as G and H respectively and different vibrational states within them are also shown (Figure 1.9A). Molecule absorbs photons and gets excited to the excited state. These excited molecules can give rise fluorescence either by radiative recombination or they can decay through non-radiative recombination.

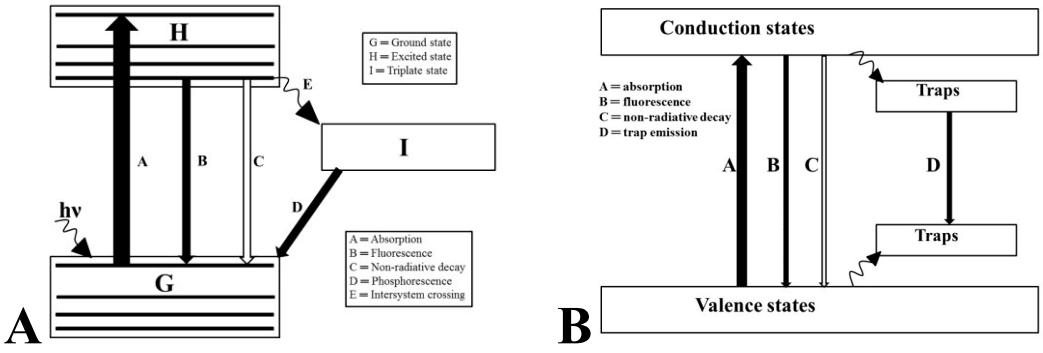

Figure 1.9 A) Different pathways of recombination of molecular excitons.[24] B) Schematic representation of CdSe QDs recombinations (right).

Non-radiative decay does not produce photon instead they produce heat and this heat is dissipated in the system. Another way of recombination is that the excited molecules tunnel to a triplet state through intersystem crossing and returns to ground state to give rise to phosphorescence.

QDs show similar photophysical processes as that of the molecule. A schematic representation of photophysical recombination of QDs is shown in Figure 1.9B. In QDs electrons get excited from valence band to conduction band upon absorption of photons leaving a hole in the conduction band. This electron hole pair is known as excitons and they can either recombine to give rise fluorescence or they can go through non-radiative decay. There is another path to recombine these excitons and that is through trap state recombination. The electrons and holes can tunnel to trap states and recombination of them at this stage would give rise to trap state emission (Figure 1.9B emission D). As a result this trap state emission shows bathochromic shift with respect to the band edge emission. Core-shell structure of QDs suppresses these trap state and excitons tunneling gets restricted which results in enhancement in photoluminescence. Apart from the similarities in photophysical processes, QDs show different photochemical behavior and that is known as photo-degradation. Photo-oxidation is the most common part of photo-degradation where reaction between high energy carriers and oxygen result in oxidation of particle surface. Photo-oxidation is a major problem in QDs research and it can be avoided by keeping QDs in glove box which will increase QDs life.[25]

Stokes shift is an important parameter associated with any fluorophore. A higher energy light source than that of band gap of QDs is always used to excite them. As a result excitons need to undergo relaxation process before it can recombine and emit fluorescence. Difference between

the absorption and emission maxima is known as stokes shift and it is represented here (Figure 1.10).

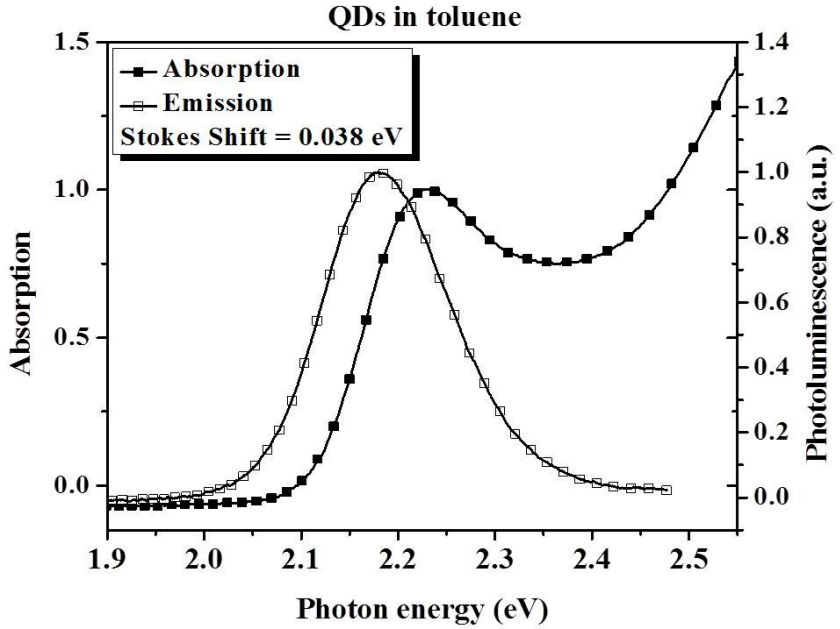

Figure 1.10 Absorption and emission spectra of CdSe NRs in toluene showing Stokes shift.

Absorption and emission of QDs are shown by filled squares and empty squares respectively and they are plotted against photon energy. The maximum absorption is found to be 0.9 and emission is represented in arbitrary unit. Stokes shift for this undoped CdSe QDs is calculated to be 0.038 eV. Stokes shift arises due to relaxation of excited electron and it varies with size of QDs.[26]

CdSe QDs show many interesting behavior and fluorescence intermittency which is also known as blinking is one of the very important properties shown by them.[27] Blinking is a single particle emission from colloidal nanoparticles which is interrupted by dark state under continuous illumination of light. A single particle regime can be achieved in blinking experiment by using a microscope with powerful objective lens. It is a very powerful technique because it can probe single QD and can provide fundamental behavior of a single QD. Information obtained from blinking experiment can also provide useful information about particle and their interaction with surroundings. It is a behavior which is well observed but not very well understood. There are few models to understand blinking behavior but two most important models are “diffusion control charge transfer model” and “auger assisted ionization model”.[28] The diffusion control charge transfer model states that a QD goes from bright state to dark state when those two states

are in resonance with each other which results in energy transfer. This model was most accepted model in scientific community in past but currently scientists believes "auger assisted ionization model" is most acceptable model to explain blinking behavior. Auger assisted ionization model states that a QD does not blink if it is charged and it blinks when the charge is neutralized.

Blinking behavior can be studied by confocal and wide field microscopy and instrumental detail of them is given in later chapter. While the confocal microscopy allows observing a single QD with high speed of data acquisition, wide field microscopy allows simultaneous blinking behavior of multiple QDs at the same time with slower speed. Significantly narrow spot size can be generated by those microscopes and hence behavior at single particle level can be achieved. The emitter, which is in this case QDs, is subjected to continuous illumination of light and periodic emission is recorded. The emitter is defined to be in 'on' and 'off' state when it is emitting and not emitting light respectively. The plot of 'on' and 'off' state distribution is known as time trace and these time traces are completely random and probability of occurrence of 'on' and 'off' state is represented by power law distribution.

Blinking time transient is completely random and non-reproducible phenomenon which means different emitter of same sample shows different 'on' and 'off' time distribution. It is also observed that same emitter does not show identical distribution if it is subjected for reproducing the distribution. Although the distribution is non-reproducible, it always follows the power law. Blinking of nanoparticles will be discussed in a great detail in this thesis.

1.3 CdSe Nanorods

CdSe nanorods (NRs) are semiconducting quantum confined material with rod like structure. QDs and NRs are considered to be zero and one dimensional quantum confined materials respectively. A significant advantage of NRs over QDs is that they transport excitons very efficiently due to the presence of the long axis. Due to the anisotropic shape of NRs, excitons can be confined along the axis as well as diameter and they behave a little differently than QDs.

1.3.1 Surface to Volume Ratio of CdSe NRs

Surface to volume ratio of NRs can be calculated like QDs and it is shown in Figure 1.11. A perfect cylinder is considered and radius is varied from 0.5 nanometers to 3 nanometers keeping length of the cylinder at 20 nanometers as shown in Figure 1.11 (left). Similarly length of NRs is

varied from 3 nanometers to 20 nanometers keeping radius of NRs at 2 nanometers as shown in Figure 1.11 (right). It is clear from the two graphs that change in radius has significant impact in surface to volume ratio of NRs. This nature is also reflected in the band gap of NRs and it is observed that the band gap has significant impact on radius change of CdSe NRs than that of change in length.

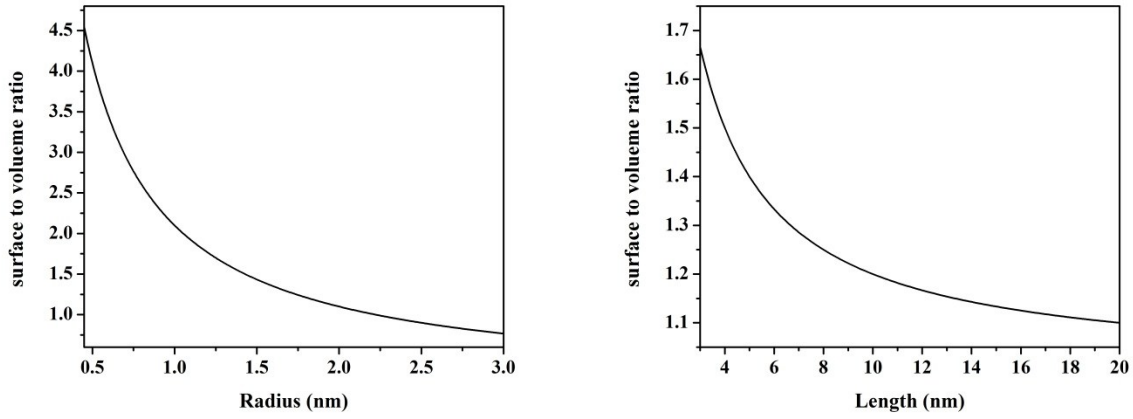

Figure 1.11 Surface to volume ratio of nanorods with change in radius (left) and length (right) respectively.

It is important to make a comparison here to surface to volume ratio of QDs and NRs. A perfect sphere and cylinder of same volume is considered where radius of the sphere and cylinder are considered to be 3.4343 nm and 4 nm respectively and length of the cylinder is 6 nm. Surface to volume ratio of the sphere and cylinder is calculated to be 0.8735 nm and 0.8333 nm respectively. It can be concluded from this calculation that surface to volume ratio of QDs would be more than that of NRs when same volume is considered.

1.3.2 Shape Dependent Property of NRs (Dipole moment)

CdSe nanorods show length and shape dependent optical properties which make it a better candidate for electro optic devices.[29] In contrast to CdSe QDs, CdSe NRs exhibit a high value of dipole moments which are determined experimentally.[30] Dipole moment of a series of CdSe nanorods is determined and their values are represented in Table 1.1 and this Table is presented elsewhere.[30] It is observed in the table that NRs have significant in-built dipole

moment and origin of this high dipole moment is explained with theoretical calculation by Nann *et. al*.[31]

Width (nm)	Length (nm)	Dipole moment (Debye)
3.1 ± 0.1	58 ± 6	153.4 ± 23.9
4.8 ± 0.2	26 ± 4	209.9 ± 32.6
3.8 ± 0.2	20 ± 3	126.4 ± 36.9
3.0 ± 0.1	51 ± 6	126.3 ± 21.4
3.0 ± 0.1	33 ± 4	95.7 ± 24.4

Table 1.1 Experimentally determined dipole moments of different NRs.

Origin of high dipole moment of NRs lies in their crystal structure. It is known that building block of wurtzite structure is perfect tetrahedron where bond lengths of equatorial and axial atoms are equal as shown in left panel of Figure 1.12. Axial and equatorial bond are represented by "a" and "e" respectively. Right panel (Figure 1.12) shows a distorted tetrahedron and it can be seen that axial bond is slightly shorter that the equatorial bonds.

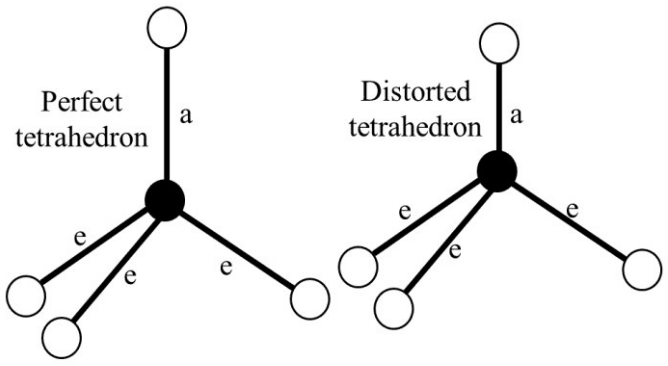

Figure 1.12 Schematic representation of a perfect and a distorted tetrahedron. Origin of dipole moment in NRs is due to the shortening of axial bond in distorted tetrahedron.

As a result of this distortion, molecule possesses net dipole moment. This net dipole moment of a single building block is not significant, whereas, a large network of this tiny dipole moment can add up to a significant value.[31] As a result CdSe NRs show very high dipole moment and this

high dipole moment can be very useful to align nanorods by application of electric field. Alignment of NRs by application of electric field is beyond the scope of this research. Another advantage of this high dipole moment is that the charge separation and transport in NRs is significantly easy.

1.3.3 Synthesis and characterization of NRs

Synthesis and characterizations of CdSe nanoparticles of different shapes and sizes are the focus of research interest in scientific community for last decade.[32] It is important to realize the reason behind the formation of different shape of nanoparticles and it is believed that monomer concentration and surfactant play major role for the shape of CdSe nanoparticles.[33] At high monomer concentration, nanocrystals grow exclusively along the c-axis of the wurtzite structure which results in rod like structure of CdSe. Organic ligands that are used at the time of synthesis also play very important role in nanorods growth.[34] The ligands stabilize NRs (100 plane) and they can only grow along the c-axis of the wurtzite structure. One commonly used ligand is trioctylphosphine oxide (TOPO) which is represented in Figure 1.13.

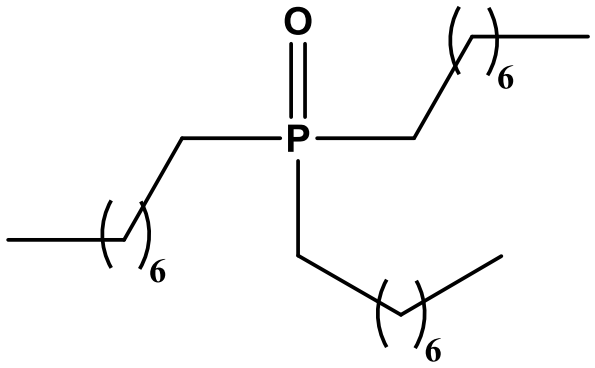

Figure 1.13 Molecular structure of trioctylphosphine oxide (TOPO) which is important ligand in NRs synthesis.

CdSe nanorods were first synthesized by Wang et al. by solvothermal method.[35] CdSe NRs can be synthesized by two different approach and they are discussed one by one. NRs are synthesized using dimethylcadmium ($Cd(CH_3)_2$) as one of the precursors and this approach is employed in the early synthesis of NRs. Dimethylcadmium and selenium (Se) are co-dissolved in a tri-alkyl phosphine (-butyl or -octyl) and the solution is injected into hot (340-360 ^oC) trioctyphosphine oxide (TOPO) .[33,36,37] Nucleation occurs rapidly followed by growth (280-300

°C). There is a major disadvantage working with this synthetic protocol and that is the use of dimethylcadmium which is very toxic in nature and volatile so it can get into human body and have some adverse effect. It is important to come up with some alternative synthetic route to avoid working with any toxic material. Another disadvantage in this reaction procedure is that it requires very high temperature which increases the energy demand.

An alternate path is available and also followed in this thesis and that method is described here. Dimethylcadmium is replaced with cadmium oxide (CdO) which is not toxic in nature and NRs were synthesized under oxygen-free conditions. The reaction mixture, comprised of CdO, trioctylphosphine oxide (TOPO) and TDPA (Tetra decyl phosphonic acid), are prepared in a three-neck flask with septa, a thermometer and a refluxing column. The refluxing column is attached to a Schlenk line. The solution is first heated to 120 °C under Argon flow and subsequently placed under vacuum for 1 hr. A selenium-trioctylphosphine (SeTOP) solution is prepared separately in a nitrogen-filled glovebox. A mixture of trioctylphosphine (TOP) and selenium (Se) powder are placed into a vial that was then capped with a septum. The solution is stirred in the glovebox with a magnetic stirrer until Se is dissolved completely. The temperature of the solution containing CdO is raised to 260 °C and solution became golden yellow once entire CdO is dissolved. At this point, the cadmium solution is returned to atmospheric pressure and SeTOP solution is injected at once. As a result solution temperature decreased to 230 °C and temperature rises back to 260 °C as temperature controller is set to that temperature. The entire growth process was monitored by UV-visible and photoluminescence spectroscopy and NRs growth is terminated after ~ 5 min. These synthesis described above produce bare NRs but core-shell NRs are also known in the literature.[38] This process of core shell formation improves the photoluminescence of the particle but it also hinders the electronic communication between either with adjacent nanorods or with nanorods and its environment. In this research nanorods are not coated with any shell material and that is why mostly nanorods are loosely bound with the surface ligands.

A successful synthesis produces NRs with excess surfactant and NRs need thorough purification. An organic polar solvent like methanol or ethanol is used to dissolve the excess ligands and NRs precipitate out from the solution in presence of this organic polar solvent. NRs are separated from the supernatant liquid by centrifugation and discarding the supernatant. A non-polar organic solvent like toluene is used to bring NRs in solution phase. These purified NRs

are then subjected to several spectroscopic experiments. High resolution TEM of synthesized NRs are shown (Figure 1.14) and it can be seen that NRs have excellent size distribution and they show single crystalline nature.

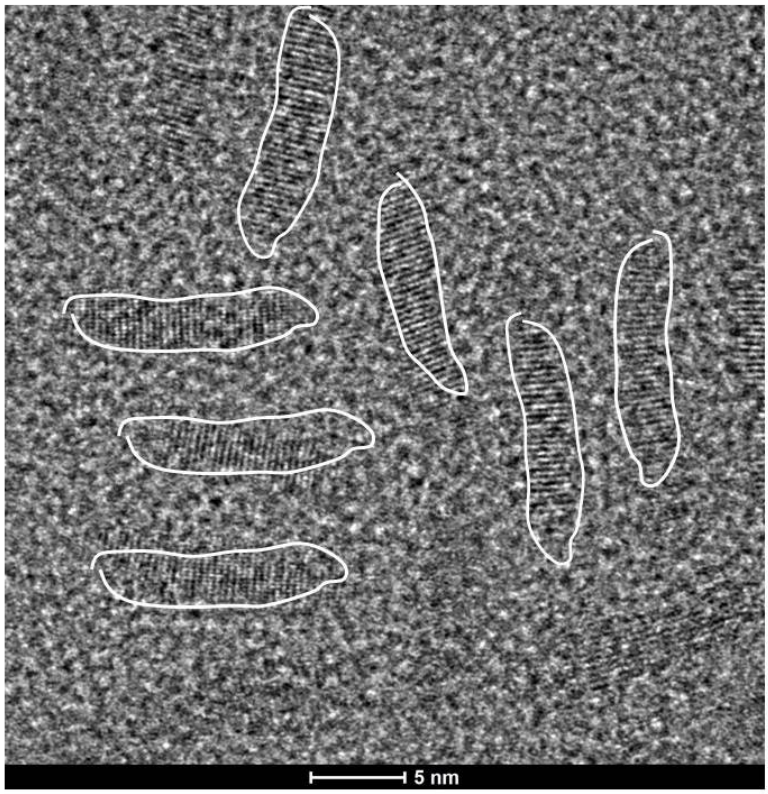

Figure 1.14 High resolution TEM image of CdSe NRs (unpublished data from Chikan group).

1.3.4 Optical properties of NRs

The absorption spectra of CdSe NRs resemble the absorption spectra of both bulk CdSe and molecular spectra like QDs. CdSe NRs show absorption profile close to the bulk absorption with a very sharp excitonic peak. The sharp excitonic peak of NRs arises due to the formation of excitons located in the discrete energy levels close to band edge. It is very distinct absorption feature that can be identified from its bulk counterpart. Absorption spectra of CdSe NRs is shown (Figure1.15) and it shows a strong excitonic peak at 576 nm. Bathochromic shift in absorption is observed with increase in diameter of NRs which in consistent with quantum confinement. NRs do not show significant quantum confinement effect with its change in length. Absorption of photon creates excitions in QDs as discussed in the previous section.

Photoluminescence arises due to recombination of band edge excitons and this recombination can follow different paths like molecular photochemistry as discussed in Figure 1.9. NRs absorb photons and electron is promoted to the conduction state creating a hole in the valence state.

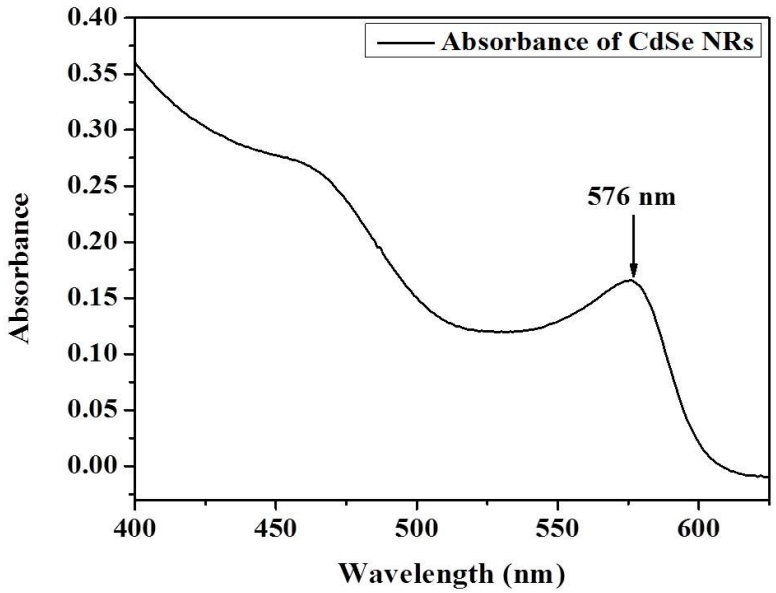

Figure 1.15 Absorption spectra of CdSe NRs in toluene.

These electron and hole in NRs give rise fluorescence either by radiative recombination or they can decay through non-radiative recombination of excitons as shown in Figure 1.16.

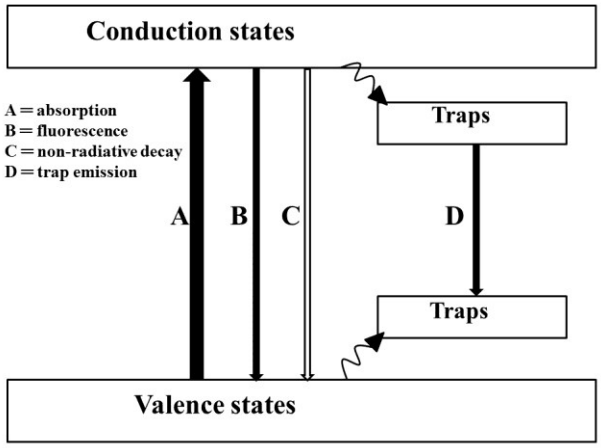

Figure 1.16 Schematic of recombination pathways of CdSe NRs.

Non-radiative decay does not produce photon. Instead heat is produced and this heat is dissipated in the system. This schematic of recombination pathway is a simple model to understand emission in CdSe NRs but more detailed model will be discussed in the later chapters. Another way of recombination of excitons in NRs is defined as trap state emission. Trap state emissions can arise from various pathways. Recombination between conduction band electron and trapped hole, trapped electron and valence band hole, trapped electron and trapped hole can appear as trap state emission. Electron and hole both can tunnel to trap states close to conduction state and valence state respectively. Trap state emission also arises when excitons in traps recombine and it gives rise to higher wavelength emission (Figure 1.16). Trap states are mostly recognized as non-emissive state and it decreases luminescence and to improve luminescence ZnS shell is used. Similar to the CdSe QDs, ZnS is used to suppress defects or trap states. Trap state emissions from CdSe nanorods are investigated in detail in this thesis. Photo-oxidation is also a major problem in NRs research as it is a problem for QDs research too and it can be avoided by keeping NRs in glove box which will increase NRs life.[25]

Stokes shift is an important parameter for NRs and it is shown in Figure 1.17.

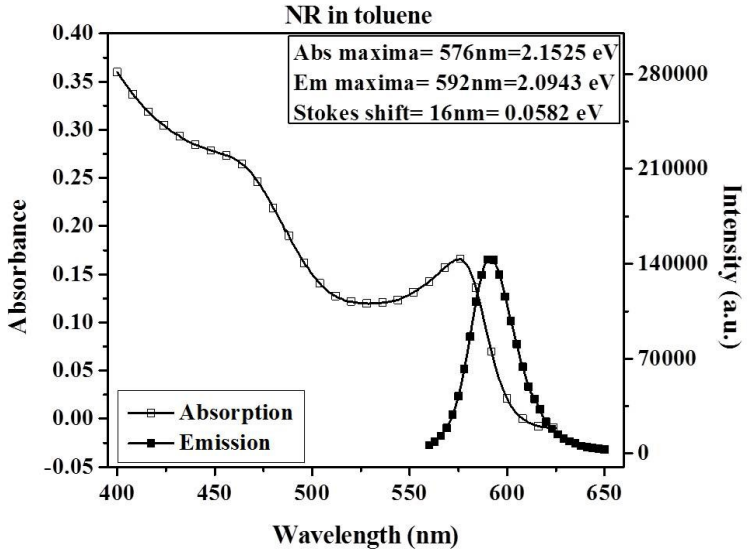

Figure 1.17 Absorption and emission spectra of CdSe NRs in toluene showing Stokes shift.

Absorption and photoluminescence of CdSe NRs in toluene are recorded and plotted against wavelength. Absorption and photoluminescence are shown in empty and filled squares respectively. Absorption of this NRs sample is observed at 0.17 and emission is expressed in

arbitrary unit. Absorption and emission maxima are observed at 572 nm and 591 nm respectively. Difference of maxima of absorption and photoluminescence is called stokes shift and it is calculated to be 0.0582 eV for this particular NR sample. The observed positive value of stokes shift is consistent with the theory of photoluminescence. Electrons move to deep conduction band by absorption of photons and they undergo relaxation process before recombination. As a result emission of fluorophore is expected to show bathochromic shift and this is explained before (Figure 1.10). Stokes shift of NRs is dependent on their aspect ratio, ratio of length by diameter of NRs, and it increases with increase in aspect ratio. It is experimentally calculated that stokes shift increases from 45 meV to 80 meV when aspect ratio changes from 4 to 8.[37]

Anisotropic shape of CdSe nanorods has resulted in many interesting properties. An unique property that is exhibited by CdSe NRs is that it shows linearly polarized light emission.[37] It is observed that CdSe nanorods absorb and emit linearly polarized light along its long axis. Wide field and confocal microscopy have emerged as very important tools to look at dynamics of flourophore at single particle level as it provides direct information about the dynamics at single particle level.[28] CdSe NRs also show fluorescence intermittency like CdSe QDs with only one major difference and that difference is that NRs show polarized emission. This behavior gives enormous flexibility to modify and develop different experiments to study properties of NRs. Blinking of CdSe NRs will be discussed in a great detail in this thesis.

1.4 Nanoparticle-polymer Photovoltaics

Photovoltaic (PV) cells are device that convert incident photons to direct current. The amount of fossil fuels is decreasing and they also produce green house gases which is the reason of global warming. It is important to fabricate clean sources of energy. Solar cells have been evolving over the years and they are categorized as different generations of solar cells. The first generation of solar cell converts light to electricity utilizing p-n junctions and it has the disadvantage of high cost of production. It is of great interest to reduce the cost of the solar cell in the second generation solar cells by employing semiconductor thin film technologies. Although, cost of production reduces significantly in second generation of solar cell but their

efficiency is very poor. The focus now is to fabricate third-generation solar cells that include multi-layer cells which could provide good efficiency and low cost of production.

It is important in PV cell design to optimize energy conversion of incident solar flux to electrons in external circuit. The theoretical maximum efficiency is analyzed by the Schockley-Queisser and it is found to be 31%.[39] This theoretical limit is not achieved yet but a significant development is introduced by combining nanoparticles and polymer into a photoactive layer.[40] The main advantage of introduction of the nanoparticles-polymer layer is to improve the power conversion efficiency (PCE) and this interface is known as a heterojunction. Silicon based PV cells are dominating the market right now and they provide PCE of about 15%.

The most important parts of fabricating PV are to generate excitons and deliver respective charges to corresponding electrodes. Any form of PV follows these two general rules and efficiency of any PV will depend mainly on these two factors. A few other important factors will be discussed later in detail but it is important to understand how PV works. A schematic of energy levels of a general polymer PV is shown in Figure 1.18.

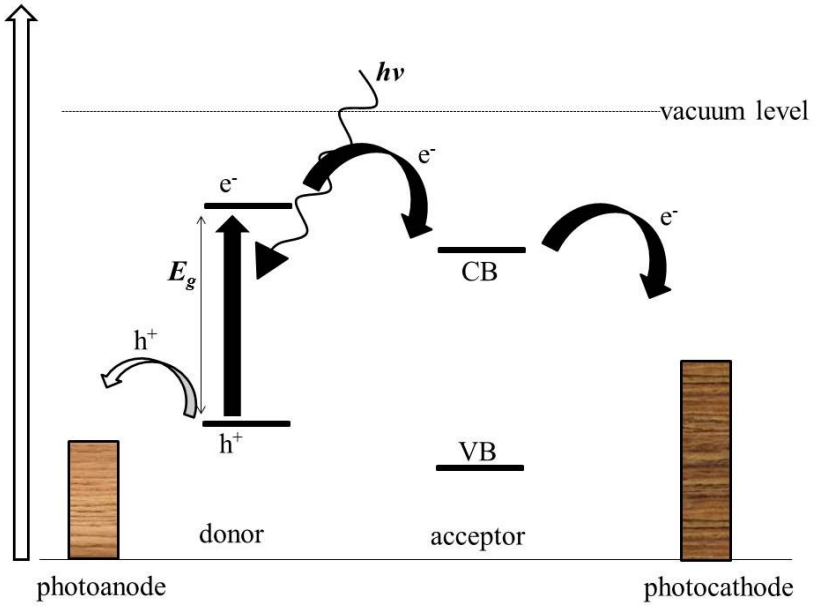

Figure 1.18 Energy levels and light harvesting from photons for an acceptor/donor interface within photoactive layer of PV cells.

Energy levels of donors and acceptors are shown in Figure 1.18. Electrons and holes are represented by e^- and h^+ respectively. Light is being absorbed by polymer which has band gap

represented by E_g. Photoanode and photocathode are electrodes where holes and electrons are deposited respectively. The photoactive layer contains materials that can absorb photons efficiently and create excitons. Photons with energy greater than band gap of donor will be absorbed by the photo active materials and the excitons do not dissociate into corresponding charges. Excitons are loosely bound electron and hole pairs located in the conduction and valence bands respectively. These excitons then either can recombine with each other or they can dissociate into corresponding charges. Recombination of excitons will give rise to either fluorescence or the energy can be dissipated in the system in the form of heat energy. Once the charges are formed they migrate to the corresponding electrodes and create direct current. Presence of donor and acceptor material in the photoactive layer helps migrating corresponding charges. Nanoparticles have low electron affinity in nanoparticle-polymer PV cells and readily accept electrons from the polymer under illumination. The electrons are accepted by the conduction bands as shown in Figure 1.19 and it can be understood that polymers act as an electron donor. This process results in exciton dissociation.[41]

The key and most important parameter of a PV cell performance is PCE (photon conversion efficiency). PCE is defined as the ratio of the maximum power output (P) to the incident light power (φ) which is represented in equation 2 below.

$$PCE = \frac{P}{\varphi} \qquad (2)$$

Another important parameter is external quantum efficiency (EQE). The EQE is defined as the number of photo-generated electrons to the number of photons. The process of charge generation and transportation in PV cells occurs in five steps and each step has efficiency associated with it. Overall efficiency is the product of individual efficiencies of five steps as shown in equation 3.

$$EQE = \rho_A \rho_{diff} \rho_{diss} \rho_{tr} \rho_{cc} \qquad (3)$$

The first term (ρ_A) in equation 2 is the absorption yield of photon and it depends on the absorption coefficient and the thickness of the photoactive layer. The second term is known as exciton diffusion yield (ρ_{diff}) and it governs the ability to diffuse excitons without recombination. The parameter represented in the fourth term is exciton dissociation yield (ρ_{diss}) which can be understood as probability of electrons and holes to separate in heterojunction. The energy required to separate excitons is the difference in energy between the conduction bands of donors and acceptors of polymer-nanoparticle cell as shown in Figure 1.18. The next parameter is the charge carrier transportation yield (ρ_{tr}) and charge transportation involves hopping mechanism as

shown in Figure 1.19. This charge transportation yield can be affected by the non-radiative traps in the nanoparticles. The ultimate goal of our work is to investigate this trap and use this information for betterment of PV cells. The last crucial parameter is the charge collection yield (ρ_{cc}) and this term represents the ability of charge transfer from photoactive layer to the electrodes. EQE values are found to be significantly lower for polymer-nanoparticle PV cells and the reasons are believed to be due to recombination of excitons before exciton dissociation and loss of charge during the transportation from photoactive layer to the electrodes. A few experimentally determined values of PCE and EQE are mentioned in table 1.2 and the table is taken from Saunders *et. al*.[41]

Polymer	Nanoparticle	EQE	PCE
OC_1C_{10}-PPV	CdSe TPs	0.52	2.8
P3HT	CdSe NRs	0.70	2.6
MEH-PPV	CdSe TPs	0.46	1.13
P3HT	CdSe QDs	-	0.85
P3HT	TiO_2 QDs	0.15	0.42
P3HT	PdSe QDs	-	0.14
MEH-PPV	CdSe TPs	-	0.003

Table 1.2 PCE and ECE of different polymer-nanoparticle solar cells.

Three different shapes of nanoparticles are shown here and they are QDs, NRs and tetrapods (TPs). It is observed that NRs-P3HT system shows highest PCE (2.6) from comparison between different polymers and nanoparticles in Table 1.2. This PCE is not very good but it is significantly higher than others and could be a potential system to implement in solar cells.

There are few different polymers used in polymer-nanoparticle PV cells and those polymers are poly(3-hexyl thiophene) (P3HT), pentaerithitol tetraacylate (PTTA), poly[2-methoxy-5-(2'-ethylhexyloxy)-p-phenylene vinylene] (MEH-PPV), polybis(thienyl)thienodia-thiazolethiophene (PDDTT), poly[2,6-(4,4-bis-(2-ethylhexyl)-4H-cyclopenta[2,1-b;3,4-b]-dithiophene)-alt-4,7-(2,1,3-benzothiadiazole)] (PCPDTBT), poly(thiophene vinylene) (PTV), poly(2,5-bis(3-alkylthiophen-2-yl)thieno[3,2-b]thiophene) (PBTTT) etc. The most important parameters to keep in mind at the time of choosing polymers are that they need to be highly

conjugated and they need to be hydrophobic in nature. P3HT is the most commonly used polymer among the polymers mentioned above in polymer-nanoparticle PV cells.

The nanoparticle geometry has significant influence on PCE. PCE increases with increase in aspect ratio of nanoparticle and that is why NRs have potential to make better solar cells than QDs. A higher aspect ratio is not necessarily correlated with higher PCE as it is found that photoactive layer consist of single wall carbon nanotubes (SWCNT) with high aspect ratio show low PCE.[42] Focus of this research is to understand CdSe nanoparticles to make them better solar cell materials. CdSe nanoparticles based solar cells lack in efficiency, hence, intrigue us to concentrate in fundamental behavior of these NPs. It is one of the interests to fabricate solar cells using CdSe nanocrystals and the advantages are discussed in earlier sections. The first CdSe sensitized solar cell is constructed in 1998 by Fang *et.al.*[43] and it did not have good efficiency and later CdSe QDs[44] and NRs[45] are used to construct solar cells as well because it is a very good model system. Highest power conversion efficiency from a CdSe nanocrystal sensitized solar cell is found to be 6.9%.[45] This conversion efficiency is not good with compared to commercially available silicon based solar cells and that is why it is important to study their fundamental behaviors to improve the efficiency of polymer-nanoparticles solar cells.

1.5 Thesis Outline

CdSe NPs is a very good model system to understand fundamental behaviors. This thesis is an effort to understand traps and defects in CdSe QDs and NRs. Several different spectroscopic techniques are utilized to understand these traps and defects in these materials. Details of different instrumental techniques are discussed in Chapter 2.

Introduction of defects intentionally in semiconductor is an important process as they significantly impact the electronic efficiency of materials. This intentional introduction of defects or foreign atoms is known as doping. There are significant applications of doped semiconductors in electronic devices. CdSe QDs are expected to show interesting behavior upon doping with foreign atoms as shown by other commercially viable semiconductor materials. Extensive research has been done on QDs but doping of QDs is explored relatively in less detail in the literature. In general dopants are chosen in a way that they do not have a significant lattice mismatch with parent semiconductors and either it makes them electron rich or electron

deficient. Hence, the effect of dopants on the properties of QDs is explored by the help of spectroscopic techniques in Chapter 3. The question we want to address with this work is how different dopants change the electronic structure of QDs

Band gap tuneability is an important part of QDs research and band gap can be tuned by changing size of NPs. Therefore, it is important to determined band gap of QDs precisely and their variation with respect to the doping of QDs. Cyclic voltammetry is a method that measures current verses potential with changing potential. Complete CV cycle provides information about valence and conduction band of QDs and one can calculate band gap from it. Cyclic voltammetry of undoped and doped QDs are discussed in Chapter 4.

NPs are significantly small particles and important questions are that how individual NP behaves and how they interact with each other. It is important to probe single NP to get information about it. Single particle confocal microscopy and wide field microscopy are excellent microscopic techniques to study single NP. CdSe QDs and indium doped CdSe QDs are subjected to confocal microscopy study and that is discussed in Chapter 5.

This thesis deals with significant work in the field of CdSe NRs. NRs show many properties different than that of QDs and one of the important properties of NRs is that it emits polarized light. Absorption and emission of polarized light is very important as it provides fundamental information about NRs such as orientation of transition dipole moment. The polarized light emission is studied using single particle confocal microscopy and it is described in Chapter 6.

Another important aspect of CdSe NRs that is dealt with in this thesis is emissive trap states. Trap states are mostly categorized as non-emissive states and they act as a photoluminescence quencher. It is important to know more about trap states as they could have significant impact on reducing efficiency of CdSe NPs based electronic devices. Trap states could be a path to improve efficiency of electro optic devices. Significant results are collected to learn more about the emissive trap states in CdSe NRs. Bilayer hetero junctions (BHJ) concept is adapted to study NRs as it improves communication between NRs and its surroundings. Chapter 7 deals with detail study of fluorescence intermittency of polymer-NR samples. Trap state shows significant results during the course of experiments. An extensive work has been carried out to address all possible aspects of NRs transition mechanism and it has been turned out that four levels transition mechanism exists for CdSe NRs which is discussed in Chapter 8.

Chapter 2 - Instrumental Background

Time resolved fluorescence:

Time resolved fluorescence is an analytical technique to measure the life time of fluorophore and in this research fluorophore are going to be CdSe QDs and NRs. Normal fluorescence does not provide any time dependent information about a fluorophore, but it is important to better understand the chemical environment about the fluorophore. Time resolved fluorescence carries more information about the molecular environment of fluorophore than that of the static fluorescence. There are many molecular events, such as rotational diffusion and resonance energy transfer which occur in the same time scale as that of fluorescence decay. Thus, time resolved fluorescence can be utilized to investigate these processes and information about chemical surroundings of fluorophore can be obtained.

A schematic representation of time resolved fluorescence set up is shown in Figure 2.1.

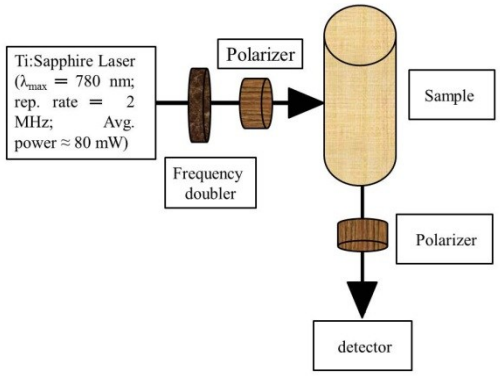

Figure 2.1 Time-resolved fluorescence set up.

The spectrometer uses output of a cavity-dumped Ti:Sapphire laser (λ_{max} = 780 nm, repetition rate = 2 MHz, average power ≈ 80 mW) pumped by a diode laser (532 nm, 4.6 W). Generated femto second pulses are guided to a nonlinear crystal (frequency doubler crystal) and it converts 780 nm light to 390 nm light. This up converted light is then guided to the sample and emitted fluorescence is collected in a perpendicular direction. A very sensitive detector is used to collect the emitted light. An additional experiment can be done by introducing a polarizer in the path of the emitted light. The polarizer can be set as parallel or perpendicular to the incident radiation and any polarization effect in the emitted light can be determined.

Time resolved tera hertz (THz) spectroscopy:

THz spectroscopic studies have been carried out using a home built THz time domain spectrometer. The spectrometer uses output of a cavity-dumped Ti:Sapphire laser (λ_{max} = 780 nm, repetation rate = 2 MHz, average power ≈ 80 mW) pumped by a diode laser (532 nm, 4.6 W). As shown in Figure 2.2, the beam is divided into two parts using a beam splitter.[46]

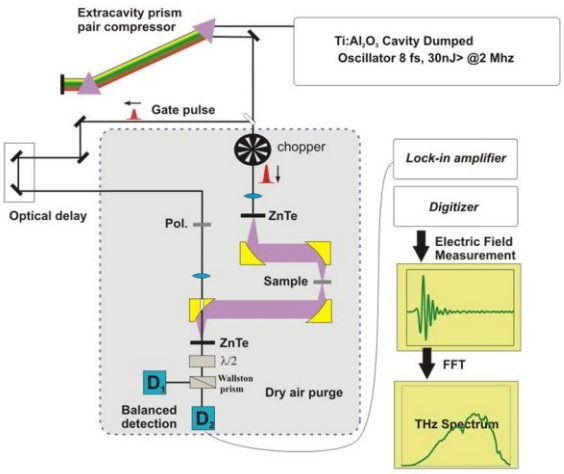

Figure 2.2 Time resolved THz spectroscopy set up.

About 75% of the beam (pump beam) is focused onto a 100 μm thick ZnTe crystal, which generates THz radiation *via* optical rectification. GaP crystals are also used for generating and detecting THz signal. The diverging THz radiation coming out of the crystal is collected, collimated, and refocused on a second GaP crystal using four gold-coated, off-axis, paraboloidal mirrors. The other 25% of the IR beam (gating beam) is focused on the second crystal for electro-optic (EO) sampling of the THz radiation. The electric field associated with the THz pulse induces a birefringence in the medium of the nonlinear crystal. The gating pulse beam from the EO crystal is passed through a quarter-wave plate and a Wollaston prism, which splits the pulse into two parts with different (vertical and horizontal) polarization. These two beams are fed into two biased photodiodes of a commercially available balanced detector. Any imbalance between the two detector inputs will lead to a net signal. The pre-amplified linear output of the detector is connected to a lock-in amplifier. The pump beam is modulated by using an optical chopper. The amplifier is locked to the chopping frequency, typically 1-2 kHz. The amplified signal is digitized and transferred to a computer for recording and analysis. A delay stage with a

typical step size of 3-5 μm is used to vary the delay between the THz pulse and the gating pulse. Hence, the entire THz pulse is mapped out by the gating pulse *via* electro-optic sampling.

Cyclic voltammetry (CV):

CV is an important analytical technique that can provide direct information about the energy levels of CdSe nanoparticles. CV characterization is carried out inside a glove box to eliminate any interference of moisture and oxygen as CV experiment of CdSe is sensitive to those elements. A schematic diagram of the experimental set up is shown in Figure 2.3.

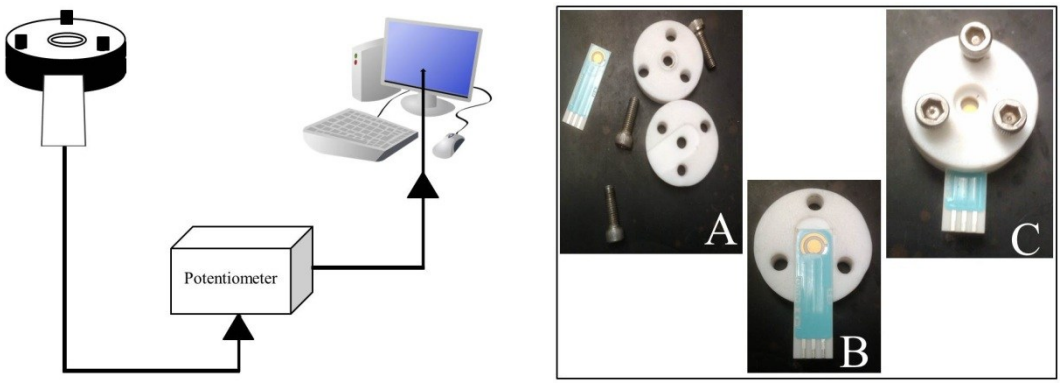

Figure 2.3 Experimental set up for cyclic voltammetry (left). Home built cell made by Ron Jackson and Joshua Shipman for CV measurements (right). All components of cells are shown in A and assembled cell is shown in C.

A homemade cell made of Teflon is used to hold nanoparticle solution. The advantage of using this homemade cell is that it needs very little amount of solution for the experiments. Gold screen printed electrodes are used where the working and counter electrodes are gold and the reference electrode and connectors are silver. The gold screen printed electrode is connected to a cord purchased from Dropsens (Model: BICAC 4mm-70005) and the other end of the cord is connected to the potentiostat.

In CV experiment, the potential of a working electrode is swept at a specific sweep rate (in volts/seconds) and current verses time curve is recorded. The sweep is reversed at some switching potential and data is again recorded. The sweep rate is kept constant in either direction and as the sweep changes direction at some potential, it is called cyclic voltammetry (CV). As sweep rate is constant in either direction, time can be replaced by the applied potential and CV diagram is represented as current *vs.* potential in the literature. A cyclic potential is applied to the

solution containing CdSe nanoparticles and the potentiostat records the current with changing potential.

Wide field microscopy:

Wide field microscopy is used to study the dynamics of NRs in polymer composite films. A schematic diagram of the experimental set up of wide field microscopy is shown in Figure 2.4.

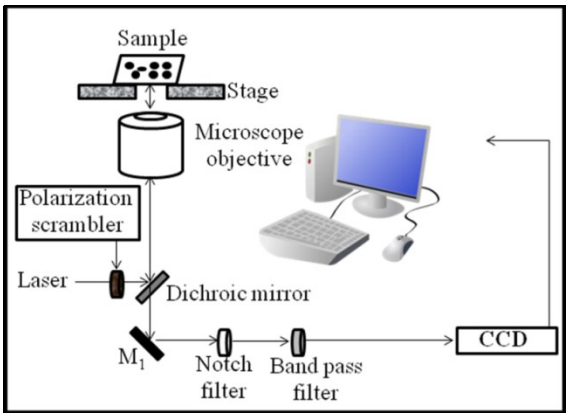

Figure 2.4 Wide field microscope for simultaneous study of blinking of many NRs.

A 532 nm laser is used for acquiring data as the excitation source. The incident light is passed through a polarization scrambler on to a dichroic mirror. Polarization scrambler is used to scramble the incident polarization of laser and this process eliminates any preferred incident polarization of light. Incident light is then guided to the microscope objective which tightly focuses the incident light to the glass cover slip that contains the sample. This incident light excites fluorophore to form excitons and they emit fluorescence upon recombination. The emitted light passes through the dichroic mirror and another mirror (M_1) is used to guide this fluorescence to the notch filter. The notch filter is a very important optic of this experiment as it blocks any scattered laser light and allows only fluorescence to reach the detector. A band pass filter is used in between the notch filter and the detector to select desired fluorescence out from rest of emission. The choice of band pass filter is made after recording the static fluorescence of the fluorophore and a band pass filter is used that has a band width in the range of peak maxima of the fluorophore. Only certain wavelength of light is allowed to reach to the detector which is in this case a CCD detector. The CCD is a sensitive detector. It is always a priority to start the

chiller connected to the CCD detector before start of the experiment. This instrument records movie of fluorophore under continuous illumination of laser and the movie images are analyzed by a MATLAB program. It is mentioned earlier that a polarization scrambler is used between the laser source and the dichroic mirror to scramble the incident polarization to remove polarization effects from the excitation laser. This polarization scrambler can be removed and perfectly polarized light can also be used depending on the requirements of experiments.

Single particle confocal microscopy:

Confocal microscopy is important in experiments where one need a very narrow spot size and high time resolution. The spot size of confocal microscope is about 380 nm, whereas, for wide field microscope it is in the range of microns. A tightly focused light source can provide information about small particles like NRs. The time resolution of confocal and wide field microscopy is set to be 20 ms and half second, respectively. These advantages come with one drawback and that is the loss of polarization of light. An experimental set up for single particle confocal microscopy is shown in Figure 2.5.

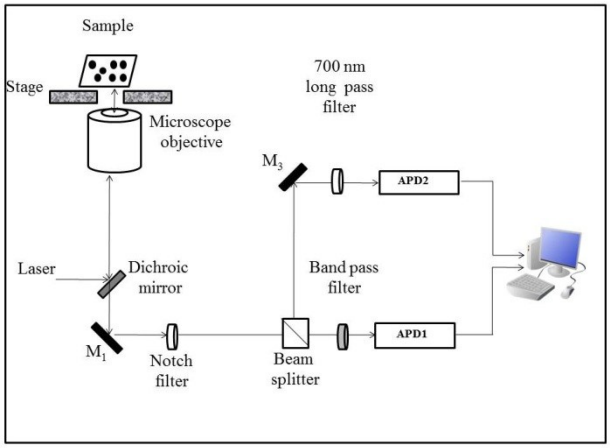

Figure 2.5 Single particle confocal microscope to study fast time transients.

A 532 nm laser is used for acquiring data as the excitation source. The incident light is passed through a dichroic mirror which guides the light to microscope objective which focuses the incident light to the glass cover slip that contains the sample. The emitted light passes through notch filter and band pass filter before it reaches to the APD (Avalanche photo diode) detector. A major advantage to work with confocal microscopy is that it provides flexibility to use a beam

splitter to divert the fluorescence light to two different APD detectors that can simultaneously collect data. If a fluorophore emits in two different wavelength and those two emissions are not close to each other, this method is very helpful. Two different filters can be used to monitor the dynamics of the band edge and trap state of CdSe nanorods simultaneously. Band edge emission is monitored by a 580-40 nm band pass filter, whereas, trap emission is monitored by a 700 nm long pass filter. Microscope objective is used to achieve a very small laser spot size. To achieve small spot size we sacrifice the polarization to a certain extent. The microscope objective behaves as a depolarization source as explained in Figure 2.6.

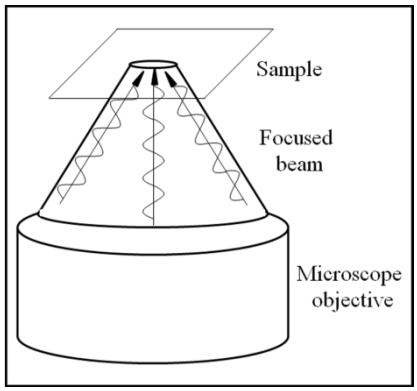

Figure 2.6 Microscope objective causes emitted light to depolarize.

The microscope objective helps to focus the polarized incident light to the sample. The incident light has a certain polarization before entering the microscope objective. When the incident light leaves the microscope objective it forms a cone shaped beam as shown in Figure 2.6. The polarization direction is different for light at the center of the cone than that of the light at the perimeter. In this situation there is a possibility of efficient excitation of NRs which are not parallel to each other and as a result of that the emission will be partially depolarized.

Chapter 3 - Progress Towards Producing n-type CdSe Quantum Dots: Tin and Indium Doped Quantum Dots

3.1 Introduction

After several decades, semiconductor quantum dots still remain in the focus of the scientific community. From the point of fundamental science, the initial thrust of quantum dot research mainly concentrated on the size control and the phenomena associated with size dependence.[47] The emphasis of the research gradually shifted towards achieving more delicate control over the quantum dot properties. Significant advancements include the control of the shape,[32,33] the surface of the quantum dots[4,48] and initiating their self-assembly to more practical structures.[49,50] These important developments of semiconductor quantum dot research have opened up a multitude of applications.[51] While these research areas continue to be important and relevant, one of the next frontiers of quantum dot research will focus on the inside of these quantum dots. Specifically, how foreign atoms affect the electronic structure of quantum dots during doping (incorporating a foreign atom into the semiconductor).[52-54] As expected, incorporation of dopants into semiconductor quantum dots will play a crucial role in curtailing the quantum dot properties. Doping makes the manipulation of the conductivity of the quantum dot possible (n and p-type material), which will facilitate the creation of quantum dot based p-n junctions. Critical components of this research are to find ways to circumvent challenges and understand the underlying mechanisms of doping of nanoparticles including quantum dots.

The challenges of doping semiconductor nanoparticles come from the lack of understanding of the science of the underlying principles of doping as well as from the technical difficulties to characterize the doped particles. While studying the nucleation of small metal crystals from binary metallic melts, Turnbull *et. al.*[55] suggested that doping of small crystallites would be difficult because small nuclei contain relatively few atoms. Specifically, dopants expected to be incorporated into quantum dots randomly, therefore, producing only a few doped particles with varying amount of dopants. Another important question is the stability of the dopant inside the quantum dots. Self-purification is expected to potentially affect the doped particles whereby the dopant is pushed to the surface of the quantum dots. Despite these difficulties, doped nanoparticles are successfully produced. Recently, Norris e*t. al.*[52] showed that

the above difficulties may not be applicable to Mn doped ZnSe nanoparticles, rather the morphology of the surface plays a crucial role during quantum dot synthesis. By manipulating the ratio of the Zn/Se, they have successfully increased ratio of the <001> facet, which resulted in increased absorption of Mn dopants. While the thermodynamic argument is useful if equilibrium conditions can be achieved, Norris[56] suggested that at lower temperatures growth kinetics via trapping the dopant can play an essential role in the incorporation of dopants into quantum dot.[57] Dopants not only can get trapped, but may activate the quantum dot surface to accelerate the monomer exchange rate, therefore, influencing the overall growth kinetics of the particles. Prior research in our group has recently showed that the addition of indium dopant increases the rate of magic-sized CdSe quantum dissolution kinetics.[58]

In addition to the conceptual difficulties, characterization of the doped quantum dots is complex. Determination of dopant concentration in the ensemble of quantum dots is straightforward, but per particle chemical analysis is rather challenging. Spectroscopic techniques *via* photoluminescence quenching offer indirect evidence of n-type quantum dots shown by Shim *et al.*[54] No similar method exists for p-type quantum dots. Static electrical conductivity measurements may contain ambiguities of the conductivities of individual quantum dots. Recently, the development of terahertz spectroscopy offers some hope to measure the increased conductivity of p or n-type quantum dots.[46] While terahertz measurements provide the AC conductivity (polarizability) of the doped quantum dots, extraction of such information is not straightforward if phonon resonances contribute to the measurements. In the case of Mn doped CdSe QDs, electron spin resonance is used to interpret the hyperfine splitting of the Mn^{2+} dopant.

In this research, we aim to explore the possibility of forming doped CdSe quantum dots using indium and tin dopants. By using high-resolution electron microscopy techniques, the presence of tin and indium dopant has been confirmed. Terahertz spectroscopic results suggest alloy formation in case of tin doped samples. Photoluminescence measurements clearly indicate increased temperature dependence of the doped samples in accordance with the expected n-type nature of the quantum dots. Time-resolved PL shows that the carrier dynamics is significantly different in the oxidized doped samples.

3.2 Experimental Section

Core-shell CdSe/ZnS particles are synthesized using two steps. In the first step, a single precursor $Li_4[Cd_{10}Se_4(SPh)_{16}]$ is used to grow CdSe quantum dots in the presence of hexadecyl amine (HDA). The $Li_4[Cd_{10}Se_4(SPh)_{16}]$ single source precursor is prepared according to the literature method.[22] In a typical synthesis, 25 g of HDA is placed in a three neck flask. 0.3 g of $Li_4[Cd_{10}Se_4(SPh)_{16}]$ precursor is placed on the top of the solid HDA to avoid exposing the precursor to direct heat from the heating mantle during the initial melting of the solid HDA. For the indium and tin doped CdSe quantum dots, an additional 10 mg of dopant (5 mol % $InCl_3$ or $SnCl_2$) are added along with the single precursor. The flask is purged under argon flow while slowly heated to 120 °C. The growth of quantum dots in solution is continuously monitored *via* an *in situ* fiber optic fluorescence setup. The *in situ* fluorescence setup consists of a Raman probe attached to the side of the reaction vessel. A 380 nm broadband light emitting diode is used to excite the quantum dots and the reflected photoluminescence (PL) is analyzed by a fiber optic spectrometer. The solution is stirred for 18 hours at 120 °C except the high temperature sample, which is kept at 250 °C. After 18 hours of quantum dot growth, the temperature is increased to 250 °C and is kept there for 2 hours to remove the remaining precursor molecules in the solution. During this temperature increase, fluorescence of the quantum dots falls below the detection limit of the apparatus. A solution made of 4.8 mL distilled TOP, 175 µL diethyl zinc and 26 µL hexamethyldisilithiane is added drop-wise to grow a ZnS shell around the doped nanoparticles. The ZnS shell is grown for 1 hour at 250 °C. When the ZnS solution is added, the quantum dot PL reappears as expected when the surface traps of the quantum dots are passivated. During the ZnS growth, the PL increased dramatically. PL of the quantum dot stabilizes after sometime, which indicates completion of ZnS shell growth. All chemicals are used as it is except HDA and TOP. Those are vacuum distilled at ~2 Torr. The ZnS solutions are prepared fresh for each synthesis.

The temperature dependent PL data are taken with *in situ* fluorescent setup described above without exposing the quantum dots to atmospheric oxygen and water. After 1 hour of ZnS shell growth at 250 °C, the heat is removed from the reaction vessel. The solution is stirred as it is cooled down to ~60 °C. PL spectra are collected. Once the temperature inside the vessel reached ~60 °C PL collection is stopped and the flask is reheated to 250 °C for 5 minutes and then cooled again to ~60 °C. While the PL is collected for the heating cycle as well, the cooling

resulted in smoother PL data due to the lack of the fluctuations induced by the heater. The process is repeated for a total of 10 cycles. Temperature data along with the spectral data are digitized. PL peaks are integrated to obtain quantitative data on the PL intensity. The PL is arbitrarily normalized to the PL intensity at 1/T = 0.00191 (250 °C).

High-resolution transmission electron microscopy (HRTEM) and energy-dispersive X-ray spectroscopy (EDX) of CdSe quantum dots are performed using a 200 kV FEI Tecnai F20 transmission electron microscope (TEM) with a field emission gun electron source. Holey carbon grids are used to prepare TEM specimens. For each sample, a droplet of toluene or methanol-based solution of quantum dots is casted on a holey carbon grid and the grid is evacuated for several hours before inserting it into the microscope. In order to evaluate the crystal structure of the quantum dots, HRTEM images are acquired from the dots oriented close to the $[11\bar{2}0]$ zone axis. This orientation enables direct imaging of stacking of hexagonal basal planes. Thus, the wurtzite structure can be easily distinguished from the zinc blend structure, and structural defects in the form of stacking faults can be readily imaged. For the EDX study, a nanoprobe of 1 nm in diameter is used. This study is performed in the scanning transmission electron microscopy (STEM) mode: High-angle annular dark-field (HAADF) STEM image of a selected specimen area is acquired first. The nanoprobe is then positioned at a specific quantum dot and an EDX spectrum is collected. Due to the low intensity of K-peaks and low concentrations of dopants in investigated CdSe quantum dots, long acquisition times of at least several minutes are required. To minimize any undesired effects caused by beam-induced decomposition of quantum dots, sample contamination and drift, the x-ray count rate as well as the shape of the EDX spectrum are monitored during the acquisition, and the nanoprobe is repositioned when needed. Spectra from several quantum dots, typically of the order of 50-100, are added together in order to increase the signal-to-noise ratio and to detect the K-peaks of tin or indium in doped quantum dots.

The terahertz time-domain spectrometer and the analysis has been described previously (Chapter 2),[46] but here is a brief summary. The spectrometer uses a cavity dumped output of a mode-locked Ti:Sapphire laser (λ_{max} = 780 nm, repetition rate = 2 MHz, average power = ~80 mW), pumped by a diode laser (532 nm, 4.6 W), for the generation and gating of the THz radiation. The laser is focused onto a 100 μm thick GaP (110) crystal which generates THz radiation via optical rectification. The entire THz pulse is mapped out by a small portion of the

laser pulse (gating pulse) via electro-optic sampling in another GaP crystal. The digitized signal is the time dependent electric field of the THz radiation. Its temporal Fourier transform yields amplitude spectrum in the frequency domain. The spectrum spans from 0.5 THz to 8 THz. The signal-to-noise (S/N) ratio obtained is ~500. To obtain the response of the sample to the THz radiation, two measurements are made. First, the THz electric field transmitted through the empty sample cell ($E_{cell}(t)$) is measured. Next, the THz field transmitted through the cell filled with sample ($E_{sam}(t)$) is recorded. Several measurements, typically 20-50, are averaged to obtain a reasonable S/N ratio. As the measured signal is the time dependent electric field, the complex Fourier transform of E(t) directly yields the complex refractive index of the sample. The quantum dots are dissolved in toluene along with polystyrene and thick quantum dot films are cast in polystyrene matrix. The absorption of the polystyrene in the spectral range is corrected for using effective medium approach, which is appropriate if the quantum dots are separated at relatively large distance compared to the frequency of light.

3.3 Results and Discussion

In this study, doping CdSe quantum dots with tin and indium are investigated. The synthesis of the quantum dots are carried out by a relatively low temperature (120 ºC) method using a single precursor of the CdSe. The photoluminescence of the quantum dots are monitored while the reaction proceeds in a 24 hour time period. The dopants are introduced from tin and indium chloride at 5±0.3 mol% relative to the cadmium concentration at the beginning of the synthesis. The experimental conditions (solvent to complex ratio) are adjusted so the size of the tin, indium doped and undoped CdSe quantum dots are the same within the experimental error. At the final stage of the synthesis, a ZnS shell is overgrown on the quantum dots to isolate the quantum dot from its environment. Figures 3.1(a-c) and 3.1(f-h) show the HRTEM images of indium and tin doped CdSe quantum dots, respectively. These quantum dots exhibit high crystallinity and are found to be formed in the wurtzite structure primarily. Structural defects in the form of stacking faults of the hexagonal basal planes, equivalent to the local zinc blend structure, are frequently observed, as seen in the HRTEM images, especially in the Sn-doped sample (Figure 3.1,f-h). More detailed interpretation of similar HRTEM images is given in

literature.[59] EDX spectra of indium and tin doped CdSe quantum dots are also shown in Figure 3.1.

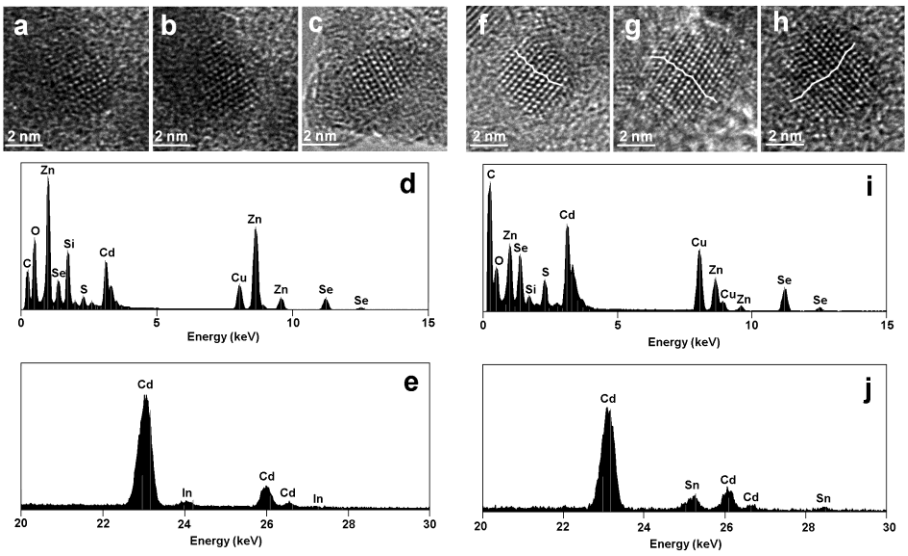

Figure 3.1 a-c HRTEM images and d,e EDX spectra of indium doped CdSe quantum dots. f-h HRTEM images and i,j EDX spectra of tin doped quantum dots. Twinning planes related to stacking faults and local switching from wurtzite to zinc blend structure are indicated in f-h.

From the lower-energy spectra, measured below 15 keV, it can be seen that the Zn/Cd peak intensity ratio in the indium doped sample (Figure 1d) is higher than the one measured in the tin doped sample (Figure 3.1i), suggesting slightly thicker ZnS shell in the former case. The low-energy part of the EDX spectrum (below 5 keV), also contains the information about the dopants as the characteristic X-ray L-peaks of In and Sn appears there. The extraction of the dopant information from this part of the spectrum is difficult as both the In and the Sn L-peaks greatly overlap with the much stronger Cd L-peaks. Therefore, in order to study the incorporation of indium or tin into CdSe quantum dots, EDX spectra are also measured in the higher energy range between 20 and 30 keV, where well-separated K-peaks of Cd, In and Sn appear. This establishes the incorporation of indium and tin into CdSe quantum dots as shown in Figure 3.1d and 3.1j, respectively. In the indium doped sample, the dopant concentration is found to fluctuate significantly from particle to particle, whereas it is more stable in the tin doped sample. The EDX quantification yields approximately 11 ± 1 mol % and 5 ± 0.5 mol % average dopant concentration in the tin and indium doped quantum dots, respectively.

Figure 3.2 presents similar HRTEM and EDX results obtained from undoped CdSe quantum dots and quantum dots produced during 'high-temperature' indium doping at 250 ºC. The nanostructure of these quantum dots, as revealed by HRTEM study, resembles that of tin or indium doped quantum dots. Again, quantum dots are formed primarily in the wurtzite structure, however, numerous basal stacking faults are observed, especially in the In-doped sample (Figure 3.2f-h). Lower-energy EDX spectra of these samples indicate significantly high Zn/Cd ratio and thick ZnS shell (Figure 3.2d,i). No indium peaks were detected in quantum dots from the high-temperature doped indium sample (see Figure 3.2j). The higher-energy spectrum of this sample resembles the spectrum measured for undoped quantum dots (Figure 3.2e): only Cd K-peaks are visible there with no significant trace of In peaks.

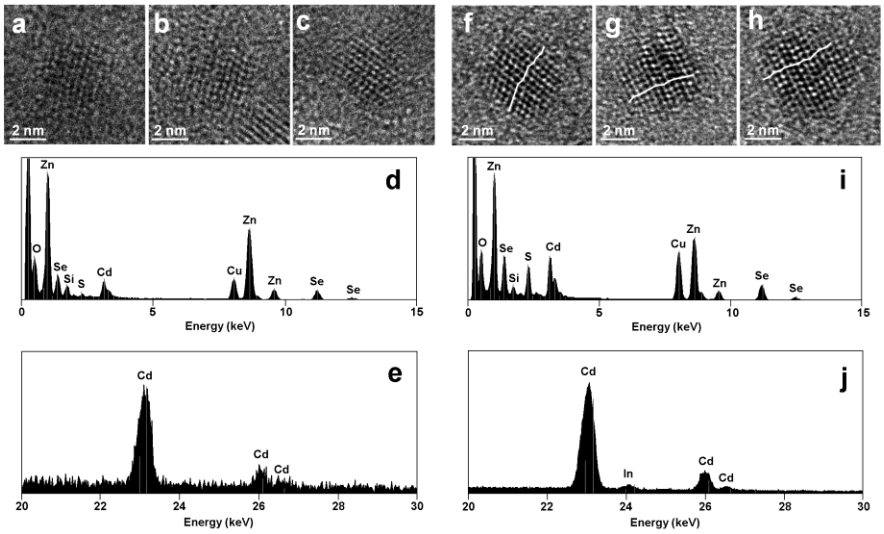

Figure 3.2 a-c HRTEM images and d,e EDX spectra of undoped quantum dots. f-h HRTEM images and i,j EDX spectra of indium doped samples grown at high temperature (see text). Twinning planes related to stacking faults and local switching from wurtzite to zinc blend structure are indicated in f-h.

The dopants loaded into the reaction mixture may yield varying amount of dopants per particles.[60] The statistical theory below describes the simplest case of doping and any deviation from it is interpreted as a clue to the underlying mechanism of doping in the specific case. When uniform concentration of dopants is introduced into a solution during the growth of quantum dots, the probability of doping depends on the dopant concentration and the radius of the

quantum dot. The probability of a given number of dopant (k) occupying a quantum dot with volume V is determined by the Poissonian distribution (eq. 1):

$$P(k) = \frac{e^{-Vn}(Vn)^k}{k!} \qquad \text{(eq.1)}$$

where, n is the dopant concentration given in $1/m^3$. The results predicted by the statistical theory are summarized in Figure 3.3.

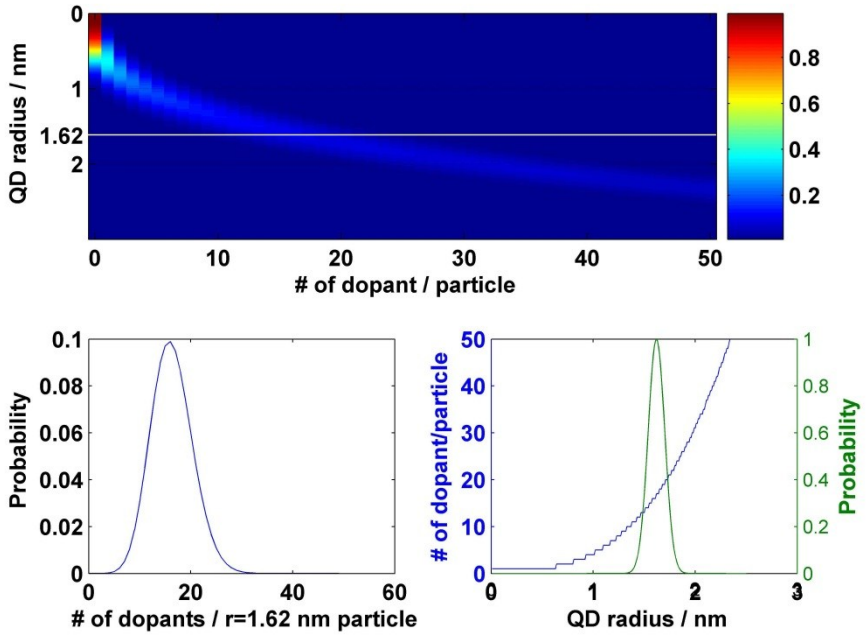

Figure 3.3 Upper: Statistical calculation of dopant distribution as a function of quantum dot radius from the Poissonian distribution for 5 mol% uniform dopant concentration. Lower left: Probability of dopant occupation of a quantum dot with a radius of 1.62 nm. Lower right: The effect of size distribution of most probable dopant occupation of a quantum with a radius 1.62 nm and 10 % size distribution.

In these calculations, the quantum dots are assumed to be spherical and the dopant concentration corresponds to the experimentally used dopant concentration (5 mol%). Figure 3.3 (upper) shows how k (number of dopant /particle) changes with the size of the quantum dot. According to this theory, as the particle becomes larger, the probability of doping increases. For the experimental size of the CdSe quantum dots (r = 1.62 nm), the predicted dopant distribution for this size is shown in Figure 3.3 (lower left). From the peak maximum of the probability distribution, the number of dopants per particle is approximately 17 dopants. Since the nanoparticles have a finite

size distribution of approximately 10%, it is expected that the maximum of the probability distribution number varies within the size distribution. Figure 3.3 (lower right) shows how the most probable dopant changes over the size distribution of the particles. The very small quantum dots will have only a few dopants, while the larger quantum dots may have twice as many dopants. These numbers are relatively high compared to bulk doping values, but not all dopant would be active in case of quantum dots. The theory predicts that it is more likely for larger particles to have the 'right' dopant that could ionize more efficiently.[61] Due to the limitation of the analytical technique used to determine the dopant number/particle in this experiment, the size selective correspondence between theory and experiment cannot be established at this point. However, the experiment above shows that tin dopants preferentially incorporate into the quantum dots during growth, while the measured concentrations of indium dopants agree well with the statistical theory.

Efros *et. al.*[57] have suggested that a dopant may be incorporated into a quantum dot *via* 'trapping' at a particular location. The requirement of doping is that the dopant binding to the surface is strong compared to the thermal energy, and the dopant-surfactant complex easily dissociates on the surface of the quantum dots. The data show that there is indium doping when the quantum dots are grown at low temperature, and indium is also incorporated into the quantum dots synthesized at 250 ºC at the same concentration level. Based on the growth conditions, the activation energy of the dopant desorption must be very small. Efros *et. al.* also pointed out the role of the surfactant-dopant complex, which cannot be too strong under the experimental conditions; therefore, the 'usual' phosponic acid based synthesis of II-VI quantum dots would yield strong dopant-phosponic acid complexes. Following this argument, in this study, the quantum dots are synthesized in the presence of hexadecyl amine, which is also proven to be a better solvent for manganese doping of CdSe quantum dots.[52]

While the indium doped samples show statistical distribution of the dopant, the tin doped samples indicate a different mechanism that leads to the preferential adsorption of tin. Figure 3.4 shows the experimentally measured terahertz absorbance of the doped and undoped quantum dots. The main feature in the THz absorbance spectra of the CdSe quantum dots is a strong resonance at ~5.75 THz (~ 192 cm^{-1}). This strong absorbance peak is due to a coupled mode between longitudinal optical (LO-211 cm^{-1}) phonon and transverse optical (TO-169 cm^{-1}) phonon modes, namely the Fröhlich mode, and has been observed earlier in simple far-infrared

spectra for small CdSe nanoparticle ensembles.[62] The frequency of this particular mode exhibits modest size dependence. For smaller particles, in addition to the Fröhlich mode, there are some other confined coupled vibrational modes which can be observed in the THz spectrum as observed in the earlier study.[62] The Fröhlich mode in the small CdSe QD seems less intense and broadened, but this behavior is expected due to mode splitting. The data indicates a slight shift in the Fröhlich mode (15 cm^{-1}) of the tin doped CdSe QDs.

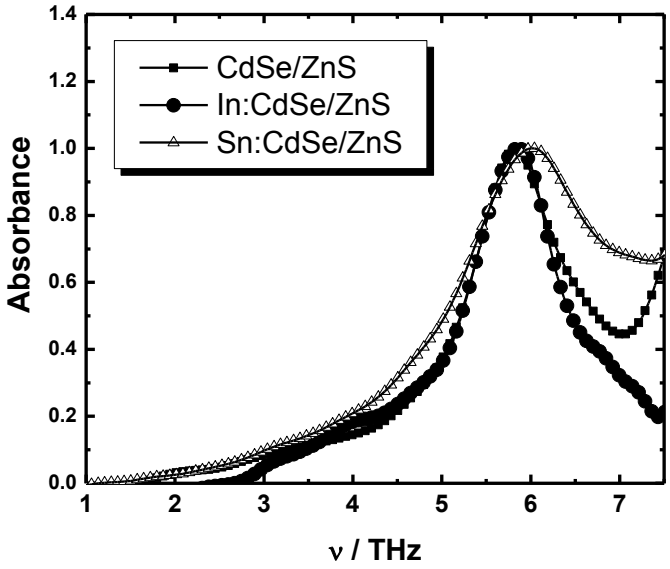

Figure 3.4 Terahertz time-domain absorption of the undoped, indium and tin doped CdSe/ZnS core/shell quantum dots

This shift can be interpreted as alloy formation on the surface of the CdSe quantum dots reducing the CdSe core size, which in turn increases the frequency of the resonance. Other explanations of the shift are also possible such as the modification of the phonon frequency due to alloy formation with tin. The indium doped sample does not exhibit the same behavior, but seem identical to the undoped samples within the instrumental resolution, which seems to support that the mechanism of tin and indium doping is different. Recent experimental data indicate that the indium incorporation into bulk CdSe is without the formation of a secondary phase up to 5 mol% of indium, therefore CdSe and indium tends to form a dilute alloy.[63,64] There is no evidence to the authors's knowledge about tin doping in CdSe.

Figure 3.5 shows the absorption and photoluminescence (PL) spectra of the CdSe quantum dots. The emission peak width of the undoped sample is noticeably narrower than the doped samples.

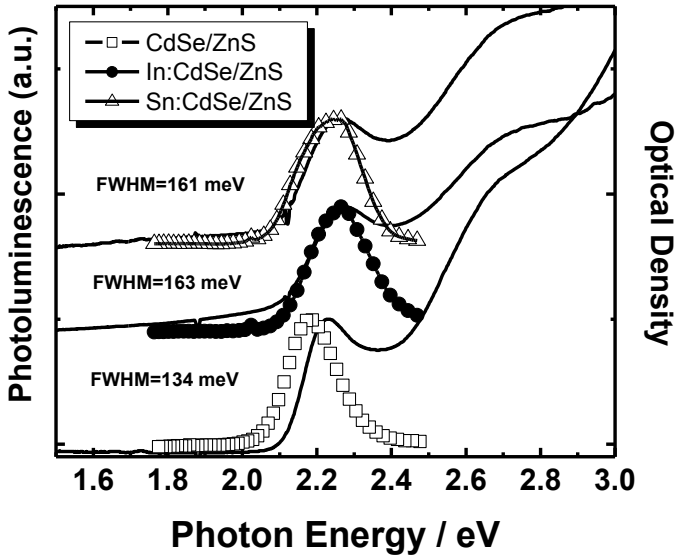

Figure 3.5 Absorption and photoluminescence spectra of undoped, indium and tin doped CdSe/ZnS core/shell quantum dots

The difference is mainly due to the effect of the dopant on the growth kinetics. Previous results[58] showed that the size distribution undergoes focusing during growth. As the dopant accelerates the growth, the doped samples cross the narrower distribution sooner resulting in a larger size distribution. Therefore, the broader distribution is not the result of the heterogeneous nucleation. The size of the quantum dots are controlled primarily by the initial amount of precursor complex measured in the reaction mixture, and the reaction proceeds until most of the precursor molecules are consumed over the period of the reaction (18 hours). Both tin and indium doped samples exhibit no or little Stokes shift. The results indicate that lack of the Stokes shift is the direct result of doping. While in undoped CdSe the origin of Stokes shift is explained via dark states that are not allowed for direct 1 photon absorption, clearly is absent here. The conclusion is that the dopant levels are significantly altered the selection rules of the absorption and

emission. As it will be shown later, the lack of Stokes shift could be the result of backfilling of the electron resulting in a more pronounced bright state emission.

Immediately after the synthesis and the overgrowth of ZnS shell, the temperature dependent photoluminescence of the quantum dots is measured in the temperature range of 343-524 K. The measurement takes place in the reaction vessel under argon to minimize the possibility of oxidation of the doped quantum dots.[54,56] This precaution is needed as predicted previously (Chapter 2).[56] In addition, measurements of the photoluminescence are carried out after addition of the ZnS shell that isolates the particles from their environment. The results of the temperature dependent photoluminescence studies are summarized in Figure 3.6.

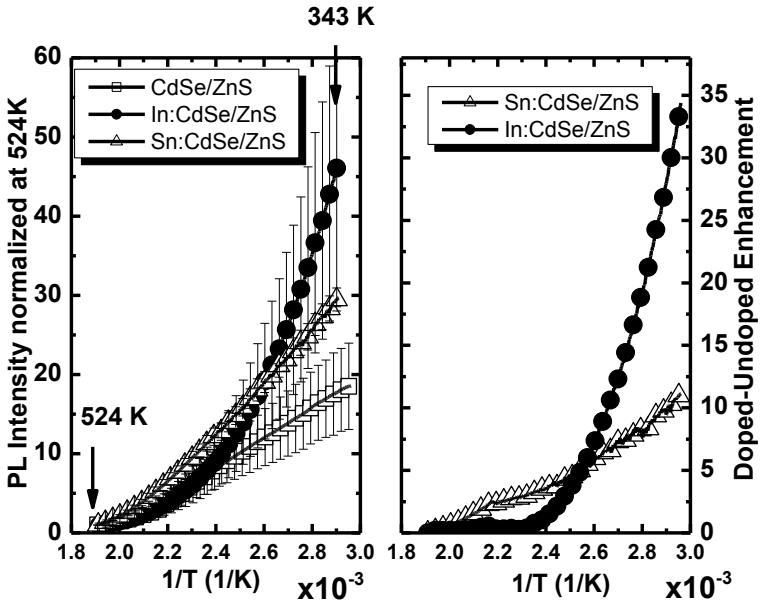

Figure 3.6 Left: Temperature dependent photoluminescence spectra of undoped, indium and tin doped CdSe/ZnS core/shell quantum dots between 524-343 K normalized to 1 at 524 K for comparison. Right: Same as the left, but the undoped photoluminescence is subtracted from the doped samples

Each curve represents the average of the 10 cycles and is normalized at 524 K for better visibility. All the curves show decreased PL with increasing temperature (or decreasing inverse temperature). The integrated PL of the undoped sample changes by a factor of approximately 18.5 between 343-524 K. In the same temperature range, the PL of tin and indium doped CdSe samples change by a factor of 29.5 and 47, respectively. Clearly, the PL of the doped samples

has steeper temperature dependent curves. Figure 3.7 shows a complementary calculation to predict the PL quenching due to the presence of $1S_e$ electron in a 3.25 nm CdSe quantum dot in the experimental temperature range. The calculation uses a simple Fermi-Dirac statistics (eq. 2) to quantify the PL quenching via occupation probability of the $1S_e$ level from the dopants.

$$n_i = \frac{1}{e^{(E_i - E_{Fermi})/kT} + 1} \qquad \text{(eq. 2)}$$

Where, n_i is the carrier concentration, k is Boltzmann constant, T is temperature, E_i is energy of carrier and E_{Fermi} is the Fermi energy.

The plot in Figure 3.6 assumes that the PL quenching is inversely proportional to the occupation probability ($1/n_i$) of the $1S_e$ level relative to the undoped quantum dot.

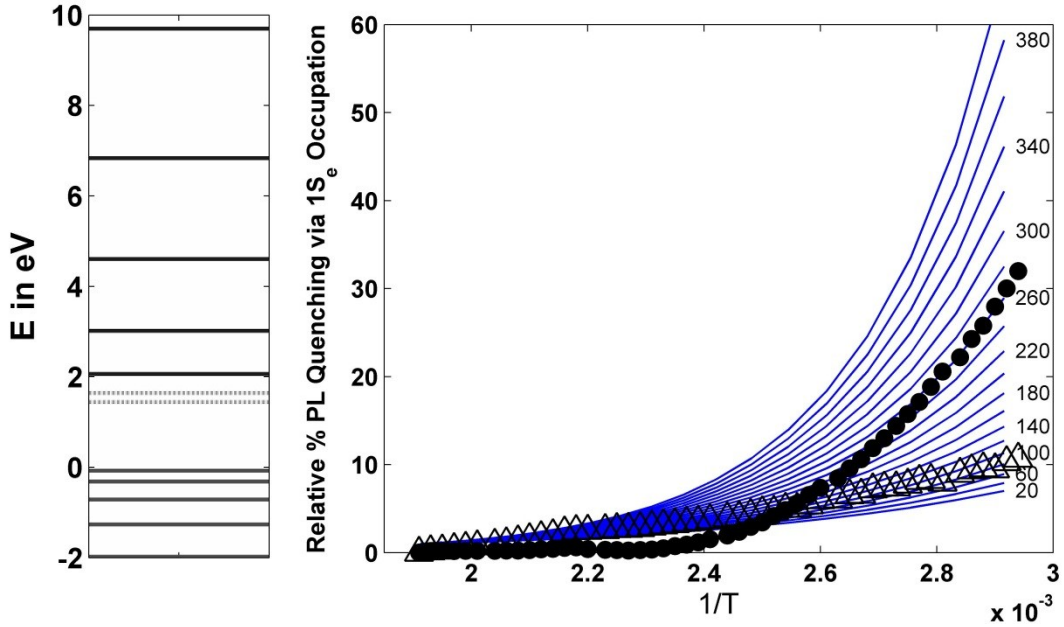

Figure 3.7 Calculated photoluminescence quenching based on the occupation of the 1Se level of the CdSe quantum dot from Fermi-Dirac statistics (see text). The dopant level is varied between 20 to 400 meV below the conduction bandedge (some dopant levels are indicated on the graph). The data are normalized to 1 at 524 K and shown in the same temperature range as the data in Figure 6. In addition the experimental data of the indium (solid circle) and tin doped (empty triangle) CdSe samples are also plotted.

The energy diagram of Figure 3.7 (left) indicates the quantum confined hole and electron levels derived using the effective mass of the hole (0.45 me) and electron (0.112 me) in CdSe. The dopant levels are critical parameters in the calculation to determine the steepness of the PL

quenching curve. For the data presented here, dopant levels below the bulk conduction band are assumed to be between 20-400 meV to approximately match the experimental data. The calculated PL quenching is normalized at 524 K in order to directly correlate the calculation with the experiment. Both experiment and calculation indicate that the PL quenching increases at lower temperatures in the case of the indium and tin doped CdSe quantum dot samples. The calculation also predicts that as the dopant energy level forms deeper below the conduction band, the temperature quenching of the PL becomes steeper. The calculation is highly approximate for several reasons. It assumes only a single dopant level (as opposed to a distribution of dopants that accounts for the random nature of doping). It is expected that the dopants occupy several sites corresponding to different energy levels as well as the actual signal is the result from an ensemble of quantum dots (doped and undoped). The quantum dots contain a thin ZnS shell, which could contribute to the density of states above the dopant level. This later shortcoming is expected to be a lesser effect, because the quantum confined levels of ZnS conduction bands are significantly higher due to the band matching and quantum confinement. In conclusion, the calculation predicts that the tin and indium energy levels form approximately 100 meV and 280 meV below the bulk conduction band, respectively.

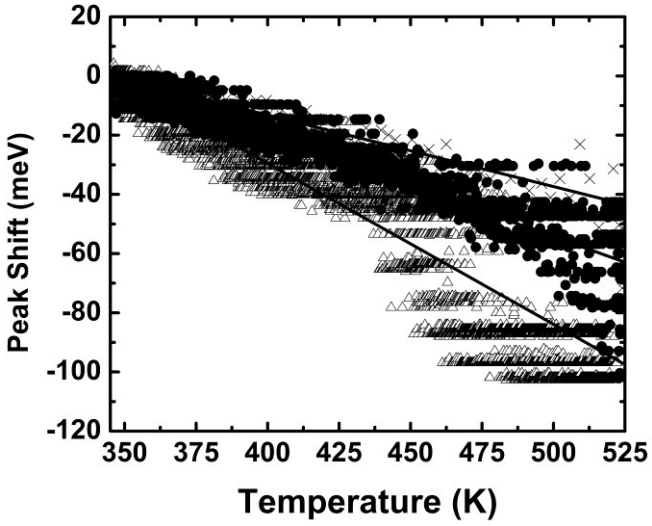

Figure 3.8 Stokes shift of the undoped (cross), indium (solid circle) and tin doped (empty triangle) CdSe samples in meV as function of temperature. The solid lines represent linear fit to the data.

If electrons from the dopant levels are available for the quantum dots, one would expect backfilling of the lowest energy levels resulting in change of the optical emission. This backfilling will be temperature dependent. In CdSe, near the bandedge, there are several excitonic states from which a dark excitonic state is responsible to the Stokes shifted emission. In Figure 3.8, the PL peak maximum is shown against the temperature. In both doped samples, the peak maximum changes steeper than undoped sample. This steeper dependence could be very well the results of backfilling. In addition, the lack of Stokes shift in doped sample points towards this conclusion. Shim *et. al.*[54] have shown that the optical absorption is also influenced by the backfilling resulting a shallow onset in case of n-type CdSe QDs. A similar feature is observed in Figure 3.5, but with diminished intensity. The doped samples exhibit an extended onset in the optical absorption spectrum.

Time-resolved photoluminescence kinetics of the bandedge emission of the freshly prepared doped and undoped samples are measured, which show that the photoluminescence is dominated by a long (~35 ns) component. No significant difference could be observed between doped and undoped samples. After several days the doped samples undergo oxidation while the undoped samples remain unchanged. The time-resolved photoluminescence of doped and undoped samples are presented in Figure 3.9.

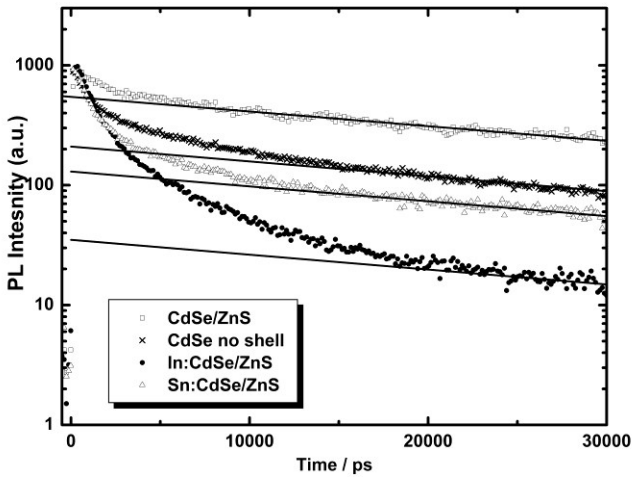

Figure 3.9 Time-resolved photoluminescence of several-days-old undoped, indium and tin doped CdSe/ZnS core/shell quantum dots. As a reference a quantum dot sample without shell is also shown, which lack the large component multi-exponential decay of the indium doped CdSe sample.

The photoluminescence dynamics of the doped and undoped samples exhibit distinctly different kinetics. The kinetics of the undoped CdSe sample shows a small component of fast decay and a relatively large component of slow decay that can be fitted with a ~35 ns single exponential. Both indium and tin doped samples display very different kinetics from the undoped samples and their PLs are dominated by fast relaxation components. It is obvious from the logarithmic plot that these curves cannot be fitted with a single exponential decay function, but multiple exponential components are needed to obtain a good fit. Because of the lack of the uniqueness of the fit, the data are not presented here quantitatively. Interestingly, the component of the 36.7±0.2 ns decay is present in each of the samples in Figure 3.9, which might mean that undoped quantum dots are present in all samples. As a reference, an undoped sample is prepared (same size as the rest) without ZnS shell, which shows still significant ~35 ns relaxation component compared to the doped samples. This comparison suggests that the observed fast relaxation kinetics is due to the indium and tin induced oxidation of CdSe quantum dots.

The excitation anisotropy (r) of the same samples is shown in Figure 3.10 (left).

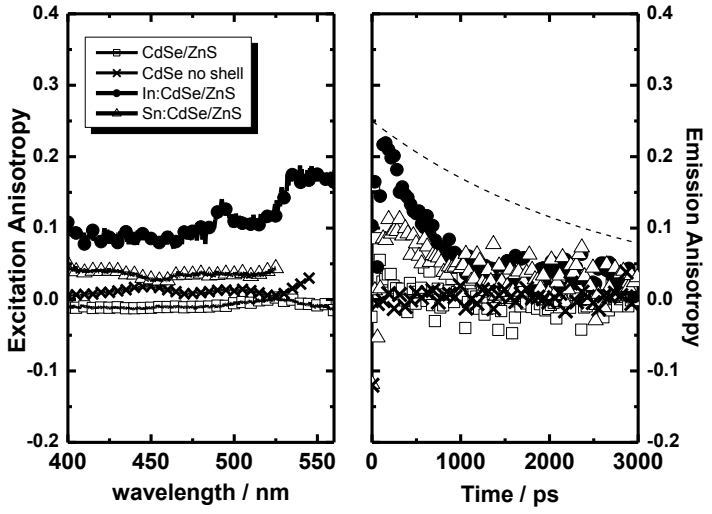

Figure 3.10 Left: Excitation anisotropy of several-days-old undoped, indium and tin doped CdSe/ZnS core/shell quantum dots detected at the bandedge photoluminescence (570 nm). Right: Time-resolved emission anisotropy of several-days-old undoped, indium and tin doped CdSe/ZnS core/shell quantum dots detected at the bandedge (570 nm). The dashed line shows the calculated rotational diffusion time of a sphere with the same radius as the size of the quantum dots.

By definition $r=(I_{par}-I_{per})/(I_{par}+2*I_{per})$, where 'I' is the PL intensity along parallel and perpendicular detection to the excitation polarization. The detector is set at the bandedge emission of the quantum dots and the excitation wavelength is scanned from 400 nm. The indium doped CdSe sample displays the largest positive anisotropy values for bandedge emission, while the anisotropy is decreasing in the order of tin, no shell and undoped CdSe/ZnS quantum dots. Again the freshly prepared tin and indium doped samples are very similar to the undoped samples showing no appreciable emission anisotropy as expected for spherical CdSe QDs. In agreement with the static anisotropy measurements, the time-resolved emission anisotropy (Figure 3.10 right) exhibit positive values of anisotropy in the same order. It should be noted that static anisotropy is the ratio of the time integrated anisotropy and the time integrated PL. Therefore, the relatively short photoluminescence lifetime of the indium doped CdSe combined with the large initial amplitude of the anisotropy results in the large static anisotropy values. In summary, the tin and indium doping induced oxidation has resulted in polarized emission if the quantum dots are excited (3.08 eV) significantly above bandedge (~2.2 eV). Decay time of the anisotropy of the samples is shorter than expected. The rotational diffusion time of 3.25 nm sphere in toluene is calculated to be 2583 ps, which is indicated also in Figure 3.10 (right) by dashed line. Obviously, the emission is depolarizing faster than the rotational diffusion time of the quantum dot, which requires other sources of depolarization. A plausible explanation is the contribution from trapping dynamics, which does not stop after few picoseconds, but continues to be a factor. While the hole relaxation levels are typically faster due to the larger effective mass, it is assumed that the primarily the electron relaxation levels are affected leading to the relatively large observed anisotropies.

3.4 Conclusions

In conclusion, CdSe quantum dots are doped with indium and tin dopants. The presence of the dopants is confirmed on a per particle bases. From the data it is concluded that the indium and tin doping takes place *via* different mechanisms. The dopant significantly changes the electronic structure of the quantum dot. Temperature dependent PL becomes steeper depending on the relative energy level of the dopant in agreement with the predictions. The PL dynamics indicate the retention of polarization in the aged doped quantum dots. The indium doped samples

appear less stable even when covered with the ZnS shell, which leads to a new challenge of exploring ideas to stabilize quantum dots in the presence of strongly reducing dopant electron.

Chapter 4 - Cyclic Voltammetry of Undoped and Doped CdSe Quantum Dots

4.1 Introduction

CdSe quantum dots are quantum confined materials and like any other quantum confined materials they have discrete energy levels. The energy gap between highest occupied molecular orbital (HOMO) and lowest unoccupied molecular orbital (LUMO) is defined as band gap. The band gap of CdSe quantum dots can be tuned by changing the size of the quantum dots or introducing dopants to it.[65] This characteristic of CdSe made it a unique candidate for photovoltaic application. It is always a significant interest to utilize an analytical technique that gives direct information about HOMO and LUMO of CdSe quantum dots. Cyclic voltammetry is an analytical technique that employs mild experimental conditions and can provide information about HOMO and LUMO levels of CdSe quantum dots. As mention earlier, quantum dots have discrete energy levels and are expected to undergo electron transfer through valance bandedge and conduction band edge. Thus, anodic and cathodic peak can be assigned to LUMO and HOMO respectively and this concept is discussed by Inamdar *et.al*.[66]

One of the challenges associated with this research is that the ligands on the quantum dots are non-polar and will not dissolve in polar solvents like toluene. However, this challenge can be overcome by introducing polar solvents that are electrically conductive to effectively characterize the electrical properties of a sample. As a result, the samples are dissolved in non-polar toluene and then mixed with polar N,N-dimethyl sulfoxide (DMSO) and a supporting electrolyte (Tetrabutylammonium perchlorate (TBAP)). A different way to get rid of the non-polar ligand is to dissolve the ligand by chemical etching.[67] Another challenge associated in this experiment is the presence of moisture and oxygen in the air and this problem is overcome by carrying out entire experiment in oxygen and moisture free glove box. It is difficult to introduce the potentostat inside the glove box and to overcome this challenge a connector (purchased from Dropsens, Model: BICAC 4mm-70005) is used to connect the cell with the potentiostat. The ends of the electrodes are connected correctly to get useful result.

The advantage of working in this instrument is that it is very sensitive and requires very little amount of solution for experiment. A cell was developed to take measurements that

minimized the amount of solution used and a schematic representation of the cell is provided in Figure 4.1.

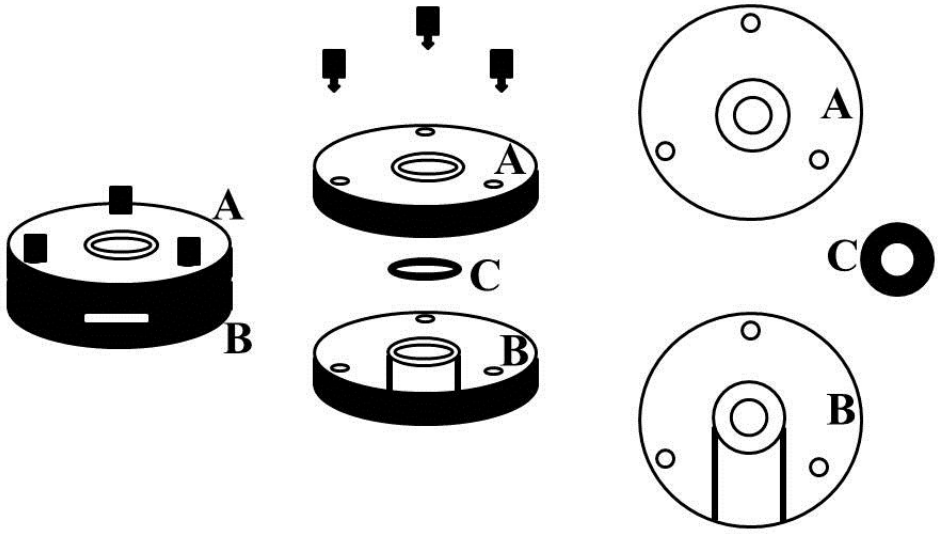

Figure 4.1 Diagram of cell used to contain gold printed electrode and test solutions. A) This is the well to hold QDs solution. B) This is the slot for the gold electrode and (C) is the o-ring used to seal part (A) and (B).

4.2 Synthesis of CdSe Quantum Dots

Synthesis of undoped and doped CdSe quantum dots are done as the method described in chapter 3 and section 3.2.

4.3 Experimental Section

Purification of CdSe quantum dots:

Undoped and doped CdSe quantum dots are purified with methanol and toluene. Methanol is used to dissolved the excess HDA (hexadecyl amine) remaining after the synthesis. The solution is then centrifuged and supernatant is discarded and this process is repeated several times. After

several washings the centrifuge tube containing quantum dots is placed inside a vacuumed chamber to remove excess methanol. The resulting quantum dots are dissolved in toluene and subjected to CV measurement.

Sample preparation for CV measurement:

DMSO is added to the solution of CdSe quantum dots in a 4:1 ratio of toluene. TBAP is added as a supporting electrolyte in very low concentration (100 mMol).[66] The cell is assembled as shown in Figure 4.1 and few drops of solution containing quantum dots are added to the groove of the cell. Gold screen printed electrodes (purchased from DropSens, Model: DRP-C220AT) are used where the working and counter electrodes are gold and the reference electrode and connectors are silver.

4.4 Results and Discussion

Figure 4.2 shows current verses potential profile of six different sized undoped QDs.

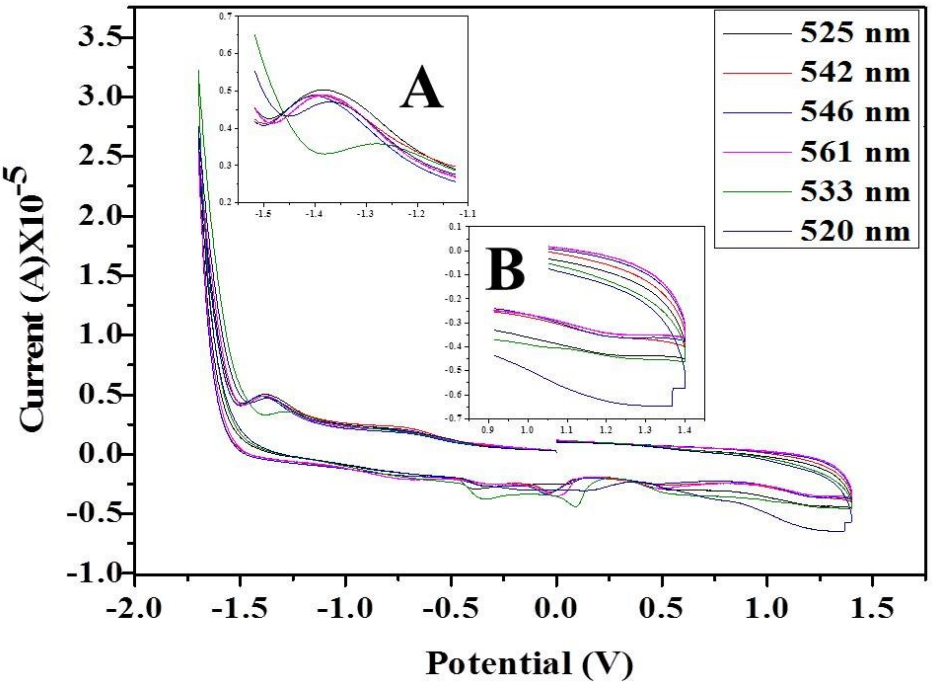

Figure 4.2 Current verses potential plot of QDs. Insets show anodic (A) and cathodic (B) peak.

Current value is recorded while changing input potential in cyclic manner. Initial and final potentials are set to be zero volts. Maximum and minimum potentials are set to be at 1.4 volts and -1.7 volts respectively. The potential decreases continuously from 0 V and when it reaches -1.7 V, it starts increasing till 1.4 V and finally it again starts decreasing until it reaches 0 V. Thus it completes a full cycle of potential change. Six different size undoped QDs are synthesized and they are represented with their absorption peak maxima. Anodic (Figure 4.2 inset A) and cathodic (Figure 4.2 inset B) peaks are observed from the CV experiments of QDs. It is observed that anodic peak is much stronger and sharper than that of cathodic peak for all the samples. The location of the peaks of the anodic and cathodic peaks are consistent with the observations presented in the previous work.[66] Oxidation and reduction are associated with anodic and cathodic peak respectively. Oxidation occurs when an electron is removed from valence band of QDs and that happens at very low potential. Therefore, anodic peak can be associated with valence band. Similarly, reduction occurs when an electron is added to the conduction band of QDs and that happens at very high potential. Therefore, cathodic peak can be associated with conduction band. Thus, information about valence band and conduction band can be determined by CV measurement. Valence band and conduction band potentials are determined along with absorption of corresponding QDs. Absorption peak maxima and valence band and conduction band potentials are tabulated below (Table 4.1).

Peak maxima of CdSe QDs	Valence band (V)	Conduction band (V)
520	-1.387	1.228
525	-1.4	1.225
533	-1.396	1.22
542	-1.359	1.241
546	-1.381	1.247
561	-1.363	1.275

Table 4.1 Valence band and conduction band potential of QDs.

The potential of valance and conduction bands are plotted for different QDs (Figure 4.3). Absorption peak maxima is an indicator of size of QDs as it is known that absorption peak

maxima shows bathochromic shift with decrease in QDs size. It is expected that band gap would increase with decrease in QDs size and that can be observed in Figure 4.3.

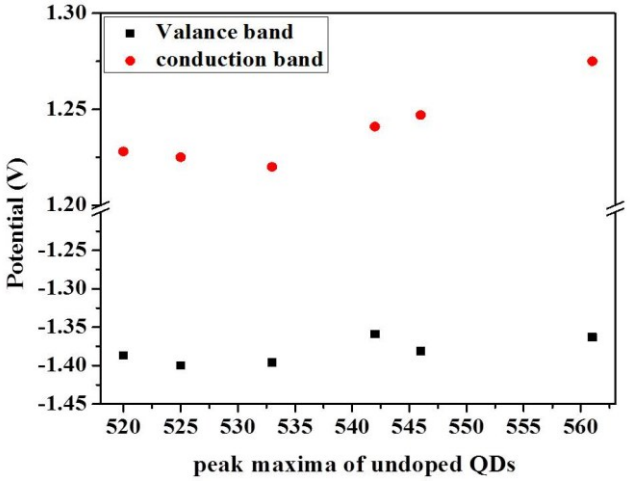

Figure 4.3 Potential of valance and conduction bands of undoped CdSe quantum dots determined from CV measurement plotted against the optical bandgap.

QDs are doped with gallium and their CV diagram is presented (Figure 4.4).

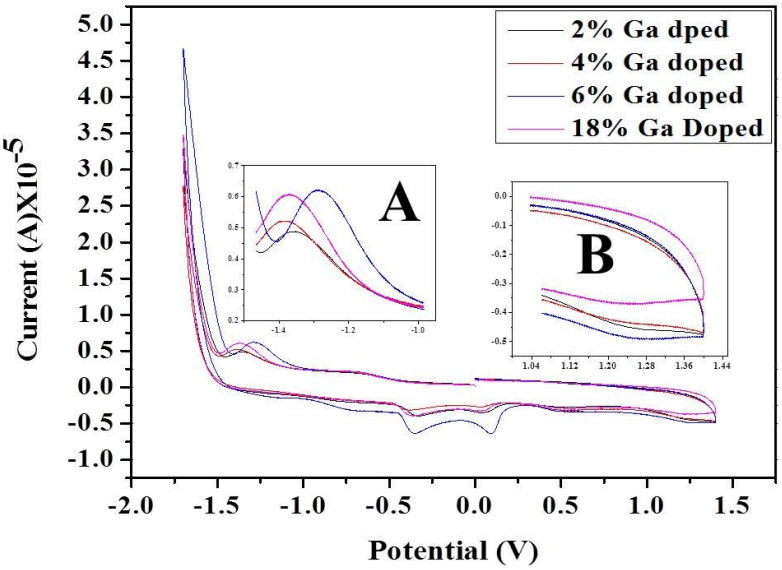

Figure 4.4 Current verses potential plot of QDs. Insets show anodic (A) and cathodic (B) peak.

Experimental parameters for this experiments are kept same as that of undoped QDs. Current verses potential of four gallium doped samples are recorded (2%, 4%, 6% and 18% gallium doped QDs). Anodic (Figure 4.4 inset A) and cathodic (Figure 4.4 inset B) peaks are observed

from the CV experiments of gallium doped QDs. Similar to the undoped QDs, valence band and conduction band potentials are recorded and shown in Table 4.2 (8%, 10%, 12% gallium doped QDs data taken from REU student Joshua Shipmen).

Percentage of Ga dopant	Valence band (V)	Conduction band (V)
2	-1.342	1.27
4	-1.369	1.27
6	-1.288	1.271
8	-1.35	1.28
10	-1.381	1.231
12	-1.371	1.256
18	-1.366	1.249

Table 4.2 Valence band and conduction band potential of gallium doped QDs.

Valence band and conduction band potential are plotted for all gallium doped sample (Figure 4.5).

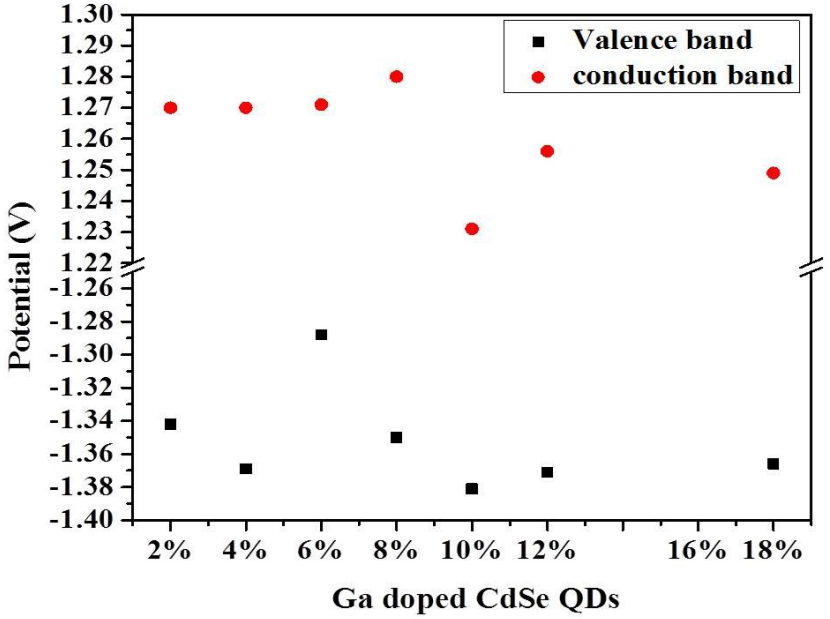

Figure 4.5 Potential of valance and conduction bands of gallium doped CdSe quantum dots.

Band gaps of gallium doped QDs show different behavior than that of undoped QDs. It is difficult to extract a general trend of change in band gap with different doping concentration. It can be hypothesized that doping is a completely random process and thus it does not show any general trend of band gap change.

4.5 Conclusions

CdSe QDs of different sizes and doped QDs of different gallium concentrations are prepared. Cyclic voltammetry experiment of undoped and gallium doped QDs are carried out in a custom made cell and in air and moisture free environment. The data obtained from undoped CdSe quantum dots shows no significant variation in band gap of QDs within the size range of CdSe QDs investigated. The gallium doped CdSe QDs exhibit slightly higher potentials in contrast the undoped CdSe QDs. This behavior is expected and most likely due to the n-type of character of these QDs.

Chapter 5 - Fluorescence Intermittency of Undoped and Indium Doped CdSe Quantum Dots

5.1 Introduction

CdSe nanocrystals are of great interest for making better solar cell application due to their high photo-stability, ease of preparation and low cost of production. The important features required for a good solar cell material are a) efficient production of excitons, b) charge formation from the excitons and c) transportation of the charge to anode and cathode to generate current. It has been reported that excitons in CdSe QDs are formed efficiently using lasers as excitation probe.[68] It is also reported that charge formation is easy upon exciton formation in CdSe QDs.[27] These qualities of quantum dots make it a better candidate for solar cell application. However, construction and fabrication of solar cell device is beyond the scope of this article. The focus here is to learn effect of dopant in electrical communication between QDs by the help of spectroscopic technique such as fluorescence intermittency.

Fluorescence intermittency or blinking is an analytical technique to record emission properties of individual particle and it is important to get information about electrical communication between QDs. It is important to achieve a very narrow laser beam to study individual particle which in this case is CdSe QDs. Single particle confocal microscopy is used to study fluorescence intermittency of undoped and indium doped QDs as it provides laser beam as low as 387 nm. The small spot size provided by the narrow laser beam is ideal to probe a small area. In this study confocal microscope acquires information about fluorescence intermittency of QDs. Fluorescence and fluorescence intermittency is two different phenomenon. Light emitted from fluorophore upon excitation by laser is known as fluorescence, whereas, fluorescence intermittency is a phenomenon where fluorescence of single nanocrystal is interrupted by dark states. The blinking behavior can be explained easily by the help of two level systems. In a two level electronic energy system, the electrons are promoted from ground state to the excited state upon excitation with laser of wavelength matching the energy gap between two states. This excited fluorophore can undergo either or all of the following steps; a) photon release through fluorescence, b) electron donation to its immediate environment, c) non radiative relaxation and d) energy transfer. The main focus of this research is to concentrate on first two steps of all four possible steps as described above and fluorescence intermittency is a powerful

technique for that reason. Reasons behind states in fluorescence intermittency are due to the presence of surface traps, non-emissive states, weakly emissive sates and charged fluorophore. Auger assisted ionization model explains that only neutral fluorophore can emit and charged species cannot emit resulting in dark state.[28] A charged species can only get neutralized if it receives counter charge from its surrounding. Thus, blinking which is combination of dark and bright states may reveal important information about electrical communication between QDs as in this case QDs are present in the environment.[69]

In this study, fluorescence intermittency is used to study single undoped and indium doped quantum dots in polymer composite. Polymer composite structure is preferred to hold QDs in its place securely so that location of every QD would not change over time and during the experiment. PMMA is used as a polymer here as it is non-conducting in nature and does not participate in any electrical communication with QDs. Indium dopant creates an extra level below the conduction band of quantum dots as discussed in chapter 3 and the extra electron makes the entire scenario interesting for intermittency experiment.

5.2 Experimental Section

5.2.1 Synthesis of CdSe Quantum Dots

Synthesis of undoped and doped CdSe quantum dots are done according to the method described in chapter 2 and section 3.2.

5.2.2 CdSe QDs-PMMA film preperation

PMMA (MW=120,000 g/mol) is obtained from Sigma-Aldrich and is used as received. A solution of CdSe QDs in toluene is added to the chloroform solution of PMMA (0.05 g /2 ml) and mixed well. A single drop of this solution is spin coated on a glass cover slip (FisherFinest) at 1500 rpm to result in the CdSe QDs/PMMA film.

5.2.3 Confocal microscope

Single point time transients and luminescence spectra were acquired on a sample scanning confocal microscope that has been described previously in Chapter 2.[70] Briefly, this

system is built upon an inverted epi-illumination microscope (Nikon TE-300). The composite films are placed on top of a closed-loop piezoelectric x,y-scanning stage (Sifam Instruments) attached to this microscope. A diode laser (Spectra-Physics, Cyan Scientific, 488 nm) is used as the excitation source. The laser light is directed into the epi-illumination port of the microscope and reflected from a dichroic beam splitter (Chroma, 505 DCLP) into the back aperture of an oil immersion objective (Nikon Plan Fluor, 1.3 numerical aperture, 100× magnification). The fluorescence is collected with the same objective lens and isolated by passing back through the dichroic beam splitter and subsequently through a holographic notch filter and a 580 nm band pass filter with 40 nm pass band. The fluorescence is then imaged onto a single photon counting avalanche photo diode (~175 μm diameter light sensitive element) for detection purposes. Fluorescence images are acquired by faster scanning the sample above the focused laser spot. The fluorescence signal was integrated for 20 ms per pixel in 200 × 200 pixel images of 20 × 20 μm^2 sample regions. Single point fluorescence time transients are collected by recording the spectrally integrated fluorescence in time from selected points in the sample. Fluorescence spectra are acquired by directing sample luminescence into an imaging spectrograph (Acton Research, 0.3 m) and onto a back-thinned, liquid N_2-cooled CCD detector (Princeton Instruments).

5.3 Results and Discussions

Concocal microscope records an image (200 × 200 pixel) and nanoparticles appear as a bright spot on those images (Figure 5.1).

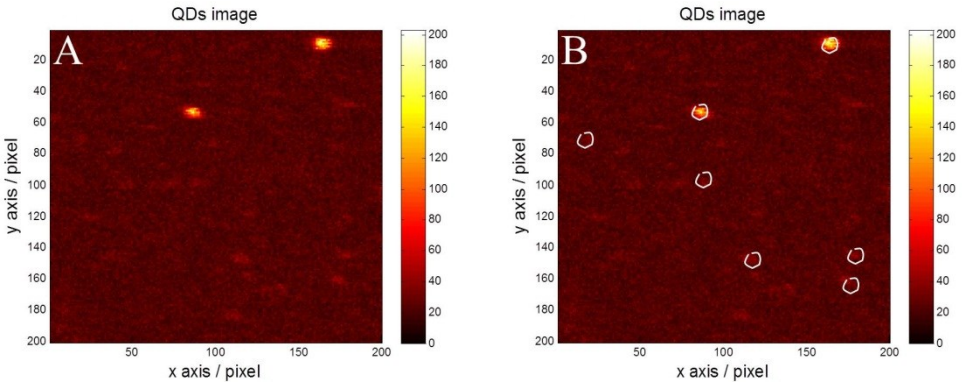

Figure 5.1 Confocal microscope image of CdSe QDs (A and B). Few bright spots are encircled.

A MATLAB code is written to extract confocal images information from binary format to digital format and the code is shown in Appendix A.3. QDs are seen to be appear as a bright spot in the confocal image (Figure 5.1 A) and some of the bright spots are encircled (Figure 5.1 B) for confirmation.

Confocal microscope can record time trace of fluorophore apart from recording image. The detector (APD) can be parked on a bright spot under continuous illumination and fluorescence can be recorded over long time period. This time trace shows blinking behavior of a single particle under continuous illumination and it is shown in Figure 5.2. Blinking behavior of undoped and indium doped CdSe quantum dots are shown in part A and D of the Figure 5.2 respectively.

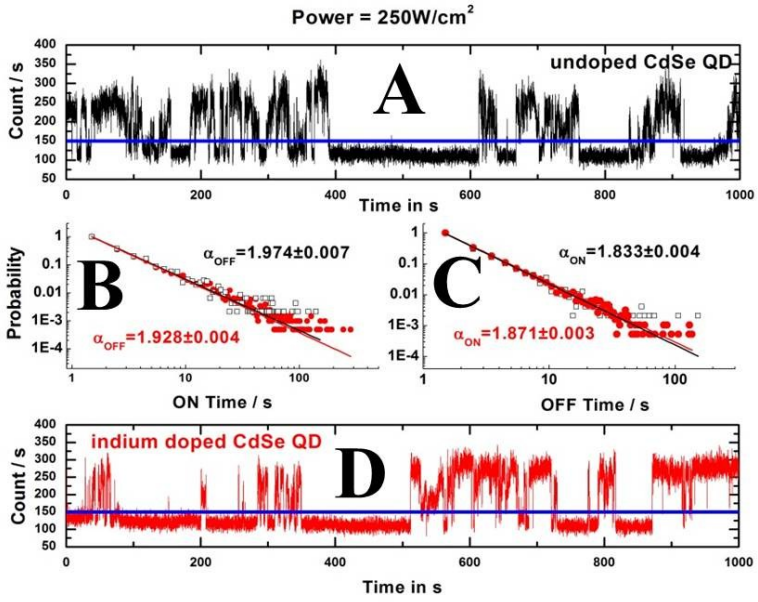

Figure 5.2 Time trace of undoped CdSe quantum dots (A) and indium doped CdSe quantum dots (D). Power law behavior of on time (B) and off time (C) for both undoped and indium doped QDs respectively.

Time transient data is recorded for 1000 seconds with a time resolution of 20 ms. Emitted fluorescence is represented in counts and they are plotted against time as shown in Figure 5.2 A and D. A blue line is shown on both time trace of undoped and indium doped QDs and it is known as threshold line. The definition of threshold line is it is the square root of background

emission. It is important to draw threshold line because it is believed that any emission above and below the threshold line is defined as “on state” and “off state” respectively.

The most important data extracted from time transient measurement is the probabilities of the QDs to stay in “on state” or “off state” continuously. A calculation is carried out to determine the probability of QDs to stay in “on state” or “off state” and it is shown in Figure 5.2 B and C respectively. Power law behavior of undoped and indium doped quantum dots are expressed by black hollow squares and filled red circles respectively. Y and X axis of the two figures (5.2 B and C) are expressed in logarithmic form and in seconds, respectively. The probability distribution ($P(\tau)$) can be fitted by power law equation which states that power law is proportional to the exponent of “on” or “off” time ($\alpha_{on/off}$) and it is expressed in eq (1). The proportionality constant is expressed by A.

$$P(\tau) = A\tau^{\alpha_{on/off}} \qquad (1)$$

The average trend of power law distribution is expressed by black and red line for undoped and indium doped QDs respectively (Figure 5.2 B and C). The values of exponent for undoped and indium doped QDs are expressed in Table 5.1.

Sample	$\boldsymbol{\alpha_{on}}$	$\boldsymbol{\alpha_{off}}$
Undoped CdSe QDs	1.833±0.004	1.974±0.007
Indium doped CdSe QDs	1.871±0.003	1.928±0.004

Table 5.1 Time exponent on undoped and indium doped CdSe QDs.

It is observed that the trend of power laws of undoped and indium doped QDs do not show significant difference from each other (Figure 5.2 B and C). A possible reason for this could be erroneous sampling of spots to record data. Since doping is completely random and concentration of dopants is low (only 5%), it is highly possible that many QDs are not containing any dopants. If by any chance, the sampling region is full of such undoped QDs, then no difference of blinking could be observed. In other words recorded data will resemble that of undoped CdSe QDs. A possible solution to this problem would be to introduce a marker to different particle. If it is possible to design an experimental technique where doped quantum dots can be marked by SEM and those marked points can be observed under optical microscope, new set of data would reveal the behavior of undoped and doped quantum dots.

5.4 Conclusions

Fluorescence intermittency of undoped and indium doped CdSe quantum dots are recorded. The data reveals completely random nature of the “on” and “off” time of both systems. Power law behavior of both undoped and indium doped QDs are found to be very similar to each other. A possible explanation is that indium dopant does not change the blinking dynamics at room temperature due to the lack of ionization of defects site.

Chapter 6 - Fluorescence Intermittency of CdSe Nanorods with Changing Polarization of Incident Light

6.1 Introduction

CdSe nanocrystals have drawn significant attention in recent past due to their wide range of optical and electrical properties. CdSe quantum dots (QDs) have been studied as a model system and applied to different fields such as lasers,[3] LEDs,[1,2] and bio-labeling[4]. The emission from QDs is found to be unpolarized,[37] which is believed to be caused by their spherical structure. Unlike to the QDs, CdSe nanorods (NRs) emit polarized light.[71] NRs can be considered as an elongated QD in crystallographic *z*-direction. The elongated axis in NRs gives rise to different crystal structure as compared to that of QDs. The crystal structure of CdSe NRs is known to be Wurtzite structure as opposed to Zinc-blend structure of CdSe QDs.

It is interesting to study anisotropic emission of CdSe NRs in the presence of polarized light and the effect of P3HT on it. Polarized light emission from single CdSe NRs is important as it provides information about the orientation of NRs and the relaxation process that lead to depolarization of the exciton. A single nanorod with a fixed dipole moment emits linearly polarized light upon excitation with plane polarized light. Probability of transition is the square of absolute value of the dot product between the dipole moment and polarized light vectors. Transition probability indicates cosine dependence of the angle between the two vectors. Thus the direction of atomic dipole can be determined from the polarized emission if the direction of polarized excitation is known.

Any real system is always a collection of atoms. The emission from a material depends on the dipole moment orientation of the ensemble of atoms which is also known as molecular dipole moment. Probability of transition is the absolute value of dot product between molecular dipole moment and polarized light vectors. It is experimentally determined that CdSe NRs emit[37] and have a large dipole moment along the crystallographic *z*-direction.[30] Intensity of polarized emission depends on the degree of alignment of individual dipoles. Fluorescence anisotropy study requires recording of the polarized emissions. The emissions are recorded both in parallel and perpendicular direction to that of incident polarization of light. Thus any observed anisotropy indicates the preference of emission in a certain direction. This research is expected to provide a clear picture of direction of polarized emission and their dependence with the

environment. With the acquired knowledge of polarization, this research can be directly extended to align the NRs in polymer matrix by some external force such as electricity. A completely polarized light emission can be achieved once the NRs are perfectly parallel to each other.

6.2 Synthesis of CdSe Nanorods

CdSe NRs are synthesized under oxygen-free conditions.[72] The reaction mixture, comprised of 50 mg of CdO, 4.1 g of trioctylphosphine oxide (TOPO) and 305 mg of TDPA (Tetra decyl phosphonic acid), is prepared in a three-neck flask with septa, a thermometer and a refluxing column. The refluxing column is attached to a Schlenk line. The solution is first heated to 120 ^{o}C under Argon flow and subsequently placed under vacuum for 1 hr. A selenium-trioctylphosphine (SeTOP) solution is prepared separately in a nitrogen-filled glovebox. A mixture of 4 ml of trioctylphosphine and 42 mg of Se powder are placed into a vial that was then capped with a septum. The solution is stirred in the glovebox with a magnetic stirrer. The Se is dissolved in TOP in ~ 0.5 hr. The solution temperature is then raised to 280 °C, after which it became golden yellow. At this point, the cadmium solution is returned to atmospheric pressure and the temperature is increased to 270 °C. The SeTOP solution is then injected and the solution temperature is decreased to 230 °C. Growth of the NRs was performed at 260 °C. The entire growth process is monitored by UV-visible and photoluminescence spectroscopy. NR growth is terminated after ~ 5 min. Methanol is added to the reaction mixture once the solution had cooled to room temperature. The mixture is then centrifuged and the supernatant was discarded. This process is repeated five times. A dark red solution is obtained when the NRs were dissolved in spectroscopic grade toluene. The crude reaction mixture is washed thoroughly with methanol to remove the phosphine ligands. The binding strength of the ligands is sufficiently low that they are easily removed by washing with organic solvents.[73]

6.3 Experimental Section

Film preparation:

Two different types of films are prepared. The first is a NR and PMMA composite, while the second is a NR, PMMA and P3HT composite. PMMA (MW=120,000 g/mol) is obtained from Sigma-Aldrich and is used as received. P3HT (regioregular form, MW=20,000-70,000) is obtained from American Dye Source and is also used as received. Two separate PMMA solutions are prepared by dissolving 0.05 g of PMMA in 2 mL of chloroform. To the first

PMMA solution, 2 mL of NRs in toluene is added and mixed well. A solution of P3HT is prepared by dissolving 0.003 g of P3HT in 4 mL of chloroform. A 0.04 mL aliquot of this P3HT solution is then added to the second PMMA solution, yielding a 6% (by weight) mixture of P3HT in PMMA. A 2 mL aliquot of NRs in toluene is then added to the PMMA/P3HT mixture and mixed well. CdSe/PMMA films and CdSe/P3HT films (the latter was comprised of NRs dispersed in a PMMA film also incorporating dilute P3HT) are obtained by spin casting (1500 rpm, 1 min) a single drop of the appropriate solution onto a glass cover slip (FisherFinest). Film thickness is determined on a spectroscopic ellipsometer (J. A. Woolam, α-SETM). Average thicknesses of the CdSe/PMMA and CdSe/P3HT composite films are found to be 49 ±23 nm and 53 ±32 nm, respectively. The CdSe NR concentrations of the casting polymer solutions are indicated in the Figure caption of each presented experimental data.

Confocal microscope:

Single point time transients and luminescence spectra are acquired on a sample scanning confocal microscope that has been described previously.[70] Briefly, this system is built upon an inverted epi-illumination microscope (Nikon TE-300). The composite films are placed on top of a closed-loop piezoelectric x,y-scanning stage (Sifam Instruments) attached to this microscope. A diode laser (Spectra-Physics, Cyan Scientific, 488 nm) is used as the excitation source. The laser light is directed into the epi-illumination port of the microscope and reflected from a dichroic beam splitter (Chroma, 505 DCLP) into the back aperture of an oil immersion objective (Nikon Plan Fluor, 1.3 numerical aperture, 100× magnification). The fluorescence is collected with the same objective and isolated by passing back through the dichroic beam splitter and subsequently through a holographic notch filter and a 580 nm band pass filter having a 40 nm pass band. Trap emission is acquired by reflecting it from a 700 nm dichroic shortpass (Chroma E700sp) and through a 700 nm longpass filter. The fluorescence is then imaged onto a single photon counting avalanche photo diode (~175 μm diameter light sensitive element) for detection purposes. Fluorescence images are acquired by faster scanning the sample above the focused laser spot. The fluorescence signal is integrated for 20 ms per pixel in 200 × 200 pixel images of 20 × 20 μm^2 sample regions. Single point fluorescence time transients are collected by recording the spectrally integrated fluorescence in time from selected points in the sample. Fluorescence spectra are acquired by directing sample luminescence into an imaging spectrograph (Acton

Research, 0.3 m) and onto a back-thinned, liquid N_2-cooled CCD detector (Princeton Instruments).

6.4 Results and Discussions

6.4.1 Polarized emission of P3HT composite film

NRs films are subjected to confocal microscopy and polarization of incident light is changed using a pockel cell. The image (consist of 100 X 100 pixels) is formed by recording emission while scanning incident light pixel by pixel of a certain area of microscope slide. Polarization of incident light is changed from 0^o to 180^o in six steps (each step of 30^o) with respect to initial incident polarization of light. Emission is recorded for every pixel at every polarization before the light scans next pixel. Emitted fluorescence is then divided by a beam splitter that resolves parallel and perpendicular emissions which are then recorded by two APD detectors. One full scan produces total twelve emission images with six parallel and six perpendicular images. A MATLAB code (see Appendix A.2) is written that calculates total absolute emission and angle of emission with respect to incident light polarization at each pixel. Blank P3HT is recorded for comparison purpose in Figure 6.1.

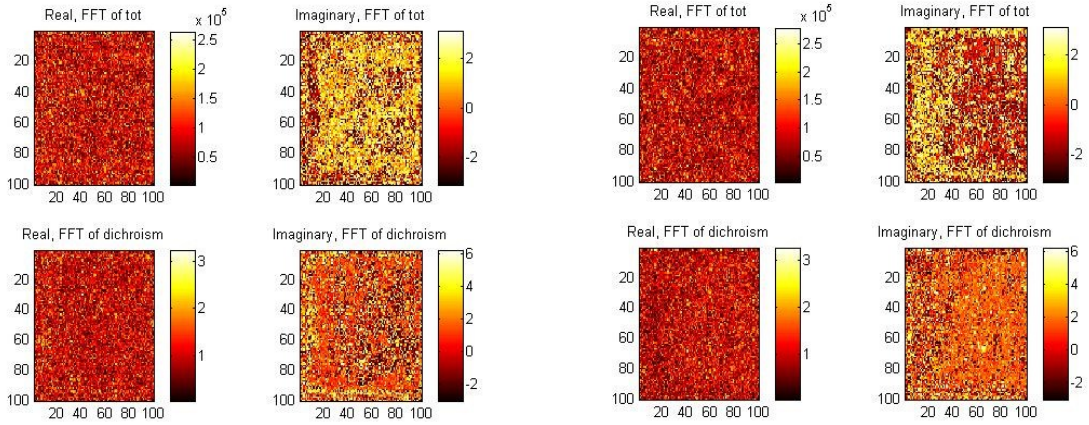

Figure 6.1 P3HT band edge (left) and trap (right) emission.

In these experiments, the excitation polarization is rotated resulting several band edge and trap emission images as a function of input polarization. These images are generated by taking the

Fast Fourier transform (FFT) to obtain the amplitude and phase of the signal at the frequency corresponding to the input polarization modulation. The same process is applied to both the total emission and dichroism of the input images and the resulting data are plotted in these figures. There are two FFT images for total emission and dichroism of P3HT film respectively. Real part (top-left and bottom-left of four images) and imaginary part of the images (top-left and bottom-left of four images) are absolute value of the emission and angle between incident and emitted light respectively. Band edge and trap state emissions are represented by "left" and "right" panel of Figure 6.1 respectively. Real part of both band edge and trap state does not show significant information but imaginary part shows structural behavior. It is important to collect more data here to draw a plausible conclusion.

6.4.2 Polarized emission of PMMA composite film

PMMA composite films are placed on confocal microscope stage and subjected for polarized emission study as described in previous section. Polarized emission of PMMA composite film is shown in Figure 6.2.

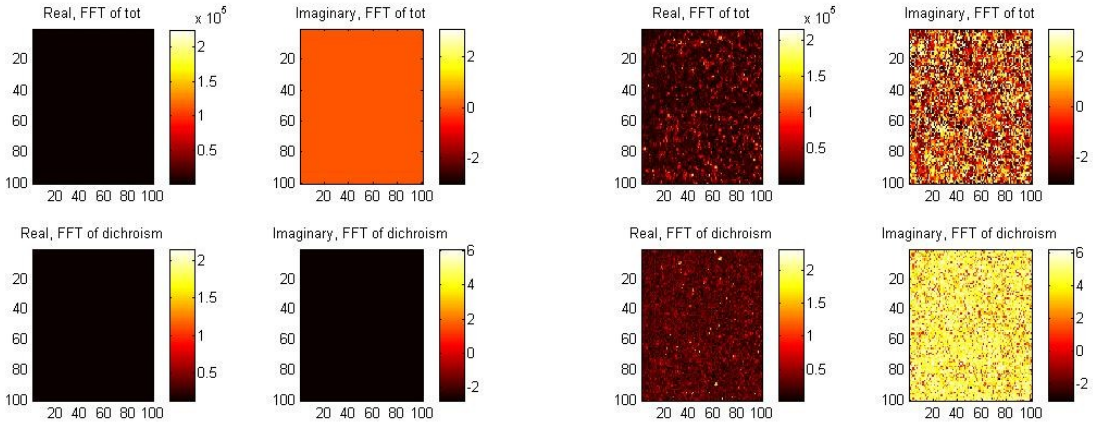

Figure 6.2 PMMA band edge (left) and trap (right) emission.

Real part (top-left and bottom-left of four images) and imaginary part of the images (top-left and bottom-left of four images) are absolute value of the emission and angle between incident and emitted light of PMMA film respectively. Real and imaginary part of total FFT shows emissions from PMMA and structural behavior of angular dependence of emission respectively. Band edge and trap state show significantly different emission. There is no band edge state emission

observed but little trap state emission is observed. The trap state of PMMA composite does provide some information and short range structure is observed. It is important to collect more data here to draw a plausible conclusion.

6.4.3 Polarized emission of NR-PMMA composite film

In the next step NRs-polymer composite films are placed on confocal microscope stage and subjected for polarized emission study as described in previous section. Polarized emission of NRs-PMMA composite film is shown in Figure 6.3.

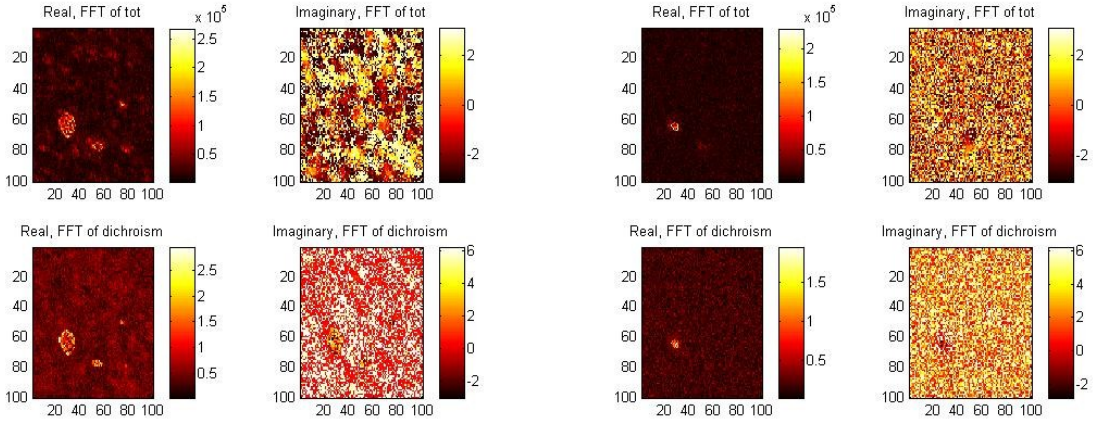

Figure 6.3 NR-PMMA band edge (left) and trap (right) emission.

Real part (top-left and bottom-left of four images) and imaginary part of the images (top-left and bottom-left of four images) are absolute value of the emission and angle between incident and emitted light of NRs-PMMA film respectively. Real and imaginary part of total FFT shows significant emissions from NRs and structural behavior of angular dependence of emission respectively. The trap state of NRs-PMMA composite does provide some information and that could be because there is no significant trap state emission for these particles. It is important to collect more data here to draw a plausible conclusion.

6.4.4 Polarized emission of NRs-P3HT composite film

Polarized emission of band edge and trap state emission of NRs-P3HT composite film is shown in Figure 6.3. Real part (top-left and bottom-left of four images) and imaginary part of the images (top-left and bottom-left of four images) are absolute value of the emission and angle

between incident and emitted light of NRs-P3HT film respectively. Real and imaginary part of total FFT shows significant emissions from NRs and structural behavior of angular dependence of emission respectively. The trap state of NRs-P3HT composite does not provide significant information and that could be because there is no significant trap state emission for these particles. It is important to collect more data here to draw a plausible conclusion.

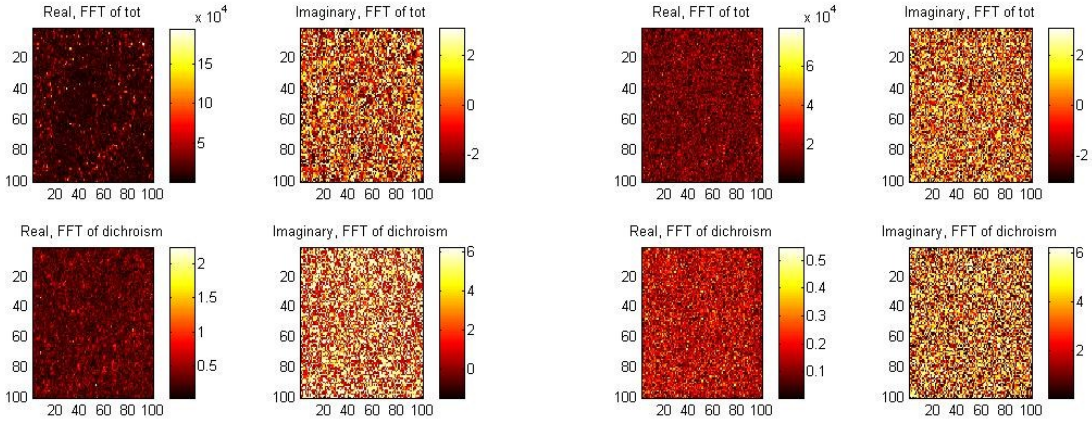

Figure 6.4 NR-P3HT band edge (left) and trap (right) emission.

6.5 Conclusions

Confocal microscope image of CdSe nanorods in PMMA and P3HT matrix is recorded. Polarization of the incident light is changed using a pockel cell from horizontal to vertical with respect to the table on which experiment is set up. It is important to collect more data here to draw a plausible conclusion.

There could be two possible reasons for not getting conclusive result. The confocal lens converges the incident light and that causes loss of polarization of the incident light on to the sample. This challenge can be overcome by using a wide field microscope instead of confocal microscope. The other reason of not getting conclusive result could be the random orientation of nanorods itself. Any kind of external measure is not employed to align the nanorods on microscope cover slip and may be due to that the results are not conclusive. This challenge of aligning nanorods can be overcome by using photolithography technique to align the nanorods.

Chapter 7 - Investigation of Charge Transfer Interaction of CdSe Nanorods P3HT/PMMA Blends by Optical Microscopy

7.1 Introduction

The development of robust technologies to produce efficient, inexpensive solar cells is a major thrust of current scientific research.[45,74] Hybrid organic polymer and inorganic quantum confined structures represent important platforms that will likely lead to improved energy conversion devices.[75] The high photostability of inorganic photosensitizers[76] offers a competitive edge over devices constructed from organic semiconductors alone, while the solution based processing of organic materials allows simpler preparation procedures than inorganic technologies. Hybrid organic/inorganic materials take advantage of both these attributes. Importantly, such hybrid materials also introduce new challenges, in this case, because of the new interface between the two media.

To date, some of the most efficient hybrid solar cells have been produced by combining CdSe quantum dots,[45] rods,[45,77] tetrapods[78,79] or superbranched structures[80] with poly(3-hexylthiophene) (P3HT) or poly(phenylene vinylene) (PPV). In these materials, the organic polymer serves as an electron donor and the quantum confined CdSe as an electron acceptor. Although CdSe is an unsustainable material,[81-84] it has been proven to be an efficient photosensitizer, an ideal model platform to better understand the fundamental aspects of charge separation and migration, and to improve efficiencies in hybrid solar cells.[77] For example, CdSe/PPV materials have been reported to yield external quantum efficiencies as high as 12%.[85] The highest power conversion efficiency achieved for CdSe nanorod(NR)/P3HT hybrid solar cells is reported to be 7% under a monochromatic illumination at 3 $mWcm^{-2}$.[77] The overall power conversion efficiency is governed by the superposition of the steps involved in power generation (light absorption, exciton generation, exciton diffusion, charge separation, charge migration) and the processes that lead to loss of excitons and charges (exciton and charge recombination).

A very important step in power generation is the separation of charges at the CdSe/polymer interface. The efficiency of interfacial charge separation is strongly dependent upon the exact nature of the contact between these materials. As a result, multiple approaches have been explored to tune these interactions and to better understand and enhance interfacial charge and energy transfer. For example, Skaff and coworkers have demonstrated methods for

directly grafting vinyl terminated PPV onto CdSe nanoparticles.[86] In their procedure, reactive bromobenzene-modified dioctylphosphine oxide ligands, to which PPV could be attached, were employed during nanoparticle synthesis.[86] Odoi, *et al.* have shown that CdSe quantum dots prepared with similar oligophenylene vinylene (OPV) ligands[87] yield improved CdSe emission stability that results from enhanced charge and energy transfer between the ligands and quantum dots. It was later concluded from single particle studies performed as a function of OPV ligand coverage that fluorescence intermittency (i.e., blinking) in these materials is suppressed specifically by charge transfer from the ligands to surface traps on the CdSe.[88] Xu, *et al.*[89] and Zhang, *et. al*.[90] have prepared related CdSe/P3HT composites by grafting vinyl-terminated P3HT onto bromobenzene-functionalized CdSe nanoparticles. Both these studies show clear evidence for enhanced electronic communication between the nanoparticles and organic polymers, along with reduced nanoparticle aggregation. Although much has been learned from these studies, efficient, inexpensive solar cells will most likely be obtained from simple blends of polymers and nanoparticles, because these methods avoid relatively lengthy overcoating procedures.[45,77,80]

Optical microscopy and spectroscopy performed on single particle,[91] few particle[92] and aggregate level have been used previously to investigate interactions between quantum dots and their ligands[88] as well as charge generation and trapping in quantum dots[93-95] and composite quantum dot/semiconducting polymer materials.[96,97] Inorganic nanostructures such as CdSe nanorods and dots are well suited for interrogation by these techniques because of their high photostabilities and large absorption cross sections.[98] Luminescence intermittency (blinking) in nanoparticles is usually described by a power law over many orders of magnitude in time.[93,94] The blinking dynamics observed at the single particle or small aggregate level[99,100] is frequently controlled by charge generation and trapping processes at the surface of individual particles. Based on current literature models,[27,101] it is believed the dark state of a particle is produced when an electron leaves the particle and the particle becomes charged. The positive charge suppresses further emission by Auger recombination with subsequently photogenerated electron-hole pairs. The bright state returns when the positive charge is neutralized. The blinking dynamics can thus reflect the dynamics of charge transfer from an attached ligand, a neighboring quantum dot or from the surrounding matrix. In organic/inorganic hybrid systems, such studies afford important information on charge transfer between the nanoparticles and surrounding polymer.

In this study, we employ optical luminescence microscopy and spectroscopy to explore the importance of charge transfer interactions at the interface between CdSe NR and P3HT in hybrid blends. Unlike previous studies of CdSe/P3HT hybrids,[89,99,102,103] these blends incorporate dilute P3HT dispersed in a poly(methylmethacrylate) (PMMA) matrix. The use of dilute P3HT allows for detection of NR luminescence in the presence of P3HT. P3HT emission overwhelms nanoparticle emission in "pure" P3HT composites. The dilute P3HT/PMMA matrix also helps to avoid P3HT aggregation, which can alter electronic interactions with CdSe due to an aggregation-induced bathochromic shift in the lowest energy electronic transition of P3HT.[89] Furthermore, the NRs employed in these studies contain no overcoat other than the solvent ligands employed during synthesis. The results obtained from CdSe/P3HT hybrids are compared to those from CdSe/PMMA dispersions (i.e., in the absence of dilute P3HT). Wide field luminescence imaging, single-point fluorescence time transients and single point optical spectroscopy experiments performed on these two types of samples show that interfacial charge transfer interactions play an important role in governing NR luminescence in dilute CdSe/P3HT films. NR bandedge luminescence is shown to be enhanced in the presence of P3HT, likely by static charge transfer interactions. P3HT is also shown to alter the power law luminescence blinking dynamics observed from the NRs, while the photoactivation of NR luminescence in P3HT provides strong evidence of the role played by dynamic charge transfer processes.

7.2 Experimental Section

Synthesis of CdSe Nanorods:

CdSe NRs were synthesized under oxygen-free conditions.[72] The reaction mixture, comprised of 50 mg of CdO, 4.1 g of trioctylphosphine oxide (TOPO) and 305 mg of TDPA (Tetra decyl phosphonic acid), was prepared in a three-neck flask with septa, a thermometer and a refluxing column. The refluxing column was attached to a Schlenk line. The solution was first heated to 120 ^{o}C under Argon flow and subsequently placed under vacuum for 1 hr. A selenium-trioctylphosphine (SeTOP) solution was prepared separately in a nitrogen-filled glovebox. A mixture of 4 ml of trioctylphosphine and 42 mg of Se powder were placed into a vial that was then capped with a septum. The solution was stirred in the glovebox with a magnetic stirrer. The Se dissolved in TOP in ~ 0.5 hr. The solution temperature was then raised to 280 °C, after which

it became golden yellow. At this point, the cadmium solution was returned to atmospheric pressure and the temperature was increased to 270 °C. The SeTOP solution was then injected and the solution temperature decreased to 230 °C. Growth of the NRs was performed at 260 °C. The entire growth process was monitored by UV-visible and photoluminescence spectroscopy. NR growth was terminated after ~ 5 min. Methanol was added to the reaction mixture once the solution had cooled to room temperature. The mixture was then centrifuged and the supernatant was discarded. This process was repeated five times. A dark red solution was obtained when the NRs were dissolved in spectroscopic grade toluene. The crude reaction mixture was washed thoroughly with methanol to remove the phosphine ligands. The binding strength of the ligands is sufficiently low that they are easily removed by washing with organic solvents.[73]

Concentration determination:

The concentration of the NRs was measured using Beer's law. The absorbance of the NR solution, and the extinction coefficient of the NRs, as reported in the literature, were employed in the calculation.[104]

Film preparation:

Two different types of films were prepared. The first was a NR and PMMA composite, while the second was a NR, PMMA and P3HT composite. PMMA (MW=120,000 g/mol) was obtained from Sigma-Aldrich and was used as received. P3HT (regioregular form, MW=20,000-70,000) was obtained from American Dye Source and was also used as received. Two separate PMMA solutions were prepared by dissolving 0.05 g of PMMA in 2 mL of chloroform. To the first PMMA solution, 2 mL of NRs in toluene was added and mixed well. A solution of P3HT was prepared by dissolving 0.003 g of P3HT in 4 mL of chloroform. A 0.04 mL aliquot of this P3HT solution was then added to the second PMMA solution, yielding a 6% (by wgt) mixture of P3HT in PMMA. A 2 mL aliquot of NRs in toluene was then added to the PMMA/P3HT mixture and mixed well. CdSe/PMMA films and CdSe/P3HT films (the later was comprised of NRs dispersed in a PMMA film also incorporating dilute P3HT) were obtained by spin casting (1500 rpm, 1 min) a single drop of the appropriate solution onto a glass cover slip (FisherFinest). Film thickness was determined on a spectroscopic ellipsometer (J. A. Woolam, α-SETM). Average thicknesses of the CdSe/PMMA and CdSe/P3HT composite films were found to be 49 ±23 nm

and 53 ±32 nm, respectively. The CdSe NR concentrations of the casting polymer solutions are indicated in the Figure caption of each presented experimental data.

Confocal microscope:

Single point time transients and luminescence spectra were acquired on a sample scanning confocal microscope that has been described previously.[70] Briefly, this system is built upon an inverted epi-illumination microscope (Nikon TE-300). The composite films were placed on top of a closed-loop piezoelectric x,y-scanning stage (Sifam Instruments) attached to this microscope. A diode laser (Spectra-Physics, Cyan Scientific, 488 nm) was used as the excitation source. The laser light was directed into the epi-illumination port of the microscope and reflected from a dichroic beam splitter (Chroma, 505 DCLP) into the back aperture of an oil immersion objective (Nikon Plan Fluor, 1.3 numerical aperture, 100× magnification). The fluorescence was collected with the same objective and isolated by passing back through the dichroic beam splitter and subsequently through a holographic notch filter and a 580 nm band pass filter having a 40 nm pass band. Trap emission was acquired by reflecting it from a 700 nm dichroic shortpass (Chroma E700sp) and through a 700 nm longpass filter. The fluorescence was then imaged onto a single photon counting avalanche photo diode (~175 μm diameter light sensitive element) for detection purposes. Fluorescence images were acquired by raster scanning the sample above the focused laser spot. The fluorescence signal was integrated for 20 ms per pixel in 200 × 200 pixel images of 20 × 20 μm^2 sample regions. Single point fluorescence time transients were collected by recording the spectrally integrated fluorescence in time from selected points in the sample. Fluorescence spectra were acquired by directing sample luminescence into an imaging spectrograph (Acton Research, 0.3 m) and onto a back-thinned, liquid N_2-cooled CCD detector (Princeton Instruments).

Wide-field microscope:

Fluorescence images of the samples were also acquired by wide-field imaging.[105] The system employed is built upon an inverted epi-illumination microscope (Nikon Eclipse TiE). Excitation light in these experiments was either from a Nd:YVO_4 laser (Coherent, Verdi, 532 nm) or a diode laser (488 nm). The incident light was first focused into a spinning optical diffuser and subsequently collected and passed through a polarization scrambler before being directed into the

epi-illumination port of the microscope. The light was reflected from a dichroic beam splitter (Chroma Q555LP or Chroma, Q505LP), for 532 nm and 488 nm excitation, respectively) and focused into the back aperture of an oil immersion objective (Nikon Apo TIRF 100X, 1.49 N.A.). Fluorescence from the sample was collected and separated from the incident laser light by passage back through the beam splitter and a 580 nm band pass filter having a 40 nm pass band. A back-illuminated EM-CCD camera (Andor iXon DU-897) was used as the detector. Wide-field movies were commonly recorded as 100 frame videos with 1 sec frame times.

7.3 Results and Discussion

The CdSe NRs used in these experiments exhibit a very narrow size distribution, as shown in Figure 7.1.

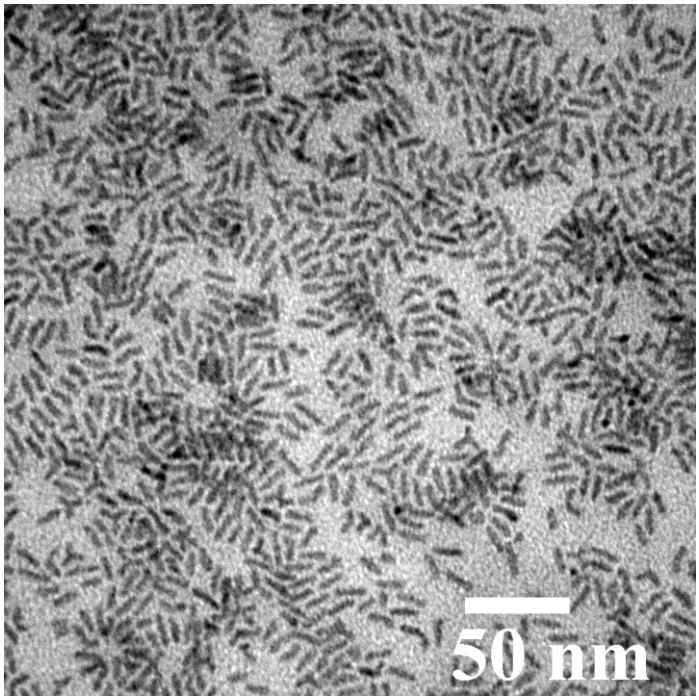

Figure 7.1 TEM image of synthesized CdSe NRs.

The rods are 20 nm in length and 4 nm in diameter. They exhibit a sharp absorption feature centered at 574 nm that is reflective of the relatively narrow size distribution (Figure 7.2). The emission spectrum of the CdSe NRs is dominated by two spectroscopic features, as shown in Figure 7.3. One constitutes the bandedge emission of the NRs and is centered at 585 nm. A

broader feature centered at ~800 nm is also observed. Long wavelength emission in this range has previously been attributed to CdSe trap state emission,[106,107] and is therefore also assigned to trap emission from bare CdSe NRs in the present materials. P3HT absorbs at 450 nm and emits at 590 nm in toluene solution (see Figure 7.3) and at similar wavelengths as a dilute dispersion in thin PMMA films (Figure 7.4).

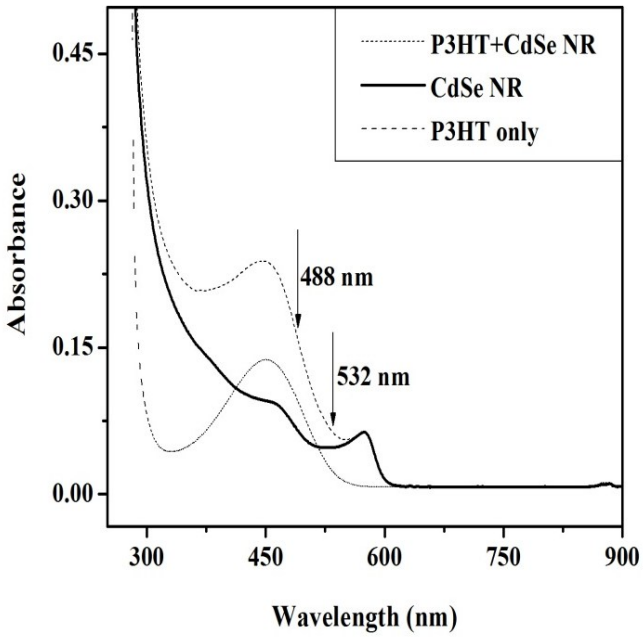

Figure 7.2 Absorption spectrum the CdSe nanorods. Absorption of P3HT is also shown.

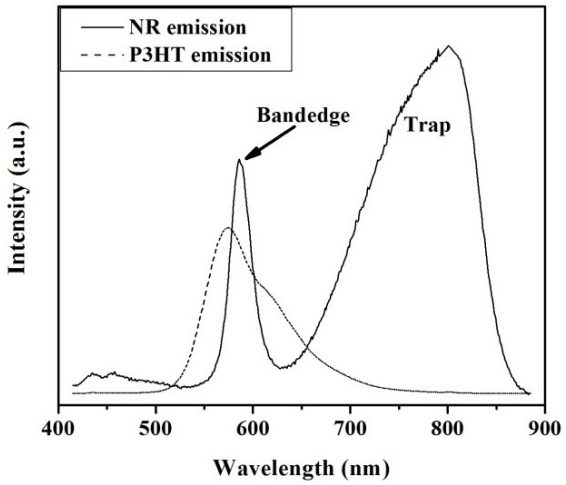

Figure 7.3 Photoluminescence spectrum of the CdSe nanorods. The photoluminescence spectrum was acquired in toluene.

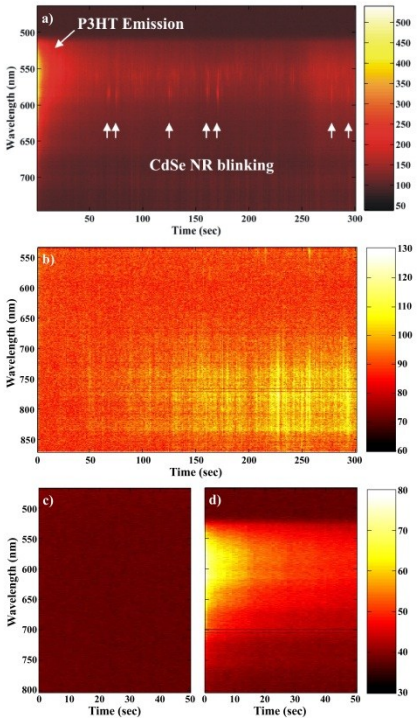

Figure 7.4 (a) and (b) bandage and trap emission blinking from single points in CdSe/P3HT and CdSe/PMMA films, respectively. The initially bright P3HT emission in (a) fades away rapidly while the CdSe NRs continue to exhibit bandedge emission. Trap emission is shown to grow in over time in (b). The CdSe NR concentration in the casting solutions was 0.5 μmol/L and 0.65 μmol/L, respectively. (c) and (d) PMMA and P3HT/PMMA film emission in the absence of NRs.

Overlap observed in the absorption and bandedge emission spectra of the polymer and NRs has been shown previously to lead to appreciable energy transfer between the two materials.[90]

Wide field fluorescence images obtained from the CdSe/PMMA and CdSe/P3HT samples provide initial evidence of electronic interactions between the NRs and dilute P3HT in the PMMA film (such samples are designated as CdSe/P3HT materials throughout this report). Representative frames of wide field videos recorded from CdSe/PMMA and CdSe/P3HT films are shown in Figure 7.5 (top row). As shown, the CdSe/PMMA sample exhibits relatively little emission, while CdSe/P3HT emission is significantly (~ 10 times) more intense. The color scale in Figure 7.5d depicts count rates 10 times larger than in Figures 7.5a-c (see Figure 7.5 caption for absolute signal levels). Films of PMMA alone exhibit only extremely weak background emission. Several characteristics of the emission observed in these videos indicate that the NRs play a direct role in producing the observed emission.

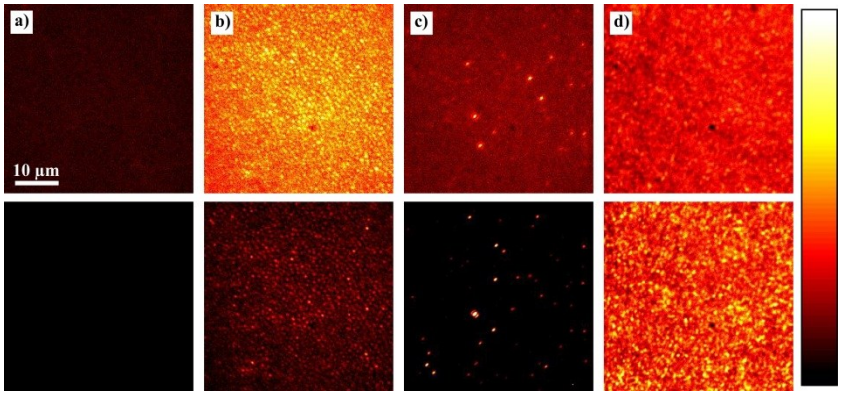

Figure 7.5 Representative frames (top) and standard deviation images (bottom) from wide field luminescence videos of (a) PMMA and (b) P3HT/PMMA films, and (c) CdSe/PMMA and (d) CdSe/P3HT composite films. Fluorescence was excited at 532 nm. The color scale (right) in these images depict signal ranges of (a-c, top) 450-1600 counts, (d, top) 4,500-16,000 counts, (a-c, bottom) 50-225 counts, (d, bottom) 200-900 counts. The CdSe NR concentrations in the casting solutions were 3.05 µmol/L and 4.22 µmol/L for CdSe/P3HT and CdSe/PMMA samples, respectively.

First, the bright spots observed in both the CdSe/PMMA and CdSe/P3HT samples exhibit clear evidence of fluorescence intermittency (blinking). The level of blinking in each is also shown in Figure 7.5 (bottom row), by "images" depicting the standard deviation of the luminescence signal in time. These images were obtained by calculating the standard deviation across all frames for each pixel in the images. While both the CdSe/PMMA and CdSe/P3HT images incorporate numerous points exhibiting high standard deviations (i.e., significant blinking), neither PMMA films nor PMMA/P3HT films prepared in the absence of NRs exhibit such behavior (see Figures 7.5 a,b). Second, although PMMA/P3HT films exhibit appreciable fluorescence, the emission intensity becomes stronger (~ 10 times stronger) in the presence of the NRs. Furthermore, PMMA/P3HT film emission is observed to rapidly fade through photobleaching (Figure 7.4). The CdSe/P3HT images show similar behavior, exhibiting a diffuse background that fades away over relatively short time scales.

The importance of interactions between the dilute P3HT and the NRs is clearly reflected by the observation that the CdSe/P3HT samples produce significantly higher emission than any other sample (see Figure 7.5). Again, the color scale in Figure 7.5d (top) depicts ten-fold larger signals than in Figures 7.5a-c. Furthermore, the videos obtained from the CdSe/P3HT samples show a significantly larger number of bright spots compared to CdSe/PMMA samples. These observations are consistent with strong enhancement of NR emission and an increase in the

number of active emitters in the presence of dilute P3HT. Enhancement of NR emission could occur by energy transfer from P3HT to the NRs or by charge transfer from P3HT. The former is expected to occur based on overlap of the P3HT emission spectrum with the NR absorption spectrum (see Figure 7.6).

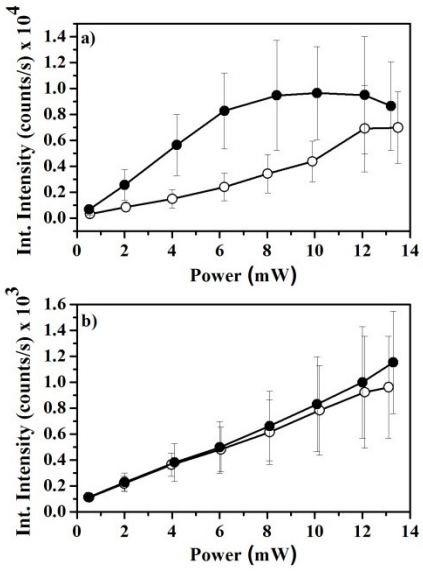

Figure 7.6 Power dependence of luminescence from (a) CdSe/P3HT and (b) CdSe/PMMA films excited at 532 nm. Data obtained from wide field images. The CdSe NR concentrations in the casting solutions were 3.05 μmol/L and 4.22 μmol/L for CdSe/P3HT and CdSe/PMMA samples, respectively.

However, the enhancement of NR emission does not change significantly when excited at 532 vs. 488 nm. The relative excitation efficiencies for the NRs and P3HT change by a factor of 10 when the excitation wavelength is changed to 532 nm, where P3HT is less efficiently excited. This observation suggests that NR emission enhancement originates from static charge transfer interactions and not energy transfer.

It is apparent that dynamic charge transfer processes also contribute to the enhancement of NR emission. Photoactivation of NR bandedge emission is clearly observed in the presence of dilute P3HT, but is much less significant in PMMA alone. Photoactivation of NR bandedge emission was explored through studies of the power dependence of NR luminescence in wide-field images of the samples. Figure 7.6 depicts these data. The data points in these plots were obtained by calculating the background-subtracted average signal obtained from all bright spots observed in the associated images. The open circles depict the signal obtained as the incident

power was slowly increased from zero, while the filled circles show the signal obtained as the incident power was subsequently reduced from high power conditions. The hysteresis observed in the data from the CdSe/P3HT sample (Figure 7.6a) provides clear evidence of photoactivation. The laser fluence is relatively low in these experiments (less than ~ 50 W/cm^2) and no saturation of the CdSe NRs is expected. In contrast, the CdSe/PMMA sample (Figure 7.6b) exhibits little such behavior. It should be noted that these experiments were performed over a period of ~ 15 min, indicating that photoactivation in the case of the CdSe/P3HT sample is very long-lived. Possible contributions from thermal effects were excluded by incorporation of dark periods (2 s) between measurements. The photoactivation of NR emission is therefore directly attributable to the presence of the P3HT and may be explained by photoactivated electron transfer from the dilute P3HT molecules to the CdSe NRs.

The NR blinking dynamics in P3HT and PMMA also provide evidence of interfacial charge transfer interactions. Bandedge fluorescence intermittency for CdSe NRs in PMMA and dilute P3HT was investigated by collecting single point time transients from a dilute CdSe/P3HT sample in a confocal microscope. Representative transients are shown in Figure 7.7a,b. These data were recorded with 20 ms time resolution. The data shown were acquired using CdSe NR concentrations in the casting solutions of 0.5 mmol/L and 0.65 mmol/L for CdSe/P3HT and CdSe/PMMA samples, respectively. These were the most dilute solutions investigated. Samples prepared at higher NR concentrations showed evidence of the effects of aggregation and have been excluded from the analysis, while data obtained from the dilute samples suggest that there is little or no communication between nanorods. Data analysis involved calculating the "on" and "off" times for the NRs. A thresholding procedure was used for this purpose. The threshold between "on" and "off" signal levels was determined in each case by first finding the global background signal level. The threshold was selected to occur at the 0.01% probability level on the Poisson (approximated by a Gaussian) distributed background. Histograms prepared from the "on" and "off" time data show clear power law behavior. Representative distributions are shown in Figure 7.7c-f. The power law exponents derived by fitting these data to eq 1 depict significant differences in both the "on" and "off" time distributions for dilute CdSe/PMMA and dilute CdSe/P3HT films. Table 7.1 gives the "m_{on}" and "m_{off}" values obtained from the calculation.

$$P(\tau) = A\tau^{m_{on/off}} \qquad (1)$$

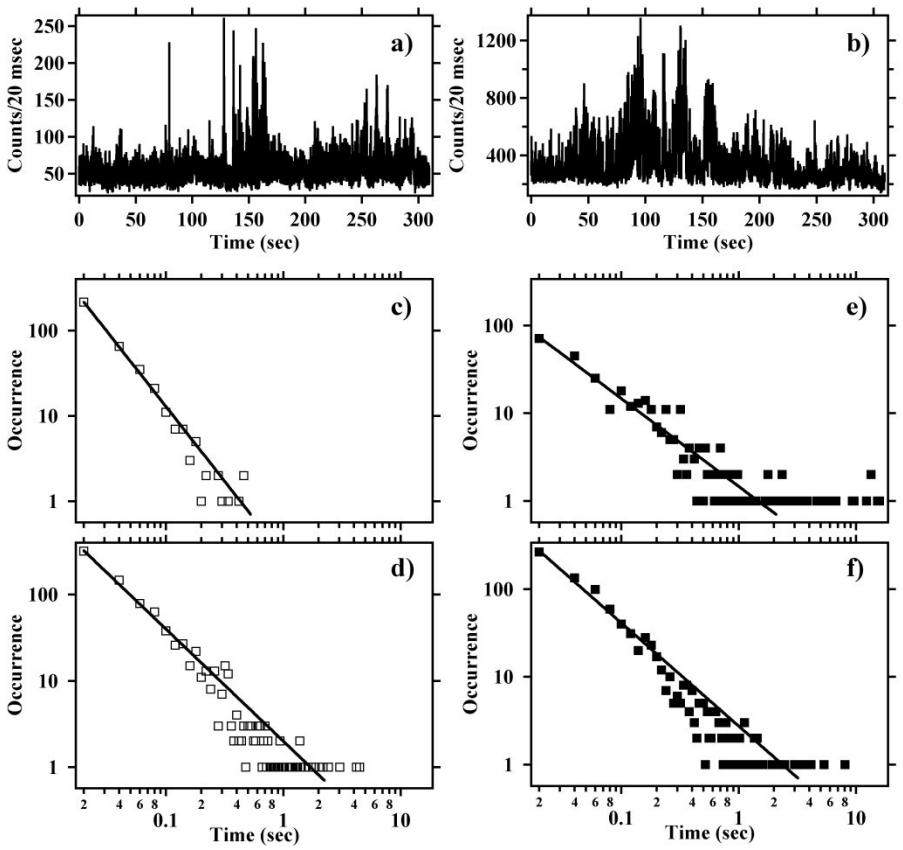

Figure 7.7 (a), (b) Representative time transients for single locations in dilute CdSe/PMMA and dilute CdSe/P3HT films, respectively. Both transients were recorded at 2.1 μW input power (488 nm). (c), (d) "On" time histograms for dilute CdSe/PMMA and dilute CdSe/P3HT films, respectively. (e), (f) "Off" time histograms for the same data sets. The data points shown in (c-f) are derived from (a) and (b); the solid lines depict fits to the power law expression given in the text. The power law exponents determined from the fits are (a) mon = -1.30, moff = -1.18 and (b) mon = -1.66, moff = -1.00. Mean values for the power law exponents determined from several measurements on different nanorods are given in Table 1. The CdSe NR concentrations in the casting solutions were 0.5 μmol/L and 0.65 μmol/L for CdSe/P3HT and CdSe/PMMA samples, respectively.

The mean values for m_{on} in PMMA and P3HT differ at > 90% confidence, for samples having similar concentrations of NRs. The results indicate the "on" times are appreciably longer for CdSe NRs in contact with dilute P3HT. Likewise, the "off" time distributions for the CdSe/P3HT films yielding larger (more negative) m_{off} exponents, reflective of shorter NR "off" times. The mean values for m_{off} in CdSe/PMMA and CdSe/P3HT films differ at ~ 86% confidence.

The values obtained for m_{on} and m_{off} exhibit little or no dependence on incident power (see Table 7.1).

Power (μW)/Film	PMMA m_{on}	P3HT m_{on}	PMMA m_{off}	P3HT m_{off}
0.7	-1.76 (±0.19)	-1.64 (±0.15)	-1.19 (±0.08)	-1.17 (±0.08)
1.4	-1.67 (±0.31)	-1.50 (±0.18)	-1.15 (±0.13)	-1.25 (±0.15)
2.1	-1.82 (±0.30)	-1.53 (±0.15)	-1.15 (±0.16)	-1.20 (±0.05)
Mean	*-1.75 (±0.27)*	*-1.56 (±0.17)*	*-1.16 (±0.12)*	*-1.21 (±0.10)*

Table 7.1 Power law exponents for single CdSe nanorod blinking. The values reported are averages (and standard deviations) obtained from ten separate time transients in each case.

While power dependences have been observed previously for the "on" time exponent, exhibiting a shortening of "on" times at high powers, the "off" time exponents are often found to be independent of incident power.[99] Any power dependence in m_{on} in the present samples is likely masked by the relatively large variability in the measured values.

The differences in m_{on} for the CdSe/PMMA and CdSe/P3HT samples are reflective of charge transfer interactions between P3HT and the NRs. The longer "on" times in P3HT are specifically attributed to the transfer of electrons from the P3HT to trap sites on the NRs. In PMMA, the NR trap sites instead capture electrons from photogenerated NR excitons, preventing radiative recombination and leading to relatively longer dark states. Filling of the traps by charge transfer from P3HT thus lengthens the "on" times. In a similar manner, charge transfer from the P3HT to the NRs also has the effect of shortening the "off" times by preventing charge trapping.

In order to better understand the effects of light exposure, and associated charge generation, on the bandedge and trap emission characteristics of CdSe NRs in P3HT and PMMA films, confocal images were acquired from these samples before and after prolonged irradiation of single points in each. In these studies, bandedge and trap emission images were simultaneously recorded on two separate avalanche diode detectors. Images were acquired of identical sample regions before and after irradiation at several specific points for periods of approximately 15 min at fluences of ~ 1000 W/cm^2. The observations are summarized in Figure 7.8. Comparison of these images shows that bandedge emission is bleached and trap emission is enhanced in both PMMA and P3HT matrices. However, the relative enhancement of trap emission is significantly higher for the CdSe/PMMA sample than for CdSe/P3HT. This is opposite to what was observed above, for short irradiation times at lower fluences in the wide-field geometry, where the bandedge emission from CdSe/P3HT materials was enhanced (see Figure 7.6).

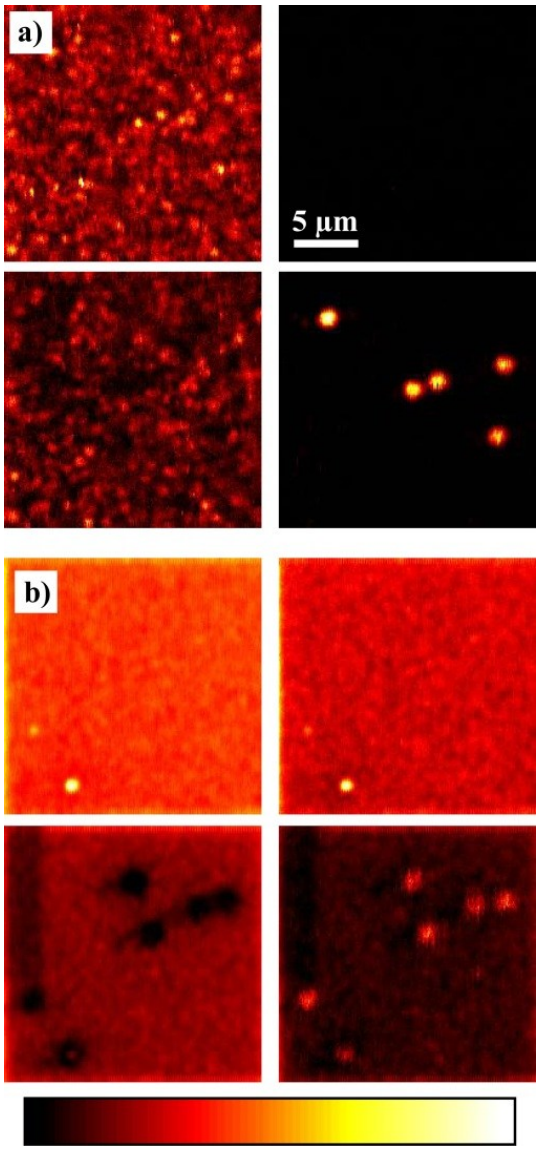

Figure 7.8 (a) Bandedge (left) and trap (right) emission images from a CdSe/PMMA film before and after irradiating at 5 different points. (b) Bandedge (left) and trap (right) emission images from a CdSe/P3HT composite sample before and after irradiating at 6 different points. The color scale in these images depict signal ranges of (a, left) 30-350 counts, (a, right) 60-3000 counts, and (b, left) 2,000-20,000 counts, (b, right) 300-2500 counts. Confocal images are shown; the pixel integration time was 20 msec. The CdSe NR concentrations in the casting solutions were 3.05 µmol/L and 4.22 µmol/L for CdSe/P3HT and CdSe/PMMA samples, respectively.

Similar data from PMMA and dilute P3HT/PMMA films in the absence of NRs are shown in Figure 7.9. These latter show no change in the case of PMMA and only uniform bleaching in the case of the dilute P3HT/PMMA blend.

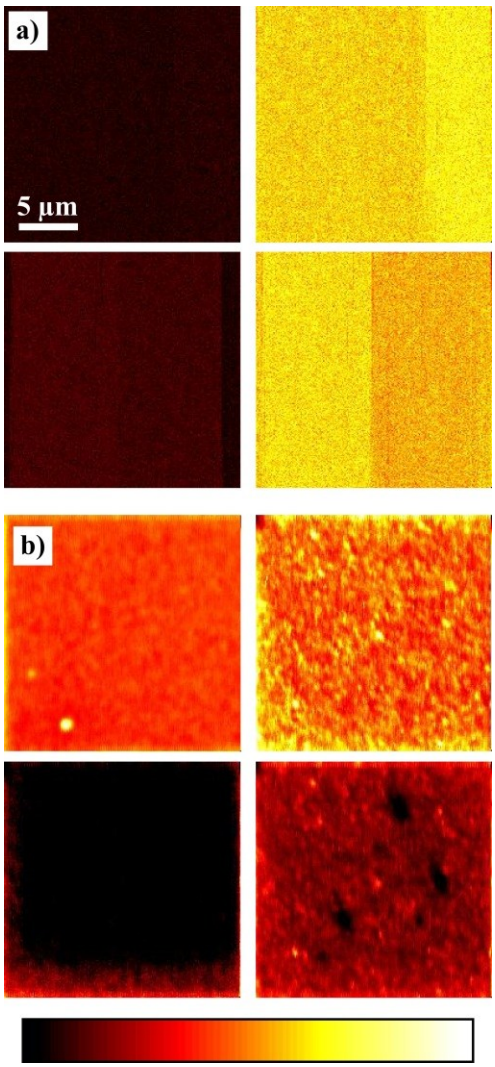

Figure 7.9 (a) PMMA background emission at the CdSe bandedge (left) and trap (right) emission wavelengths before and after irradiating at 3 different points. (b) Bandedge (left) and trap (right) emission images from a dilute P3HT/PMMA film before and after irradiating at 3 different points. The color scale in these images depict signal ranges of (a, left and right) 0-200 counts, and (b, left) 300-1,000 counts, (b, right) 400-4000 counts. Confocal images are shown; the pixel integration time was 20 msec.

Based on the above observations, the following simple model is proposed to describe the data presented. A pictorial view of this model is given in Figure 7.10. P3HT is known to be an electron donor, due to its band alignment with respect to CdSe. When P3HT is mixed with CdSe NRs, electron transfer takes place, filling charge trapping sites on the NR surface. Filling of NR charge traps results in enhanced emission rates from individual NRs and aggregates and also leads to an increase in the number of CdSe NRs observable in the images. A core-shell structure has also been shown to improve bandedge emission by preventing formation of surface trap

states.[108] Although a core-shell structure would improve the bandedge emission,[91] the presence of a shell would also prevent direct interactions between P3HT and the NRs.

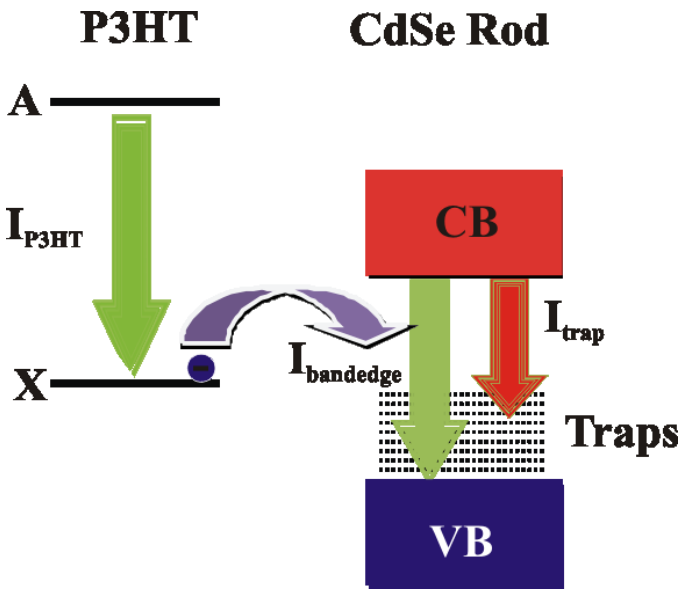

Figure 7.10 A simple model for the emission observed in the experiments as well as the relative band alignment of the P3HT and CdSe nanorods.

The lack of an overcoat is well-known to facilitate electronic communication between inorganic quantum confined structures and semiconducting organic polymers.[45,77,80,99,102] As the purpose of the present study was to explore direct interactions between the NRs and P3HT, bare CdSe NRs were employed instead.

From the above results, it is important that significantly (i.e. 10X) more emission is observed from CdSe/P3HT films than from CdSe/PMMA materials. This clearly means that the CdSe NRs in P3HT spend more time in the emissive bandedge state than in the dark state/emissive trap state. The role of the emissive trap state in governing the NR emission dynamics is presently being explored. The photoactivation of bandedge emission is also explained *via* electron transfer from the P3HT. Based on the NR and P3HT concentrations, and under the assumption of a homogeneous mixture of the two, the average NR-P3HT separation is estimated to be 2 nm. It is clear from this estimate that some P3HT molecules will be in contact with the NRs, providing a direct route for charge transfer. While some NRs may not be directly in contact with P3HT, the average separation is sufficiently short that some tunneling of charges through the PMMA matrix could also occur. It can also be hypothesized that if photoactivated

electron transfer takes place from P3HT to the NRs, we should also observe its affects on the trap state emission of the CdSe NRs in CdSe/P3HT materials, relative to what is observed in PMMA. As noted above, trap state emission is significantly enhanced in CdSe/PMMA films (see Figure 7.9) while in the CdSe/P3HT films trap enhancement is significantly less. We conclude that reduced trap emission in P3HT after light exposure results from electron transfer from P3HT to the NRs and associated filling of the trap states. Also, the traps filled by the electrons in CdSe NRs produce increased bandedge emission, but decreased trap state emission. A related photoactivated efficiency increase was also recently observed during working with CdSe nanocrystal/P3HT solar cells exposed to the laboratory ambient environment.[109] In this study, Yang *et. al*. showed that the current density of their cells increased in the first 25 minutes of light exposure before later decreasing.

7.4 Conclusions

In summary, hybrid inorganic/organic semiconducting films comprised of CdSe NRs dispersed in dilute P3HT/PMMA blends have been investigated by optical microscopy and spectroscopy. The results obtained were compared to those from CdSe/PMMA films. The fluorescence properties of the CdSe NRs were found to be affected by charge transfer from the dilute P3HT/PMMA matrix to the NRs. Interfacial charge transfer between the NRs and P3HT led to luminescence activation of the NRs and enhancement of bandedge emission from the NRs by trap state filling. Trap state filling by electron transfer from P3HT also altered the "on" and "off" time distributions in NR blinking experiments. Electron transfer from P3HT to the NRs was also reflected by enhanced trap emission observed for NRs dispersed in PMMA, relative to those in dilute P3HT. The results of these studies will be useful to those seeking to prepare CdSe NR/P3HT blends for use in solar energy conversion devices and for further photophysical investigations.

Chapter 8 - Investigation of Trap State Emission of CdSe Nanorods in PMMA and PMMA/P3HT matrix

8.1 Introduction

The development of novel photovoltaic devices for solar energy conversion requires photoactive materials that are efficient, durable, and easy to manufacture. Many of the most promising new materials that meet these requirements are hybrid systems consisting of inorganic nanostructures embedded in conductive polymer matrices.[110-114] For example, functional solar cells have been prepared from CdSe quantum dots, rods, and tetrapods dispersed in the conductive polymer poly-3-hexylthiophene (P3HT).[114] Hybrid CdSe/P3HT materials are good candidates for tandem solar cells that capture light in two stages because CdSe has a relatively large bandgap and efficiently captures light from the blue part of the solar spectrum. The best CdSe/polymer solar cells produced to date have efficiencies reaching 2.6-2.8%, depending on the structure of the nanoparticle.[115] Among other factors, the surface quality of the nanoparticles[116] and the interaction of the coating ligands with the matrix[117] determine the overall efficiency and durability of these materials. Further improvement of hybrid inorganic/organic solar cell materials therefore requires a better understanding of the fundamental details of charge separation and migration across the interface, as well as possible chemical changes that occur following the absorption of light.

One way to study the underlying processes that inhibit solar energy conversion in hybrid nanoparticle/polymer materials is to observe the nanoparticle fluorescence. Fluorescence measurements monitor the charge carrier dynamics, including charge trapping and recombination, because the emission of light occurs upon radiative recombination of an electron and a hole. The fluorescence intensity of a material is therefore proportional to the number of radiatively recombining electron-hole pairs and the emission wavelength reports on their relative energies. Fluorescence intermittency (or blinking) measurements reveal charge trapping and other processes that potentially inhibit energy conversion by blocking the formation and transport of new charge carriers,[118-122] whereas time-resolved fluorescence decay measurements provide information about the kinetics of the excited system.

The fluorescence intermittency or blinking behavior of CdSe semiconductor nanoparticles has been of interest in the scientific community over the past decade. [118-122] In the blinking

measurements, nanoparticles are characterized by fluorescent (ON) and non-fluorescent (OFF) states, where the ON and OFF times of a quantum confined structure under continuous illumination typically follow a power law.[122] Experiments and theory indicate that blinking is a result of charge trapping that temporarily leaves the nanoparticle in a charged state, thus preventing further excitation and/or emission.[72,123] Because charge trapping generally occurs at the interface, various methods have been used to minimize trapping effects by protecting the surface of the nanoparticle. For example, growing a shell of large-bandgap semiconductor around the CdSe nanoparticle has been shown to suppress surface traps and improve the overall emission quantum yield,[124] although tunneling to the surrounding matrix can still play a role in charge trapping.[123] Recently, Jander, et al.[125] found that the intermittency of CdSe nanorod emission was suppressed when the nanorods are located near an amorphous carbon layer due to Forster-type energy transfer that efficiently competes with charge transfer to trap sites. Similar to the work by Jander et al., some of us[126] observed longer ON times and increased fluorescence intensity for CdSe nanorods in the presence of the conductive polymer P3HT. The increased fluorescence of CdSe nanorods in the presence of P3HT was attributed to a decrease in the number of surface traps via static charge transfer from the conductive polymer.[126]

Understanding interfacial charge carrier dynamics at and across the CdSe/polymer boundary therefore requires further investigation of the nanoparticle emission properties. In addition to bandedge emission, in which conduction band electrons recombine with valence band holes, trap state emission has been discussed in the literature.[127,128] Trap state emission below the bandedge energy can be attributed to the radiative recombination of trapped electrons with valance band holes, conduction band electrons with trapped holes, or trapped electrons with trapped holes. The electron and hole traps are defects that lie energetically between the valence band and conduction band. Emission from conduction band electrons recombining with hole traps and from trapped electrons recombining with valance band holes have both been observed in the literature, depending on the relative composition of the nanoparticle surface.[127,128] For example, some of us recently observed relatively strong emission below the bandedge for CdSe nanorods dispersed in a polymethylmethacrylate (PMMA) polymer matrix.[126] The relatively strong trap state emission of the CdSe nanorods was attributed to radiative recombination of conduction band electrons with trapped holes (defect sites) lying above the valence band. Importantly, the addition of dilute

P3HT enhanced the relative bandedge emission of the CdSe nanorods by filling the intraband defects of CdSe with electrons via charge transfer from the P3HT.[126]

In this part of the thesis, we present complementary single particle fluorescence intermittency and ultrafast transient absorption measurements that provide deeper insight on the interfacial dynamics and charge trapping behavior of CdSe nanoparticles. Specifically, we probe the interaction between bare, uncoated CdSe nanorods and dilute P3HT dispersed in PMMA by monitoring the bandedge and trap emission of the nanoparticles. New single point fluorescence intermittency measurements presented here support a three-state model for fluorescence blinking that includes distinct bandedge emission, trap emission, and dark (OFF) states. Here, bandedge emission refers to fluorescence at the bandedge energy of CdSe nanoparticles, whereas "trap emission" indicates radiative relaxation of a conduction band electron to a localized defect (hole trap) located above the valence band of CdSe.[129] We show that the trap emission and bandedge emission are negatively correlated, indicating that the three emission states of the nanoparticle are distinct, and that the switching among these emissive and dark states occurs on a milliseconds to seconds time scale under continuous irradiation. Complementary femtosecond transient absorption measurements probe the interfacial charge transfer and ultrafast recombination dynamics by monitoring the stimulated emission of CdSe nanorods following optical excitation of P3HT. The ultrafast measurements confirm that there is efficient charge transfer from P3HT to CdSe upon photoexcitation of the conductive polymer and verify the nature of the trap emission in the microscopy experiments. Finally, we explore the role of photochemical etching in creating new surface trap sites, and comment on the chemical composition of the traps. Collectively, these experiments provide a detailed view of the interfacial dynamics and charge trapping behavior of CdSe nanorods in an environment that closely resembles functional hybrid nanoparticle/polymer solar cell materials.

8.2 Experimental Methods

Synthesis of CdSe nanorods:

CdSe nanorods were synthesized under oxygen-free conditions.[72] The reaction mixture, comprised of 50 mg of CdO, 4.1 g of trioctylphosphine oxide (TOPO) and 305 mg of tetradecylphosphonic acid (TDPA), was prepared in a three-neck flask with septum, a thermometer and a refluxing column. The refluxing column was attached to a Schlenk line. The

solution was first heated to 120 ^{o}C under Argon flow and subsequently placed under vacuum for 1 hr. A selenium-trioctylphosphine (SeTOP) solution was prepared separately in a nitrogen-filled glovebox. A mixture of 4 ml of trioctylphosphine (TOP) and 42 mg of Se powder were placed into a vial that was then capped with a septum. The solution was stirred in the glovebox with a magnetic stirrer. The Se dissolved in TOP in ~ 0.5 hr. The solution temperature was then raised to 280 °C, after which it became golden yellow. At this point, the cadmium solution was returned to atmospheric pressure and the temperature was increased to 270 °C. The SeTOP solution was then injected and the solution temperature decreased to 230 °C. Growth of the nanorods was performed at 260 °C. The entire growth process was monitored by UV-visible and photoluminescence spectroscopy. Nanorod growth was terminated after ~ 5 min. Methanol was added to the reaction mixture once the solution had cooled to room temperature. The mixture was then centrifuged and the supernatant was discarded. This process was repeated five times. A dark red solution was obtained when the nanorods were dissolved in spectroscopic grade toluene. The crude reaction mixture was washed thoroughly with methanol to remove the phosphine ligands. The binding strength of the ligands is sufficiently low that they are easily removed by washing with organic solvents.[130]

Etching of CdSe nanorods:

The etching of the CdSe nanorods was performed in a temperature controlled fiber optic fluorescence setup. A diode laser of wavelength 405 nm and 6.5 mW power was used to excite the sample continuously. The solutions were placed in quartz fluorescence cuvettes and were heated at 40 °C for 72 hours with continuous stirring. Photoluminescence spectra were recorded at five minute intervals. The data on trap formation at elevated temperature are not presented here. Only the photoluminescence spectra recorded at room temperature before and after heat treatment are included.

Film preparation:

Two different types of film containing the CdSe nanorods were prepared. The first was a CdSe/PMMA composite, and the second was a CdSe/P3HT/PMMA composite where the nanorods were dispersed in a PMMA film doped with dilute P3HT. PMMA (MW=120,000 g/mol) was obtained from Sigma-Aldrich and was used as received. P3HT (regioregular form,

MW=20,000-70,000) was obtained from American Dye Source and was also used as received. Two separate PMMA solutions were prepared by dissolving 0.05 g of PMMA in 2 mL of chloroform. To the first PMMA solution, 2 mL of nanorods in toluene was added and mixed well. A solution of P3HT was prepared by dissolving 0.003 g of P3HT in 4 mL of chloroform. A 0.04 mL aliquot of this P3HT solution was then added to the second PMMA solution, yielding a 6% (by wgt) mixture of P3HT in PMMA. A 2 mL aliquot of nanorods in toluene was then added to the PMMA/P3HT mixture and mixed well. The CdSe/PMMA and CdSe/P3HT/PMMA films were obtained by spin casting (1500 rpm, 1 min) a single drop of the appropriate solution onto a glass cover slip (FisherFinest). Film thickness was determined on a spectroscopic ellipsometer (J. A. Woolam, α-SETM). Average thicknesses of the CdSe/PMMA and CdSe/P3HT/PMMA composite films were 49 ±23 nm and 53 ±32 nm, respectively.

Confocal microscopy:

Single point fluorescence measurements under continuous irradiation were acquired over several hundred seconds using a sample-scanning confocal microscope that has been described previously.[131] Briefly, this system is built upon an inverted epi-illumination microscope (Nikon TE-300). The composite films were placed on top of a closed-loop piezoelectric x,y-scanning stage (Sifam Instruments) attached to this microscope. A diode laser (Spectra-Physics, Cyan Scientific, 488 nm) was used as the excitation source. The laser light was directed into the epi-illumination port of the microscope and reflected from a dichroic beam splitter (Chroma, 505 DCLP) into the back aperture of an oil immersion objective (Nikon Plan Fluor, 1.3 numerical aperture, 100× magnification). The fluorescence was collected with the same objective and passed back through the dichroic beam splitter and subsequently through a holographic notch filter. The bandedge and trap emission were separated by directing the fluorescence onto a 700 nm dichroic shortpass filter (Chroma E700sp). The reflected trap emission was further filtered with a 700 nm longpass filter, while the transmitted bandedge emission was directed through a 580 nm band-pass filter with 40 nm bandwidth. The bandedge and trap emission were detected simultaneously, using separate single photon counting avalanche photodiodes. Fluorescence images were acquired by raster scanning the sample above the focused laser spot. The fluorescence signal was integrated for 20 ms per pixel in 200 × 200 pixel images of 20 × 20 μm^2

sample regions. Single point fluorescence time transients were collected by recording the spectrally integrated fluorescence in time from selected points in the sample.

Statistical properties for the lifetimes of the bandedge and trap emission states were obtained from single point fluorescence intermittency measurements under continuous irradiation with 488-nm light. Separate threshold limits for ON and OFF states were assigned to each fluorescence channel, with the threshold values set to twice the standard deviation of the background signal. An emission channel is considered ON when the emission intensity exceeds the threshold for that channel. If both channels are below threshold, the system is considered to be in the dark OFF state. We observe that the bandedge emission, trap emission, and OFF times follow power-law distributions having different exponents. Instances where both emissions exceed the threshold are rare, typically less than one percent of the total measurement time, which justifies the use of a three-state model with distinct ON states. However, dual-emission points are included in the statistical analysis, and are assigned to the emissive state (bandedge or trap) with the largest signal above threshold.

Widefield video microscopy:

Fluorescence videos were recorded on a widefield microscope that has been described previously. Briefly, this system is built upon an inverted epi-illumination microscope (Nikon Eclipse Ti). A diode laser (Spectra-Physics, Cyan Scientific, 488 nm) was used as the excitation source. For uniform illumination of the sample, the laser light was passed through a spinning optical diffuser and then reflected from a dichroic beamsplitter (Chroma, 505 DCLP) and into the back aperture of an oil immersion objective (Nikon Apo TIRF 100x, 1.49 N.A.). The incident laser power was maintained in the 1 mW range throughout these experiments. Fluorescence from the sample was collected in reflection and was separated from the excitation light by passage back through the dichroic beamsplitter. The fluorescence was subsequently directed through an image splitter (Cairn Research, Optosplit II) fitted with a dichroic beamsplitter (Chroma XXX). The bandedge emission was subsequently passed through a 580 nm bandpass filter (40 nm passband) and the trap emission through a 700 nm longpass filter. In this experimental setup, the bandedge emission and the trap emission were recoded simultaneously. A back-illuminated EM-CCD camera (Andor iXon DU-897) was used as the detector.

Transient absorption:

Ultrafast transient absorption measurements were performed using a regeneratively amplified Ti:sapphire laser (Legend Elite USP; Coherent) that produces 35-fs pulses of light at a repetition rate of 1 kHz. Non-linear frequency conversion of the 800-nm laser fundamental in an optical parametric amplifier (TOPAS-C; Light Conversion) generates pump pulses at 630 nm. The pump pulses were attenuated to 0.25 μJ and gently focused to a spot size of 1 mm at the sample. The attenuated pulses have a duration of about 120 fs. Probe pulses in the range 450-765 nm were obtained by focusing a small amount of the fundamental laser light into a 3-mm sapphire window to produce broadband continuum, which is then collimated and passed through two colored-glass filters to remove the residual 800 nm fundamental and sample-damaging UV radiation, respectively. An off-axis parabolic mirror focuses the probe to a spot size of 0.1 mm at the sample, where it is overlapped with the pump beam. After passing through the sample, an imaging spectrograph disperses the continuum probe light onto a 256-pixel silicon photodiode array for shot-to-shot detection. The time-dependent transient absorption spectra were obtained by averaging 2000 laser shots at each delay time, with a 500 Hz chopper blocking every other pump pulse for active background subtraction. Transient spectra are dispersion-corrected to account for the wavelength-dependent arrival time of the probe light. The transient absorption measurements use CdSe/PMMA, P3HT/PMMA, and CdSe/P3HT/PMMA samples with the same composition as described above, except that the film thickness was reduced to give optical densities below 1.0 OD. The laser fluence of ~30 $\mu J/cm^2$ was well below the reported damage threshold for CdSe nanoparticles.[132]

8.3 Results and Discussions

Fluorescence intermittency:

The representative fluorescence microscopy images in Fig. 1 show the intensity of bandedge and trap emission for CdSe nanorods dispersed in PMMA and P3HT/PMMA films under continuous irradiation at 488 nm. This wavelength excites both CdSe nanorods and the P3HT polymer, although the emission signal is almost entirely from the nanorods. The strongly localized CdSe emission reveals the locations of the nanorods in each image, whereas the diffuse P3HT emission bleaches within a few seconds and therefore contributes only weakly to the overall background

signal. The early time evolution of the P3HT emission is excluded from the temporal analysis of the confocal microscopy data (below) in order to selectively investigate the behavior of CdSe emission states. The wide-field microscopy images in Fig. 1 show that both bandedge and trap emission are relatively weak for CdSe nanorods dispersed in a PMMA matrix, but that the bandedge emission of the nanorods is dramatically enhanced in the presence of dilute P3HT. Trap emission is also slightly enhanced in the presence of P3HT, but not to the same extent as the bandedge emission.

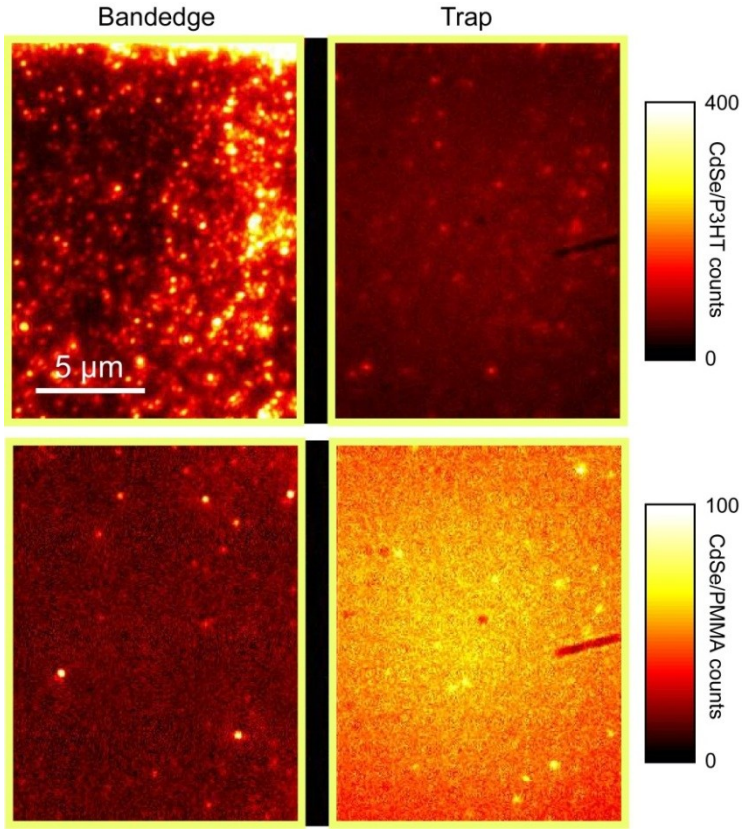

Figure 8.1 Widefield fluorescence microscopy images of the bandedge emission (left) and trap emission (right) from CdSe nanorods in a CdSe/P3HT/PMMA film (top panels) and in a CdSe/PMMA film (bottom panels). The relative emission rate depends on sample, as indicated by the color scales, with the highest overall emission observed for CdSe/P3HT/PMMA. The videos used to produce these images are included in the Supporting Information (Videos S1 and S2). Images shown here depict the final frame of each video. In the right images the background count is somewhat higher due to the larger bandwidth of the filer used in the experiment.

As shown previously,[126] neither the bandedge nor the trap emission signals from these samples are stable. Rather, they exhibit dramatic fluctuations in time (i.e., fluorescence intermittency), as

shown in the widefield microscopy videos provided as supporting information. Using a confocal microscope to simultaneously record fluorescence time transients for both the bandedge and trap emission states at single sites in each film provides a unique opportunity to observe the competition between the two emissive states. Representative examples of such transients, acquired with ms time resolution, are shown in Figure 8.2.

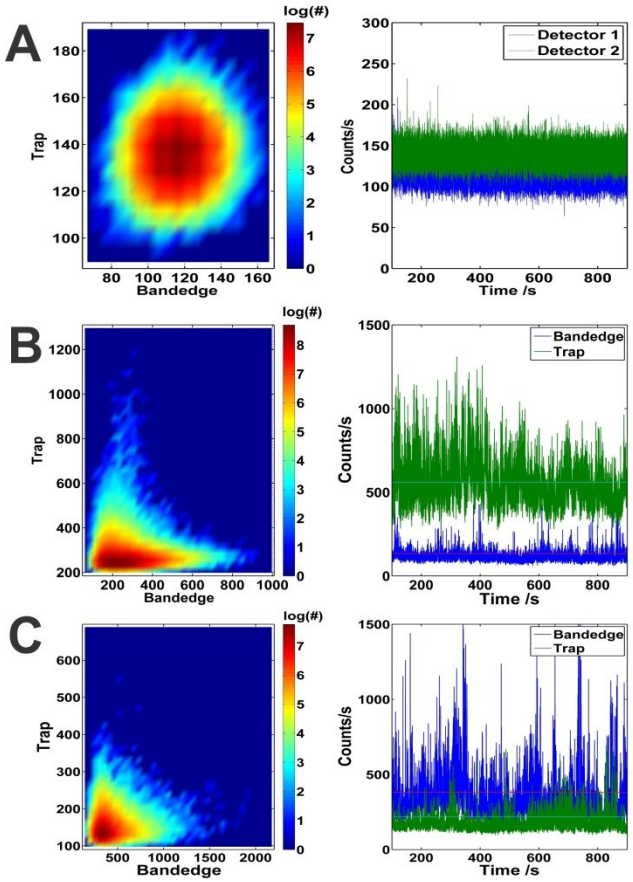

Figure 8.2 Correlation maps (left) and fluorescence time transients (right) for the simultaneously measured bandedge and trap emission channels at a single site using confocal microscopy. The panels from top to bottom show the uncorrelated dark counts of the instrument (A), and anti-correlated CdSe nanorod emission signals for CdSe/PMMA (B) and CdSe/P3HT/PMMA (C) films.

The right side of Figure 8.2 shows the state-specific, single-point emission signals as a function of time for CdSe nanorods in CdSe/PMMA and CdSe/P3HT/PMMA films. The detector dark counts are also plotted for comparison (top panel). The left half of Figure 8.2 shows the aggregate probability distributions as a function of emission intensity in the bandedge and trap emission channels. These 2D color maps demonstrate that the fluctuations in the two channels

are anti-correlated for the CdSe/PMMA and CdSe/P3HT/PMMA samples. That is, high signals in one channel are only observed with low signals in the other channel, leading to relatively high intensity along the two axes and low intensity along the diagonal of the correlation plots in Figure 8.2. These results stand in strong contrast with the uncorrelated dark counts from the instrument (Fig 8.2A). The correlation maps indicate that only one emission state (bandedge or trap) is likely to be observed within the 20 ms signal integration time of the dual-channel fluorescence intermittency measurements. In principle, the switching between these two emission channels could take place over a wide range of timescales, but we conclude that the typical switching time must be longer than the integration time of the microscope.

The microscopy images in Figure 8.1 and the single point emission data in Figure 8.2 both demonstrate an increased likelihood of detecting bandedge emission from the nanorods in the presence of P3HT compared with the undoped PMMA matrix. This behavior was previously attributed to static electron transfer from P3HT that fills the low-lying, unoccupied trap sites at the surface of the CdSe nanorods and in the PMMA matrix.[126] In the present paper, a quantitative analysis of the switching rates reveals how doping the PMMA matrix with P3HT affects both the bandedge and trap emission from CdSe. The observation of distinct emission processes in these experiments allows for the relative switching rates among all three states of the CdSe nanrods (i.e., bandedge emission, trap emission, and dark states) to be determined. The probabilities of switching between each of the three available states are reported in Table 8.1.

	CdSe/PMMA	CdSe/P3HT/PMMA	Significance
Bandedge State→OFF State	24.6±2.9	21.5±1.6	93%
OFF State→ Bandedge State	24.8±2.9	21.6±1.6	95%
Trap State→Bandedge State	1.36±0.27	2.25±0.28	>99%
Bandedge State→Trap State	1.63±0.33	2.33±0.28	>99%
Trap State→OFF State	23.9±2.8	26.2±1.5	84%
OFF State→ Trap State	23.7±2.8	26.1±1.5	88%

Table 8.1 Relative probabilities of switching between trap emission, bandedge emission and OFF states in CdSe nanorods in PMMA and P3HT/PMMA matrices. Error bars depict the 95% confidence interval. Significance gives the confidence level at which the pairs of measurements differ in a t-test.

The values in the table represent the probability that the signal will change from one particular state to another in successive time points. For example, the change from bandedge emission to the OFF state accounts for 24.6% of all observed transitions in the CdSe/PMMA sample, but only 21.5% of transitions for CdSe/P3HT/PMMA. The ON times for bandedge and trap emission as well as the OFF times for the dark state of the CdSe nanorods in the CdSe/PMMA and CdSe/P3HT/PMMA films were analyzed by fitting the data with a power law function, $P(t) \propto t^{\alpha}$. The results are summarized in Table 8.2, which shows that the observed lifetimes of both ON states (bandedge emission and trap emission) are longer in the presence of the P3HT.[126]

$P(t) \approx t^{\alpha}$	CdSe/PMMA	CdSe/P3HT/PMMA	Significance
OFF State	-1.19±0.07	-1.10±0.04	97%
Bandedge State	-1.92±0.10	-1.8±0.06	96%
Trap State	-2.1±0.08	-1.88±0.05	>99%

Table 8.2 Power Law Exponents for Single CdSe Nanorod Blinking. Error bars depict the 95% confidence interval. Significance gives the confidence level at which the pairs of measurements differ in a t-test.

Several conclusions can be drawn from the relative switching probability data in Table 8.1. First, both ON states are significantly more likely to switch to an OFF state than to the other emitting state (i.e., bandedge→trap or trap→bandedge), consistent with the discussion above. In fact, observation of direct transitions between emissive states may simply reflect "missing" OFF states due to the limited time resolution of the microscope. Second, the complementary switching probabilities (e.g. trap→OFF and OFF→trap) are very similar for both bandedge and trap emission channels, suggesting that excitation of the system represents only a small perturbation of the overall dynamics of the CdSe blinking and that repeated optical excitation by the laser does not influence the overall fluorescence behavior. Third, the inclusion of P3HT in the matrix increases the probability for direct conversion from bandedge emission to trap emission, and vice versa. This result is probably an artifact of missed dark states, suggesting that the overall switching rate increases slightly in the presence of P3HT. The shortening of the OFF state lifetime in the presence of P3HT is proposed to result from filling of the trap states by electrons from P3HT. Fourth, the probability of switching from bandedge emission to the OFF

state decreases in the presence of P3HT, while the probability of switching from trap emission to the OFF state increases under these same conditions. The different relative probabilities for each transition are probably a result of the reduced intermittency of the bandedge emission state. The bandedge emission state blinks less in the presence of P3HT, so we observe fewer transitions into and out of this state relative to the other possible transitions. The relative probability of a transition involving the trap emission state increases, because P3HT reduces the blinking rate of the trap emission state to a smaller extent than for the bandedge emission state. Transitions between the two ON states become more likely in the presence of P3HT because of the reduced blinking of both states (i.e. less time in the dark state overall).

Ultrafast Charge Transfer Dynamics:

In order to probe the interaction between P3HT and the CdSe nanorods directly, we used ultrafast spectroscopy to observe the charge transfer dynamics following excitation of the conductive polymer at 630 nm. The top panel of Figure 8.3 shows the static absorption spectra of the CdSe/PMMA, P3HT/PMMA, and CdSe/P3HT/PMMA films that we studied. Samples of the dilute P3HT without CdSe nanorods and of the nanorods without P3HT reveal the dynamics of the individual components in the PMMA matrix and provide an important reference point for comparison with the composite CdSe/P3HT/PMMA film. A strong shoulder near 620 nm in the static absorption spectra of the films containing P3HT is similar to the interchain absorption band observed in well-ordered (e.g. crystalline) P3HT, and therefore indicates that the conjugated polymer is highly ordered.[133,134] Importantly, this low energy transition of the structurally ordered P3HT polymer extends well below the bandedge of the CdSe nanorods at ~580 nm. If the P3HT were amorphous, as in liquid solutions, we would not expect to see the strong absorption near 620 nm. In fact, the relative amplitudes of the absorption near 550 nm and 620 nm suggest that the presence of CdSe enhances the structural order of dilute P3HT in the CdSe/P3HT/PMMA film compared with a P3HT/PMMA film in the absence of nanorods.

The bottom panel of Figure 8.3 shows the transient absorption spectra of all three samples following excitation at 630 nm. These experiments exclusively excite the P3HT polymer because the excitation energy is below the bandgap of the CdSe nanoparticles, in contrast with the microscopy experiments, where both components are excited by the 488 nm photons. As expected, no transient absorption signal is observed for the CdSe/PMMA film, whereas

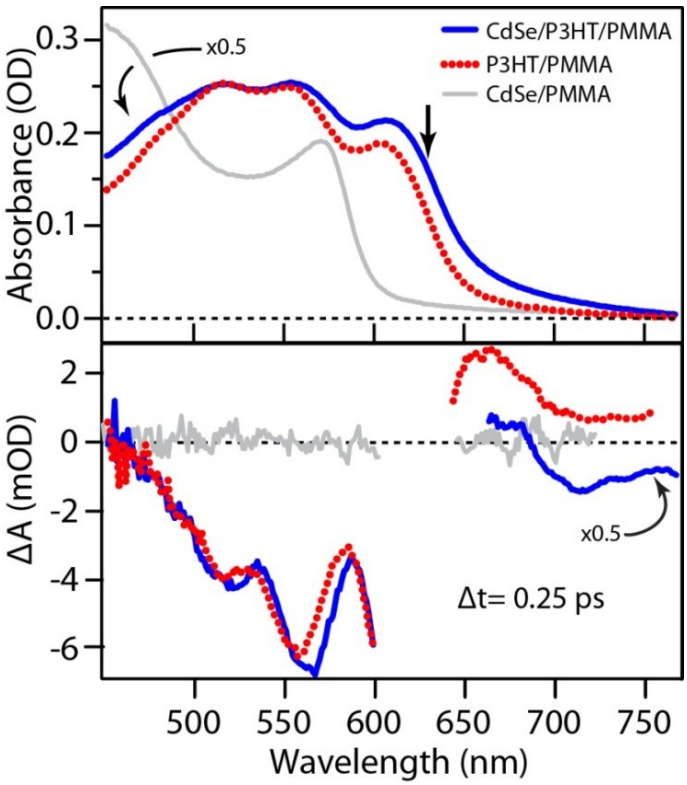

Figure 8.3 Top panel: Static absorption spectra of CdSe/PMMA, P3HT/PMMA, and CdSe/P3HT/PMMA films used in the transient absorption measurements. Bottom panel: Transient absorption spectra of all three samples at a delay of 0.25 ps following excitation at 630 nm.

excitation of the two samples containing P3HT leads to a strong transient response. Figure 8.4 compares the temporal evolution of the transient absorption at three different wavelengths for the P3HT/PMMA and CdSe/P3HT/PMMA films. The transient absorption spectrum of the P3HT/PMMA film at 0.25 ps has two main features, a negative band in the range 475-650 nm and a positive band in the region 650-765 nm. The negative signal closely matches the inverse of the static P3HT absorption spectrum and appears within the instrument response time. We assign this feature as the ground state bleach of the conductive polymer. The positive signal in the region near 665 nm also appears within the instrument response time, and then decays on a timescale of about 1 ps, consistent with an excited state absorption band that was previously reported in the same wavelength range for crystalline films of P3HT.[135] The dynamics of the P3HT/PMMA film are therefore consistent with the observation from the static spectrum that the P3HT conductive polymer aggregates into well-ordered, crystalline microdomains within the PMMA matrix.

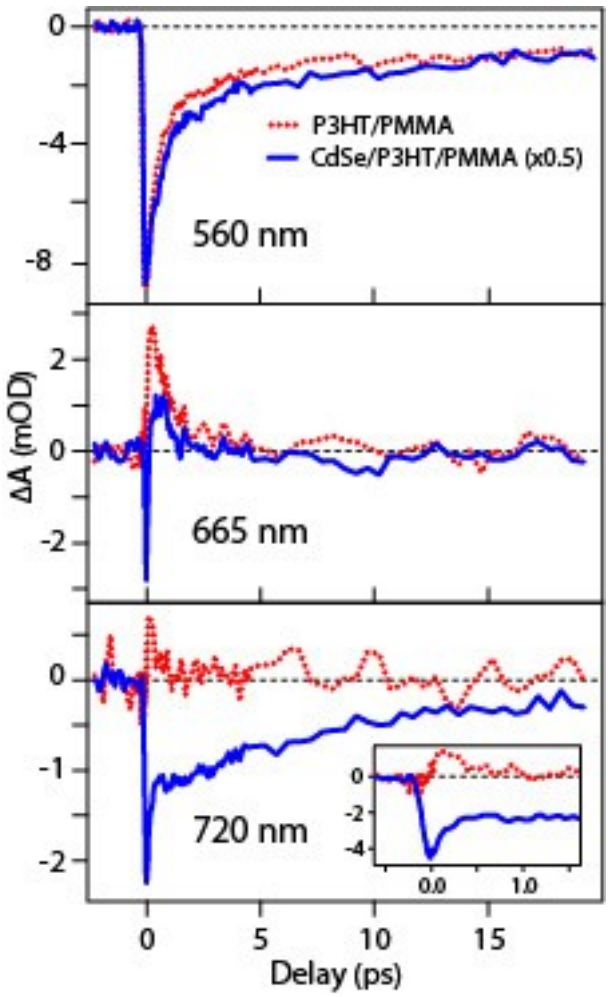

Figure 8.4 Transient absorption at 560, 665 and 720 nm as a function of delay following 630 nm excitation of P3HT/PMMA (dashed red line) and CdSe/P3HT/PMMA (solid blue line).

The transient absorption spectrum of the CdSe/P3HT/PMMA film is very similar to P3HT/PMMA, except that we observe an additional negative signal at wavelengths longer than ~675 nm. We assign this negative signal as stimulated emission from the conduction band of CdSe to unoccupied defect sites located above the valence band. The assignment is based on comparison with trap emission spectra from the microscopy experiments (see below) and the fact that the valence band of CdSe remains fully occupied under 630 nm excitation. The fact that we observe emission from the nanoparticles means that the charge transfer process must involve electron transfer to the nanorod, because there can be no emission from CdSe without first creating an excited state of the nanoparticle. Furthermore, the electron must radiatively recombine with a trapped hole lying above the valence band, because the valence band of the

nanoparticle is already full under these excitation conditions. Thus, the ultrafast measurement confirms the nature of the trap emission observed in the microscopy experiments.

The bottom panel of Figure 8.4 shows the temporal evolution of the stimulated emission band at 720 nm, where there is only a minimal contribution from the positive P3HT excited-state absorption. The signal at 720 nm reveals the relative population of charge carriers in the CdSe conduction band as a function of time. An instrument-limited rise of the emission signal indicates that the charge transfer from P3HT to the CdSe nanorods occurs within the ~150 fs time resolution of our experiment. This ultrafast charge transfer confirms that there is strong coupling between P3HT and the CdSe nanoparticles. The emission decays with sub-ps and few-ps timescales, suggesting two decay pathways.[136] The decay rates provide a direct measure of the interfacial charge carrier dynamics.

The transient absorption signal in the region of the P3HT ground-state bleach provides additional evidence for charge transfer from P3HT to the CdSe nanorods. Although scattering of the pump light obscures the transient spectra in the range 600-650 nm, the bottom panel of Figure 8.3 shows that the negative feature in the P3HT ground-state bleach near 550 nm shifts to longer wavelength by about 10 nm in the CdSe/P3HT/PMMA sample. Placing an electron in the conduction band of CdSe blocks a possible transition from the valence band, and results in a negative feature in the transient absorption spectrum (at the 575 nm bandedge) due to Pauli blocking. The negative signal in the CdSe/P3HT/PMMA sample therefore reports on both the ground-state bleach of P3HT and the conduction band charging of CdSe, consistent with the above description of the charge transfer dynamics.

Role of photoetching:

Trap emission from the CdSe nanorods can be related to the chemical composition of the nanoparticle surface. In the case of a cadmium rich surface, Knowles, et al.[137] observed the radiative recombination of delocalized conduction band electrons with trapped holes. Those authors point out that there are several emissive excitonic states present where the hole is not in its initial delocalized state. Kalyuzhny, et al. have shown that selenium rich CdSe samples due to the loss ligands could enhance the strong red shifted emission associated with traps.[128] Kalyuzhny's work is important because it provide an insight of the possible structural origin of the trap emission in CdSe nanorods.

It has been shown in the literature that either chemical or photochemical etching of CdSe can occur in the presence of chlorinated solvents.[138] Therefore, we propose that exposure of the CdSe/PMMA and CdSe/PMMA/P3HT samples to chloroform during film preparation is responsible for the defects that lead to the observed trap emission. To test this hypothesis, a solution of CdSe nanorods was heated at 40 °C for 72 hours in either toluene (Figure 8.5A and 8.5B), a mixture of equal portions of toluene and chloroform (Figure 8.5C and 8.5D), or a toluene-chloroform mixture with 0.05g PMMA added (Figure 8.5E and 8.5F). The left and right panels of Figure 8.5 show the normalized bandedge and trap emission spectra, respectively.

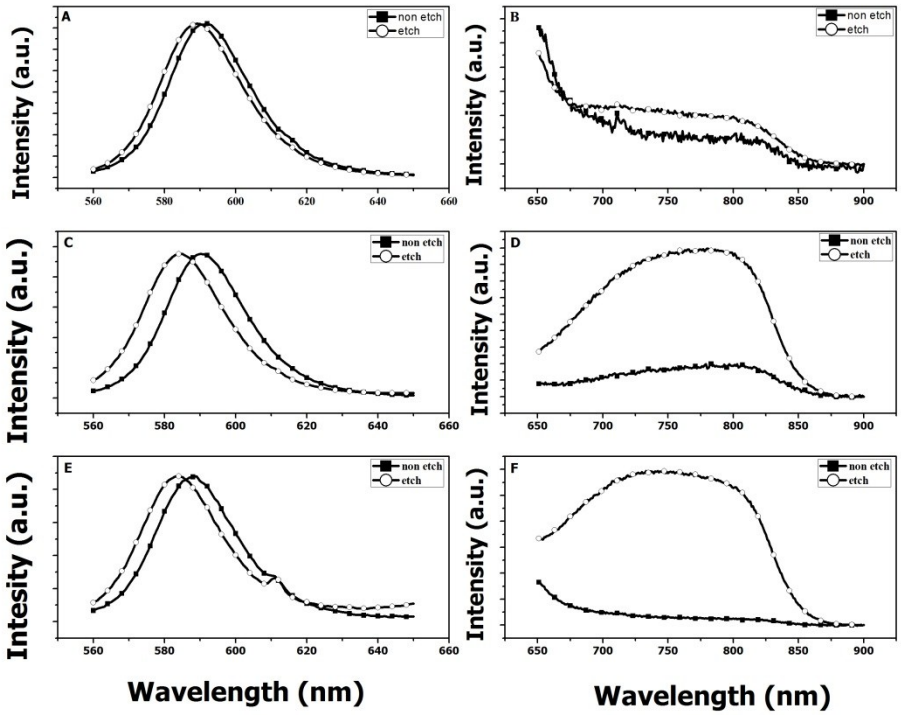

Figure 8.5 Bandedge (A, C, E) and trap state (B, D, F) emission of CdSe nanorods before and after etching treatment. Non etched and etched nanorods are represented as filled squares and hollow circles respectively. Nanorods in toluene are shown in panel A and B. An equal mixture of toluene and chloroform with nanorods are shown in panel C and D. An equal mixture of toluene and chloroform with nanorods and PMMA are shown in panel E and F. The spectra are normalized to the maximum of the bandedge emission.

It is observed that the trap state emission is enhanced in the presence of chloroform in both absolute terms and relative to the bandedge emission of the CdSe nanorods. Analysis of tunneling

electron microscopy (TEM) images of the nanorods before and after etching shows that the nanorods become shorter in length, while their diameters change little. The length of the CdSe nanorods were reduced by 34% while the diameter decreased by only 4%. The shift of the bandedge emission to shorter wavelength for the etched nanorods in Figure 8.5 is also consistent with the reduced Stokes shift with decreasing aspect ratio that was previously observed for CdSe nanorods.[139] It is clear from the data that the presence of chloroform causes removal of cadmium atoms from the CdSe, consistent with earlier findings.[138] Based on the TEM measurement, cadmium atoms are primarily removed from the ends of the nanorod. As Kalyuzhny, et al. showed, trap emission in the case of CdSe nanocrystals results from the binding of the residual Se atoms to coordinating TOP ligands.[128] In this previous work it was also observed that the trap emission gets stronger over time when the nanoparticles are exposed to light. This observation suggests that photochemical etching also occurs in the presence residual chloroform from solution processing of the nanorods. In our samples, trap state emission also became stronger with extended illumination of the PMMA samples. This effect was less pronounced when P3HT was added to the PMMA.[126]

Model for Bandedge and Trap Emission Dynamics

The excited state dynamics of CdSe nanorods dispersed in PMMA and PMMA/P3HT matrixes have been explored by both ms-scale fluorescence microscopy and by fs-scale transient absorption spectroscopy. These two experimental tools probe the dynamics on very different time scales. Nevertheless, they provide complementary data that reveals the important role played by charge transfer between P3HT and trap states in the CdSe nanorods in governing the observed nanorod emission characteristics. Figure 8.6 summarizes the processes involved. As noted above, enhanced bandedge emission is observed from the CdSe nanorods in the presence of P3HT (Figure 8.1). Static charge transfer from P3HT into unoccupied trap states positioned just above the valence band in the nanorods (see Fig. 8.6A) is believed to be the cause of enhanced nanorod emission. In the presence of unfilled traps, radiative and non-radiative relaxation of excited electrons from the conduction band into these traps competes with relaxation to the valence band and reduces the quantum efficiency of the bandedge emission. Injection of electrons from the P3HT reduces the tendancy towards relaxation into these traps. The fluorescence microscopy experiments further demonstrate that relaxation into the trap states

can occur by radiative processes (see Figure 8.6B). Nanorod emission of both short (~ 580 nm) and long (>700 nm) wavelengths is detected in the microscopy experiments.

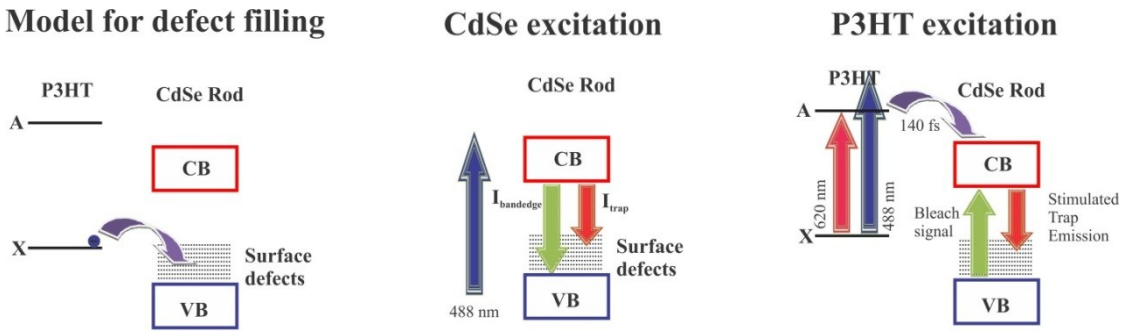

Figure 8.6 Simplified Scheme of the interaction of CdSe nanorods in p3ht/pmma in the fluorescence blinking and the transient absorption experiments

The observation of trap emission suggests that at least some of the trap states are very short lived and that the trapped electrons rapidly relax to repopulated the hole created in the valence band by nanorod excitation. However, other traps are long lived, blocking further excitation and emission processes in the nanorod. These latter traps may involve trapping of the valence band hole, as has been described previously.[140]

The ultrafast transient absorption data provide strong support for the proposed model. These studies confirm the presence of the trap states, their position just above the valence band, their participation in radiative relaxation of excited nanorods, and the role played by charge transfer from P3HT in modulating their population. The ultrafast studies provide direct evidence for charge transfer from P3HT via the observed P3HT ground-state bleach that appears in < 140 fsec. Charge transfer in this case results in population of the conduction band of the nanorods (Figure 8.6C) and the negative absorption signal detected at long wavelengths (> 675 nm) on ps time scales is attributable to stimulated emission between the conduction band of the nanorods and unfilled trap states positioned just above the valence band.

In the fluorescence intermittency experiments, bandedge emission is concluded to be enhanced by charge transfer from P3HT to surface defects on the CdSe nanorods. Charge transfer also takes place via a light activated process, as shown in our previous experiments.[126] The occurrence of charge transfer between P3HT and the CdSe nanorods is further evidenced by the ultrafast experiments, which reveal evidence of stimulated emission in the CdSe nanorods upon excitation of the P3HT alone. The presence of P3HT also impacts the blinking of CdSe

nanorods. Careful analysis of the power law behavior of the bandedge emission channel shows that the nanorods remain in the ON state longer, on average, in the presence of P3HT. Furthermore, analysis of the probabilities of switching between the two ON states and the OFF state reveals that the probability of a transition from bandedge emission to the OFF state is lower in the presence of P3HT. These observations are again attributed to defect filling (both traps in the CdSe and the matrix) by electrons from P3HT. On the whole, these observations and conclusions explain the enhancement of CdSe nanorod bandedge emission observed in both the confocal and widefield image data presented here (see Figure 8.1 and videos presented in supporting information).

On a very fast time scale, the transient absorption experiments have shown that there is a fast (<140 fs) charge transfer from P3HT to CdSe nanorods. This charge transfer is followed by a signal that is assigned to stimulated emission from the conduction band of CdSe nanorod to a defect lying above the valence band. The ultrafast experiments provide strong support for direct charge transfer from P3HT to CdSe. While the ultrafast experiments allow the assignment of charge transfer from P3HT to CdSe nanorods in terms of the ensemble average of the particles, the fluorescence blinking experiments probe the long time (ms to seconds) behavior of individual CdSe nanorods. The stimulated emission confirms that the longer wavelength emission observed in the microscopy experiments involves a transition to the defect sites. In these experiments, we have found that the switching between trapemission/bandedge emission and OFF state in both PMMA and PMMA/P3HT matrix is slow compared to the integration time of the fluorescence blinking experiments (20 ms). When the CdSe nanorods are excited with 488 nm light, the possible relaxation pathways for the excited electron are recombination (radiative and non-radiative) of the electron with the hole present in either in the valance band or on a defect (Fig 6). In addition, electron transfer to the matrix is also possible as it has been pointed out by single molecule blinking experiments on quantum dots.[141] The charge trapping in either case (matrix or surface defects) is likely responsible for the production of OFF states. We observe that there is a slow dynamic switching between the trap and bandedge emission. The fluorescence blinking experiments allow us to assign the time scale of trapping to a few milliseconds. An important difference between the two experiments is the excitation wavelength. The fluorescence microscopy measurements monitor emission under continuous irradiation at 488 nm, which excites both CdSe nanorods and the P3HT polymer, whereas the ultrafast pump pulse at 630 nm

excites only P3HT. The 633 nm excitation of the CdSe nanorods in P3HT in the microscopy experiments does not produce significant trap state emission, but more importantly shows the complete lack of blinking.

8.4 Conclusions

Trap states play an important role in the conversion of photon energy into electricity in solar cells. The combination of ultrafast spectroscopy and emission-state resolved fluorescence microscopy experiments reported here provides a unique opportunity to observe the dynamics of the emitting states on very different timescales. Specifically, the role of the trap state emission of bare CdSe nanorods is investigated in PMMA and PMMA/P3HT blend films. Transient absorption measurements show that for etched CdSe nanorods, photoexcited charges in the P3HT quickly transfer to the CdSe nanorods and a transient signal is observed in the 630-780 range, which is assigned as stimulated emission from the conduction band of CdSe to defect (hole trap) states above the valence band. The fluorescence microscopy measurements monitor emission under continuous irradiation at 488 nm, which excites both CdSe nanorods and the P3HT polymer. In the literature, trap states of CdSe nanocrystals are mostly categorized as non-emissive states, but we find that chemical etching creates emissive trap states that are distinct from the bandedge emission state. The emissive trap states are a direct result of chemical etching by the chlorinated solvent used to fabricate the films.

Chapter 9 - Conclusions

Intrinsic and extrinsic defects of CdSe NPs are studied in this thesis. Few important findings are discussed below.

Extrinsic defects are incorporated by doping CdSe QDs indium and tin dopants. The presence of the dopants is confirmed on per particle bases using high resolution TEM. The dopant significantly changes the electronic structure of the QDs. Temperature dependent PL becomes steeper depending on the relative energy level of the dopant in agreement with the predictions. The PL dynamics indicate the retention of polarization in the aged doped quantum dots. The indium doped samples appear less stable even when covered with the ZnS shell, which leads to a new challenge of exploring ideas to stabilize quantum dots in the presence of strongly reducing dopant electron.

Intrinsic defects of NRs are studied by hybrid inorganic/organic semiconducting films comprised of CdSe NRs dispersed in dilute P3HT/PMMA blends. Optical microscopy and spectroscopy techniques are used to study the defects state. The fluorescence properties of the CdSe NRs are found to be affected by charge transfer from the dilute P3HT/PMMA matrix to the NRs. Interfacial charge transfer between the NRs and P3HT led to luminescence activation of the NRs and enhancement of bandedge emission from the NRs by trap state filling. Trap state filling by electron transfer from P3HT also play a role in altering the “on” and “off” time distributions in NR blinking experiments. Electron transfer from P3HT to the NRs is also reflected by enhanced trap emission observed for NRs dispersed in PMMA, relative to those in dilute P3HT. The results of these studies will be useful to those seeking to prepare CdSe NR/P3HT blends for use in solar energy conversion devices and for further photophysical investigations.

Trap states (defects) play an important role in the conversion of photon energy into electricity in solar cells. The combination of ultrafast spectroscopy and emission-state resolved fluorescence microscopy experiments provides a unique opportunity to observe the dynamics of the emitting states on very different timescales. Specifically, the role of the trap state emission of bare CdSe nanorods is investigated in PMMA and PMMA/P3HT blend films. Transient absorption measurements show that for etched CdSe nanorods, photoexcited charges in the P3HT quickly transfer to the CdSe nanorods and a transient signal is observed in the 630-780 range, which is assigned as stimulated emission from the conduction band of CdSe to defect

(hole trap) states above the valence band. The fluorescence microscopy measurements monitor emission under continuous irradiation at 488 nm, which excites both CdSe nanorods and the P3HT polymer. In the literature, trap states of CdSe nanocrystals are mostly categorized as non-emissive states, but we find that chemical etching creates emissive trap states that are distinct from the bandedge emission state. The emissive trap states are a direct result of chemical etching by the chlorinated solvent used to fabricate the films.

References

(1) Coe-Sullivan, S. S., J. S.; Woo, W.-K.; Bawendi, M. G.; Bulovic, V. *Adv. Funct. Mater.* 2005, *15*, 1117.

(2) Coe-Sullivan, S. W., W.-K.; Steckel, J. S.; Bawendi, M. G.; Bulovic, V. *Org. Electron.* 2003, *4*, 123.

(3) Chan, Y. C., J.-M.; Snee, P. T.; Bawendi, M. G. *Appl. Phys. Lett.* 2004, *85*, 2460.

(4) Medintz, I. L. U., H. T.; Goldman, E. R.; Mattoussi, H. *Nature materials* 2005, *4*, 435.

(5) Seidman, A. H. M., S. L. *Wiley* 1963.

(6) Li, S. S. *Springer* 2006, *2nd edition*.

(7) Nirmal, M. B., L. *Acc. Chem. Res.* 1999, *32*, 407.

(8) Luttinger, J. M. K., W. *Phys. Rev. B* 1955, *97*, 869.

(9) Grunberg, v. H. H. *phys. Rev. B* 1997, *55*, 2293.

(10) Dabbousi, B. O. J. R.-V., J.; Mikulec, F. V.; Heine, J. R.; Mattoussi, H.; Ober, R.; K. F. Jensen, K. F.; Bawendi, M. G. *The journal of physical chemistry. B* 1997, *101*, 9463.

(11) Park, H. W. K., D.-H. *J. Nanomaterials* 2012, 1.

(12) Kim, S. F., B.; Eisler, H-J.; Bawendi, M. G. *J. Am. Chem. Soc.* 2003, *125* 11466.

(13) Tian, Y. N., T.; Kotov, N. A.; Guldi, D. M.; Fendler, J. H. *J. Phys. Chem.* 1996, *100*.

(14) Youn, H. C. B., S.; Fendler, J. H. *J. Phys. Chem.* 1988, *92*, 6320.

(15) Reiss, P. P., M.; Li, L. *small* 2009, *5*, 154.

(16) Murray, C. B. N., D.J.; Bawendi, M. G. *J. Am. Chem. Soc.* 1993, *115*, 8706.

(17) Hines, M. A. B., S.A.; Guyotsionnest, P. *J. Phys. Chem.* 1996, *100*, 468.

(18) Trindade, T. O., P *Adv. Mater.* 1996, *8*, 161.

(19) Burda, C. C., X. B.; Narayanan, R.; El-Sayed, M. A. *Chem. Rev.* 2005, *105*, 1025.

(20) Qu, L. H. P., Z. A.; Peng, X. G *Nano Lett.* 2001, *1*, 333.

(21) Peng, X. G. *Chem. Eur. J.*
2002, *8*, 335.

(22) Cumberland, S. L. H., K. M.; Javier, A.; Khitrov, G. A.; Strouse, G. F.; Woessner, S. M.; Yun, C. S. *Chem. Mater.* 2002, *14*, 1576.

(23) Roy, S. T., C.; Fungura, F.; Dagtepe, P.; Chikan, V. *J. Phys. Chem. C* 2009, *113*, 13008.

(24) Zimmermann, J. A. Z., A.; Röder, B. *Phys. Chem. Chem. Phys.* 2003, *5*, 2964.

(25) van Sark , W. G. J. H. M. F., Patrick L. T. M.; Van den Heuvel , Dave J.; Gerritsen, Hans C. *The journal of physical chemistry. B* 2001 *105*, 8281.

(26) Efros, A. L. R., M.; Kuno, M.; Nirmal, M.; Norris, D. J.; Bawendi, M. G. *Phys. Rev. B* 1996, *54*, 4843.

(27) Nirmal, M. D., B.O.; Bawendi, M. G.; Macklin, J. J.; Trautman, J. K.; Harris, T. D.; Brus, L. E. *Nature* 1996, *383*, 802.

(28) Knappenberger Jr., K. L. W., D. B.; Xu, W.; Schwartzberg, A. M.; Wolcott, A.; Zhang, J. Z.; Leone, S. R. ***ACS Nano*** **2008,** ***2***, **2144.**

(29) Kan, S. M., T.; Rothenberg, E.; Banin, U. ***Nature materials*** **2003,** ***2***, **155.**

(30) Li, L.-S. A., P. A. ***Phys. Rev. Lett.*** **2003,** ***90***, **097402/1.**

(31) Nann, T. S., J. ***Chem. Phys. Lett.*** **2004,** ***384***, **150.**

(32) Manna, L. S., E. C.; Alivisatos, P. A. ***J. Am. Chem. Soc.*** **2000,** ***122***, **12700.**

(33) Peng, Z. A. P., X. ***J. Am. Chem. Soc.*** **2001,** ***123***, **1389.**

(34) Wang, W. B., S.; Jia, S.; Steigerwald, M. L.; Herman, I. P. ***Chem. Mater. 2007*** **2007,** ***19***, **2573.**

(35) Wang, W. G., Y.; Yan, P.; Liu, F.; Xie, Y.; Qian, Y. ***Inorg. Chem. Commun.*** **1999,** ***2***, **83.**

(36) Peng, X. M., L.; Yang, W.; Wickham, J.; Scher, E.; Kadavanich, A.; Alivisatos, P. A. ***Nature*** **2000,** ***404***, **59.**

(37) Hu, J. L., L.-S.; Yang, W.; Manna, L.; Wang, L.-W.; Alivisatos, P. A. ***Science*** **2001,** ***292***, **2060.**

(38) Mokari, T. B., U. ***Chem. Mater.*** **2003,** ***15***, **3955.**

(39) Shockley, W. Q., H. ***J. Appl. Phys.*** **1961,** ***32***, **510.**

(40) Boucle, J. R., P.; Nelson, J. ***J. Mater. Chem.*** **2007,** ***17***, **3141.**

(41) Saunders, B. R.; Turner, M. L. ***Advances in colloid and interface science*** **2008,** ***138***, **1.**

(42) Kymakis, E. K., E.; Franghiadakis, I.; Amaratunga, G. A. J. ***J Phys. D: Appl. Phys.*** **2006,** ***39***, **1058.**

(43) Fang, J. H. L., X. M.; Zhang, X. F.; Fu, D. G.; Lu, Z. H. ***Supramol. Sci.*** **1998,** ***5***, **709.**

(44) Raffaelle, R. P. C., S. L.; Hepp, A. F.; Bailey, S. G. ***Prog. Photovolt.*** **2002,** ***10***, **433.**

(45) Huynh, W. U.; Dittmer, J. J.; Alivisatos, A. P. ***Science*** **2002,** ***295***, **2425.**

(46) Mandal, P. C., V. ***Nano Lett.*** **2007,** ***7***, **2521.**

(47) Trindade, T. ***Chem. Mater.*** **2001,** ***13***, **3843.**

(48) Veinot, J. G. C. G., M.; Pietro, W. J. ***Chem. Mater.*** **1997,** ***9***, **2117.**

(49) Barth, J. V.; Costantini, G.; Kern, K. ***Nature*** **2005,** ***437***, **671.**

(50) Pileni, M. P. ***Langmuir*** **1997,** ***13***, **3266.**

(51) Michalet, X. P., F.; Lacoste, T. D.; Dahan, M.; Bruchez, M. P.; Alivisatos, P. A.; Weiss, S. ***Single Mol.*** **2001,** ***2***, **261.**

(52) Erwin, S. C.; Zu, L.; Haftel, M. I.; Efros, A. L.; Kennedy, T. A.; Norris, D. J. ***Nature*** **2005,** ***436***, **91.**

(53) Yu, D.; Wang, C.; Guyot-Sionnest, P. ***Science*** **2003,** ***300***, **1277.**

(54) Shim, M. G.-S., P. ***Nature*** **2000,** ***407***, **981.**

(55) Turnbull, D. ***J. Appl. Phys.*** **1950,** ***21***, **1022.**

(56) Norris, D. J.; Efros, A. L.; Erwin, S. C. ***Science*** **2008,** ***319***, **1776.**

(57) Du, M. H.; Erwin, S. C.; Efros, A. L. ***Nano Lett.*** **2008,** ***8***, **2878.**

(58) Tuinenga, C.; Jasinski, J.; Iwamoto, T.; Chikan, V. ***ACS Nano*** **2008,** ***2***, **1411.**

(59) Dagtepe, P. C., V.; Jasinski, J.; Leppert, V. J. ***J. Phys. Chem. C*** **2007,** ***111***, **14977.**

(60) Tchebotareva, A. L.; de Dood, M. J. A.; Biteen, J. S.; Atwater, H. A.; Polman, A. ***J. Lumin.*** **2005,** ***114***, **137.**

(61) Anderson, K. E. P., W. E. *J. Non-Cryst. solids* 2002, *299-302*, 1105.

(62) Vasilevskiy, M. I. R., A. G.; Artemyev, M. V.; Filonovich, S. A.; Gomes, M. J. M.; Rakovich, Y. P. *Phys. Stat. Sol.* 2001, *224*, 599.

(63) He, Z.; Jie, J.; Zhang, W.; Luo, L.; Fan, X.; Yuan, G.; Bello, I.; Lee, S. T. *Small* 2009, *5*, 345.

(64) Gonzalez, A. M. P. A., I. V.; Tepantlan, C. S. *Rev. Mex. Fis.* 2009, *55*, 51.

(65) Sahu, A. K., M. S.; Kompch, A.; Notthoff, C.; Wills, A. W.; Deng, D.; Winterer, M.; C. Frisbie, D.; Norris, D. J. *Nano Lett.* 2012, *12*, 2587.

(66) Inamdar, S. N. I., P. P.; Santosh K. Haram, S. K. *ChemPhysChem* 2008, *9*, 2574.

(67) Zhou, Y. R., F. S.; Yuan, Y.; Schleiermacher, H.-F.; Niggemann, M.; Urban, G. A.; Krüger, M *App. Phys. Lett.* 2010, *96*, 013304/1.

(68) Klimov, V. I. *The journal of physical chemistry. B* 2006, *110*, 16827.

(69) Ito, Y. M., K.; Kanemitsu, Y. *J. Lumin.* 2008, *128*, 868.

(70) Wang, H. M.; Bardo, A. M.; Collinson, M. M.; Higgins, D. A. *J. Phys. Chem. B* 1998, *102*, 7231.

(71) Sitt, A. S., A.; Menagen, G.; Banin, U. *Nano Lett.* 2011, *11*, 2054.

(72) Knappenberger, K. L., Jr.; Wong, D. B.; Xu, W.; Schwartzberg, A. M.; Wolcott, A.; Zhang, J. Z.; Leone, S. R. *Acs Nano* 2008, *2*, 2143.

(73) Puzder, A.; Williamson, A. J.; Zaitseva, N.; Galli, G.; Manna, L.; Alivisatos, A. P. *Nano Lett.* 2004, *4*, 2361.

(74) Kumar, S.; Scholes, G. D. *Microchimica Acta* 2008, *160*, 315.

(75) Milliron, D. J.; Gur, I.; Alivisatos, A. P. *MRS Bull.* 2005, *30*, 41.

(76) Wang, F.; Tan, W. B.; Zhang, Y.; Fan, X. P.; Wang, M. Q. *Nanotechnology* 2006, *17*, R1.

(77) Huynh, W. U.; Dittmer, J. J.; Teclemariam, N.; Milliron, D. J.; Alivisatos, A. P.; Barnham, K. W. J. *Phys. Rev. B* 2003, *67*.

(78) Zhou, Y.; Li, Y. C.; Zhong, H. Z.; Hou, J. H.; Ding, Y. Q.; Yang, C. H.; Li, Y. F. *Nanotechnology* 2006, *17*, 4041.

(79) Fiore, A.; Mastria, R.; Lupo, M. G.; Lanzani, G.; Giannini, C.; Carlino, E.; Morello, G.; De Giorgi, M.; Li, Y.; Cingolani, R.; Manna, L. *J. Am. Chem. Soc.* 2009, *131*, 2274.

(80) Gur, I.; Fromer, N. A.; Chen, C. P.; Kanaras, A. G.; Alivisatos, A. P. *Nano Lett.* 2007, *7*, 409.

(81) Murphy, C. J. *J. Mater. Chem.* 2008, *18*, 2173.

(82) Gao, S. Y.; Li, Z. D.; Zhang, H. J. *Current Nanoscience*, *6*, 452.

(83) Makita, Y.; Nakayama, Y.; Fukuzawa, Y.; Wang, S. N.; Otogawa, N.; Suzuki, Y.; Liu, Z. X.; Osamura, M.; Ootsuka, T.; Mise, T.; Tanoue, H. *Thin Solid Films* 2004, *461*, 202.

(84) Dahal, N.; Chikan, V. *Chem. Mat.* 2010, *22*, 2892.

(85) Greenham, N. C.; Peng, X.; Alivisatos, A. P. *Phys. Rev. B* 1996, *54*, 17628.

(86) Skaff, H.; Sill, K.; Emrick, T. *J. Am. Chem. Soc.* 2004, *126*, 11322.

(87) Odoi, M. Y.; Hammer, N. I.; Sill, K.; Emrick, T.; Barnes, M. D. *J. Am. Chem. Soc.* 2006, *128*, 3506.

(88) Hammer, N. I.; Early, K. T.; Sill, K.; Odoi, M. Y.; Emrick, T.; Barnes, M. D. *The journal of physical chemistry. B* 2006, *110*, 14167.

(89) Xu, J.; Wang, J.; Mitchell, M.; Mukherjee, P.; Jeffries-El, M.; Petrich, J. W.; Lin, Z. Q. *J. Am. Chem. Soc.* 2007, *129*, 12828.

(90) Zhang, Q. L.; Russell, T. P.; Emrick, T. *Chem. Mat.* 2007, *19*, 3712.

(91) Chan, W. C. W.; Maxwell, D. J.; Gao, X. H.; Bailey, R. E.; Han, M. Y.; Nie, S. M. *Current Opinion in Biotechnology* 2002, *13*, 40.

(92) Higgins, D. A.; Barbara, P. F. *J. Phys. Chem.* 1995, *99*, 3.

(93) Hoogenboom, J. P.; Hernando, J.; van Dijk, E.; van Hulst, N. F.; Garcia-Parajo, M. F. *Chemphyschem* 2007, *8*, 823.

(94) Lee, S. F.; Osborne, M. A. *ChemPhysChem* 2009, *10*, 2174.

(95) Cogdell, R. J.; Gall, A.; Kohler, J. *Quarterly Rev. Biophys.* 2006, *39*, 227.

(96) Odoi, M. Y.; Hammer, N. I.; Early, K. T.; McCarthy, K. D.; Tangirala, R.; Emrick, T.; Barnes, M. D. *Nano Lett.* 2007, *7*, 2769.

(97) Doi, M. Y.; Early, K. T.; Tangirala, R.; Sudeep, P. K.; Emrick, T.; Barnes, M. D. *J. Phys. Chem. C* 2009, *113*, 13462.

(98) Leatherdale, C. A.; Woo, W. K.; Mikulec, F. V.; Bawendi, M. G. *J. Phys. Chem. B* 2002, *106*, 7619.

(99) Wang, S.; Querner, C.; Emmons, T.; Drndic, M.; Crouch, C. H. *J. Phys. Chem. B* 2006, *110*, 23221.

(100) Wang, S.; Querner, C.; Fischbein, M. D.; Willis, L.; Novikov, D. S.; Crouch, C. H.; Drndic, M. *Nano Lett.* 2008, *8*, 4020.

(101) Efros, A. L.; Rosen, M. *Phys. Rev. Lett.* 1997, *78*, 1110.

(102) Huynh, W. U.; Dittmer, J. J.; Libby, W. C.; Whiting, G. L.; Alivisatos, A. P. *Adv. Func. Mater.* 2003, *13*, 73.

(103) Aldakov, D.; Jiu, T.; Zagorska, M.; Bettignies, R. d.; Jouneau, P.-H.; Pron, A.; Chandezon, F. *Phys. Chem. Chem. Phys.* 2010, *12*, 7497.

(104) Sih, B. C.; Wolf, M. O. *J. Phys. Chem. C* 2007, *111*, 17184.

(105) Cui, C. C.; Kirkeminde, A.; Kannan, B.; Collinson, M. M.; Higgins, D. A. *J. Phys. Chem. C* 2011, *115*, 728.

(106) Landes, C. F.; Braun, M.; El-Sayed, M. A. *J. Phys. Chem. B* 2001, *105*, 10554.

(107) Schreuder, M. A.; McBride, J. R.; Dukes III, A. D.; Sammons, J. A.; Rosenthal, S. J. *J. Phys. Chem. C* 2009, *113*, 8169.

(108) Manna, L.; Scher, E. C.; Li, L.-S.; Alivisatos, A. P. *J. Am. Chem. Soc.* 2002, *124*, 7136.

(109) Yang, J. H.; Tang, A. W.; Zhou, R. J.; Xue, J. G. *Solar Energy Materials and Solar Cells* 2011, *95*, 476.

(110) Dayal, S.; Reese, M. O.; Ferguson, A. J.; Ginley, D. S.; Rumbles, G.; Kopidakis, N. *Advanced Functional Materials* 2010, *20*, 2629.

(111) Goodman, M. D.; Xu, J.; Wang, J.; Lin, Z. Q. *Chem. Mat.* 2009, *21*, 934.

(112) Zhai, G.; Church, C. P.; Breeze, A. J.; Zhang, D.; Alers, G. B.; Carter, S. A. *Nanotechnology* 2012, *23*, 405401.

(113) Nam, M.; Kim, S.; Kang, M.; Kim, S. W.; Lee, K. K. *Org. Electron.* 2012, *13*, 1546.

(114) Saunders, B. R.; Turner, M. L. *Adv. Colloid Interface Sci.* 2008, *138*, 1.

(115) Greenham, N. C.; Peng, X.; Alivisatos, A. P. *Physical Review B* 1996, *54*, 17628.

(116) Ip, A. H.; Thon, S. M.; Hoogland, S.; Voznyy, O.; Zhitomirsky, D.; Debnath, R.; Levina, L.; Rollny, L. R.; Carey, G. H.; Fischer, A.; Kemp, K. W.; Kramer, I. J.; Ning, Z.; Labelle, A. J.; Chou, K. W.; Amassian, A.; Sargent, E. H. ***Nature Nanotechnology*** **2012,** ***7*****, 577.**

(117) Zhao, L.; Lin, Z. Q. ***Adv. Mater.*** **2012,** ***24*****, 4353.**

(118) Hohng, S.; Ha, T. ***Journal of the American Chemical Society*** **2004,** ***126*****, 1324.**

(119) Krauss, T. D.; Brus, L. E. ***Physical Review Letters*** **1999,** ***83*****, 4840.**

(120) Kuno, M.; Fromm, D. P.; Hamann, H. F.; Gallagher, A.; Nesbitt, D. J. ***Journal of Chemical Physics*** **2000,** ***112*****, 3117.**

(121) Mahler, B.; Spinicelli, P.; Buil, S.; Quelin, X.; Hermier, J.-P.; Dubertret, B. ***Nature Materials*** **2008,** ***7*****, 659.**

(122) Shimizu, K. T.; Neuhauser, R. G.; Leatherdale, C. A.; Empedocles, S. A.; Woo, W. K.; Bawendi, M. G. ***Physical Review B*** **2001,** ***63*****, 205316.**

(123) Wang, S.; Querner, C.; Emmons, T.; Drndic, M.; Crouch, C. H. ***Journal of Physical Chemistry B*** **2006,** ***110*****, 23221.**

(124) Mokari, T.; Banin, U. ***Chem. Mat.*** **2003,** ***15*****, 3955.**

(125) Jander, S.; Kornowski, A.; Weller, H. ***Nano Letters*** **2011,** ***11*****, 5179.**

(126) Roy, S.; Aguirre, A.; Higgins, D. A.; Chikan, V. ***J. Phys. Chem. C*** **2012,** ***116*****, 3153.**

(127) Knowles, K. E.; McArthur, E. A.; Weiss, E. A. ***Abstracts of Papers of the American Chemical Society*** **2011,** ***242*****.**

(128) Kalyuzhny, G.; Murray, R. W. ***Journal of Physical Chemistry B*** **2005,** ***109*****, 7012.**

(129) Gomez-Campos, F. M.; Califano, M. ***Nano Letters*** **2012,** ***12*****, 4508.**

(130) Puzder, A.; Williamson, A. J.; Zaitseva, N.; Galli, G.; Manna, L.; Alivisatos, A. P. ***Nano Letters*** **2004,** ***4*****, 2361.**

(131) Wang, H. M.; Bardo, A. M.; Collinson, M. M.; Higgins, D. A. ***Journal of Physical Chemistry B*** **1998,** ***102*****, 7231.**

(132) Giblin, J.; Syed, M.; Banning, M. T.; Kuno, M.; Hartland, G. ***Acs Nano*** **2010,** ***4*****, 358.**

(133) Sirringhaus, H.; Brown, P. J.; Friend, R. H.; Nielsen, M. M.; Bechgaard, K.; Langeveld-Voss, B. M. W.; Spiering, A. J. H.; Janssen, R. A. J.; Meijer, E. W.; Herwig, P.; de Leeuw, D. M. ***Nature*** **1999,** ***401*****, 685.**

(134) Brown, P. J.; Thomas, D. S.; Kohler, A.; Wilson, J. S.; Kim, J. S.; Ramsdale, C. M.; Sirringhaus, H.; Friend, R. H. ***Physical Review B*** **2003,** ***67*****.**

(135) Guo, J. M.; Ohkita, H.; Benten, H.; Ito, S. ***Journal of the American Chemical Society*** **2009,** ***131*****, 16869.**

(136) Carey, C. R.; Yu, Y.; Kuno, M.; Hartland, G. V. ***J. Phys. Chem. C*** **2009,** ***113*****, 19077.**

(137) Knowles, K. E.; McArthur, E. A.; Weiss, E. A. ***Acs Nano*** **2011,** ***5*****, 2026.**

(138) Lim, S. J.; Kim, W.; Jung, S.; Seo, J.; Shin, S. K. ***Chem. Mat.*** **2011,** ***23*****, 5029.**

(139) Hu, J. T.; Li, L. S.; Yang, W. D.; Manna, L.; Wang, L. W.; Alivisatos, A. P. ***Science*** **2001,** ***292*****, 2060.**

(140) Vietmeyer, F.; Tchelidze, T.; Tsou, V.; Janko, B.; Kuno, M. ***Acs Nano*** **2012,** ***6*****, 9133.**

(141) Schwartz, O.; Oron, D. ***Isr. J. Chem.*** **2012,** ***52*****, 992.**

Appendix A

A.1 temperature dependence of semiconductor

```
function [ output_args ] = arheniouseq( input_args )
%UNTITLED2 Summary of this function goes here

%   Temperature dependence of semiconductor

k=8.617E-5;
t=1:1:300;
x=1./t;
x=x'
y=-(1/k)*x;
plot(x,y)
end
```

A.1 Surface to volume ratio calculations for perfect sphere and rods

```
function [ output_args ] = stvratio( input_args )
%UNTITLED2 Summary of this function goes here
%   Detailed explanation goes here
%surface to volume ratio of Quantum Dots
x=0.1:0.01:10;
x=x';
a=4*3.14*(x.^2);
v=(4/3)*3.14*(x.^3);
y=a./v;
 %surface to volume ratio of nanorods
r1=0.1:0.01:3;
r1=r1';
h1=6;
a1=(2*3.14*(r1.^2))+(2*3.14*r1.*h1);
v1=3.14*r1.^2*h1;
y1=a1./v1;
r2=2;
```

```
h2=3:0.1:20;
h2=h2'
a2=(2*3.14*(r2^2))+(2*3.14*h2.*r2);
v2=h2.*3.14*r2^2;
y2=a2./v2
plot(r1, y1)
figure
plot(h2, y2)

end
```

A.2 Analysis of polarized light emission

```
function [ output_args ] = readbin4( input_args )
%UNTITLED1 Summary of this function goes here
%  reading polarised emission
%calculation of polarized light emission from NRs
R=5;
im1=[];
im2=[];
x=[];
y=[];
fid = fopen('1.cfl');
fseek(fid, 84, 'bof');
 for i=1:12,
    im = fread(fid,[100,100],'uint16','l');
    im=im';
    im1=[im1, im];
    fseek(fid, 8, 'cof');
end
fclose(fid);
im1=reshape(im1,100,100,12);
imper=zeros(100,100,6);
for i=1:6
    imper(:,:,i)=im1(:,:,i*2-1);
end
imper=reshape(imper,100,100,6);
impar=zeros(100,100,6);
for i=1:6
    impar(:,:,i)=im1(:,:,i*2);
end
impar=reshape(impar,100,100,6);
dic=(impar-imper)./(impar+imper);
tot=impar+2*imper;

for i=1:100
```

```
    for j=1:100
    vect=tot(i,j,:);
    vect=reshape(vect,1,6);
    Y=fft(vect);
    real_fft_tot(i,j,:)=abs(Y);
    imag_fft_tot(i,j,:)=unwrap(angle(Y));
    end
end

for i=1:100
    for j=1:100
    vect=dic(i,j,:);
    vect=reshape(vect,1,6);
    Y=fft(vect);
    real_fft_dic(i,j,:)=abs(Y);
    imag_fft_dic(i,j,:)=unwrap(angle(Y));
    end
end
i=2;
subplot(2,2,1);
imagesc(real_fft_tot(:,:,i));
title('Real, FFT of tot');
colormap(hot);
colorbar;
subplot(2,2,2);
imagesc(imag_fft_tot(:,:,i));
title('Imaginary, FFT of tot');
colorbar;
subplot(2,2,3);
imagesc(real_fft_dic(:,:,i));
title('Real, FFT of dichroism');
colorbar;
subplot(2,2,4);
imagesc(imag_fft_dic(:,:,i));
title('Imaginary, FFT of dichroism');
colorbar;
end
```

A.3 Reading confocal image data

```
function [ im1 im2 dic ] = readbin( input_args )
%UNTITLED1 Summary of this function goes here
%  Detailed explanation goes here
fid = fopen('9.cfl');
fseek(fid, 100, 'bof');
im = fread(fid,[200,400],'uint16','b');
```

```
fclose(fid);
%normalizing image to 0 to 1 optional
%Nor = im - min( im(:) );
%imnorm = Nor / max( Nor(:) );

im1=im(:,1:200);
im2=im(:,201:end);

subplot(2,2,1);
imagesc(im1+im2);
Title('Tot image','FontSize', 14);
   xlabel('x axis / pixel','FontSize', 14);
   ylabel('y axis / pixel','FontSize', 14);
   set(gcf, 'color', 'white');
   colorbar;
   colormap jet;
subplot(2,2,2);
diff=im1-im2;
tot=im1+2*im2;
dic=diff./tot;
imagesc(dic);
Title('Dichroism','FontSize', 14);
   xlabel('x axis / pixel','FontSize', 14);
   ylabel('y axis / pixel','FontSize', 14);
   set(gcf, 'color', 'white');
   colorbar;
   colormap jet;

   par=sum(sum(im1));
   per=sum(sum(im2));
   ani=(par-per)/(par+2*per);

   %getting the histogram
subplot(2,2,3);
   tot=im1+im2;
   n = numel(tot)
   totv=tot(:);
   [y x]=hist(totv,50);
   semilogy(x,y);
   Title('Image Hist','FontSize', 14);
   xlabel('intensity counts/s','FontSize', 14);
   ylabel('# of events','FontSize', 14);

   subplot(2,2,4);
   pol=(im1-im2)./(im1+im2);
   n = numel(pol)
```

```
 polv=pol(:);
 [y x]=hist(polv,50);
 semilogy(x,y);
Title('Dichroism Hist','FontSize', 14);
xlabel('Dichroism','FontSize', 14);
 ylabel('f*P','FontSize', 14);
```

A.4 Reading time trace from confocal data

```
function [time ani par per Autocorr1 lag1 Autocorr2 lag2 Autocorr3 lag3] = readtrace( file )
%UNTITLED1 Summary of this function goes here
%  Detailed explanation goes here
fid = fopen(file);
fseek(fid, 0, 'bof')
tr = fread(fid,'uint32','b');
fclose(fid);
l=length(tr)/2;
par=tr(1:l);
per=tr(l+1:end);
par=par(1:end-100);
per=per(1:end-100);
timestep=tr(1);
stp=1/timestep;
lengthoftrace=length(par)-1;
par(1)=[];
per(1)=[];
par=par*1;
maximum=lengthoftrace*stp;
time=0:stp:maximum;
time(1)=[];
time=time';
subplot(3,1,1);
plot(time,par,time,per);
legend('par','per',2);
xlabel('time / s');
ylabel('count /s ');
title('Paralel and perpedicular detector');
dic=par./per;
subplot(3,1,2);
plot(time,dic);
xlabel('time / s');
ylabel('dichroism');
title('dichroism');
subplot(3,1,3);
ani=(par-per)./(par+2*per);
plot(time,ani);
```

```
xlabel('time / s');
ylabel('anisotropy');
title('anisotropy');
figure();
[Autocorr1 lag1] = xcorr(ani);
lag1=lag1/50;
lag1=lag1';

maximum=length(Autocorr1);
center=length(Autocorr1)/2;
Autocorr1=Autocorr1(center:maximum);
lag1=lag1(center:maximum);
for i=1:length(Autocorr1)
Autocorr1(i)=Autocorr1(i)/(length(Autocorr1)-i+1);
end
Autocorr1(1)=[];
lag1(1)=[];
Autocorr1=Autocorr1/Autocorr1(1);

[Autocorr2 lag2] = xcorr(par);
lag2=lag2/50;
lag2=lag2';

maximum=length(Autocorr2);
center=length(Autocorr2)/2;
Autocorr2=Autocorr2(center:maximum);
lag2=lag2(center:maximum);
for i=1:length(Autocorr2)
Autocorr2(i)=Autocorr2(i)/(length(Autocorr2)-i+1);
end
Autocorr2(1)=[];
lag2(1)=[];
Autocorr2=Autocorr2/Autocorr2(1);

[Autocorr3 lag3] = xcorr(per);
lag3=lag3/50;
lag3=lag3';

maximum=length(Autocorr3);
center=length(Autocorr3)/2;
Autocorr3=Autocorr3(center:maximum);
lag3=lag3(center:maximum);
for i=1:length(Autocorr3)
Autocorr3(i)=Autocorr3(i)/(length(Autocorr3)-i+1);
end
Autocorr3(1)=[];
```

```
lag3(1)=[];
Autocorr3=Autocorr3/Autocorr3(1);

plot(lag1,Autocorr1,lag2,Autocorr2,lag3,Autocorr3);
legend('anisotropy','par','per',3);
end
```

A.5 Calculation of sum image from wide field data (reversibility experiment)

```
function [ output_args ] = trackbin2( input_args )
%UNTITLED1 Summary of this function goes here
%  track rods and plot avg intensity Vs laser power
R=5;
%for i=1:8
   %str1 = num2str(i);
   %str2='.dat';
   %filename=[str1 str2];

fid = fopen('14.dat');
%fseek(fid, 0, 'bof');
im1 = fread(fid,[256,25600],'uint32','l');
fclose(fid);
im2=reshape(im1,[256,256,100]);
h1=figure();
set(h1,'Position',[20,400, 600, 600] );
title('movie image');

%ploting original image
im3=zeros(256,256);
for i=1:100
var1=im2(:,:,i);
im3=im3+var1;
imagesc(im2(:,:,i));
drawnow();
end

meanim=im3./100;
imagesc(meanim);
title('Original image');

%[x y]=ginput(1);
%x=round(x);
%y=round(y);
hold on;
DrawCircle(85 ,142, R, 32, 'b-');
```

```
%Circle with radius centered at 40,40 in an 256x256image
[rr cc] = meshgrid(1:256);
C = sqrt((rr-85).^2+(cc-142).^2)<=5;
imshow(C);

cutim=(meanim.*C);
imagesc(cutim);
data=sort(nonzeros(reshape(cutim,1,[])));
vector=1:10;
background=mean(data(vector));
data=data-background;
signal=sum(data)

end
%end
```

A.6 Reading binary file of confocal image

This code is used to generate Figure 5.1.

```
function [ output_args ] = readbin( input_args )
%UNTITLED1 Summary of this function goes here
%  Detailed explanation goes here
fid = fopen('12.cfl');
fseek(fid, 100, 'bof');
im = fread(fid,[200,200],'uint16','b');
fclose(fid);

im1=im(:,1:200);

imagesc(im1);
Title('QDs image','FontSize', 14);
   xlabel('x axis / pixel','FontSize', 14);
   ylabel('y axis / pixel','FontSize', 14);
   set(gcf, 'color', 'white');
   colorbar;
   colormap hot;
```